OSAKA University - Graduate School of Science

Department of Physics

Doctor of Philosophy Dissertation

Study of Electronic Raman Scattering and Angle-resolved Photoemission Spectra of $Bi_2Sr_2CaCu_2O_{8+\delta}$ Superconductors

by

Nguyen Trung Hieu

Supervisor: Prof. Setsuko TAJIMA

OSAKA, April - 2014

To all people I love!

Contents

Chapter 1

Introduction

Nearly 30 years have passed since the discovery of high-T_c superconductivity in the cuprates, however its mechanism is still in mystery. Cuprates have a layered structure with common CuO_2 planes on which superconductivity appears from formation of Cooper pairs. The pairing symmetry in cuprates is d-wave which is different from the BCS s-wave of conventional superconductors. The parent compound of high-T_c cuprates are antiferromagnetic Mott-insulators which are half-filled in the most upper electronic band $d_{x^2-y^2}$ but insulating because of a strong Coulomb interaction between on-site electrons. It is unclear how a Mott-insulator changes into a superconductor until now. Therefore understanding the electronic structure in both the normal and the superconducting state is important. The pseudogap state in the normal state just above superconducting transition temperature (T_c) is a strange state observed by many techniques. There are three different viewpoints on the pseudogap. The pseudogap competes with superconductivity, the pseudogap is the precursor of superconductivity and the pseudogap is independent of superconductivity. Study on manifestations of pseudogap and on its effects to superconductivity has been done intensively.

Both angle-resolved photoemission spectroscopy (ARPES) and electronic Raman scattering (ERS) are strong tools to study the electronic structure of cuprate superconductors. ARPES is a single particle method while Raman is a two-particle method. In Raman measurements, with different geometries one can probe different regions on Brillouin zone (BZ). However, the origin of electronic Raman spectra is still unclear, and if we compare quantitatively the results obtained by ARPES

and Raman, one could see that there are some differences.

In this study, *electronic Raman spectra in B_{1g} and B_{2g} geometries are calculated from ARPES data in the superconducting state for cuprate superconductor $Bi_2Sr_2CaCu_2O_{8+\delta}$ (Bi2212).* This study was done for Bi2212 single crystals with different doping levels, underdoped $T_c = 75$ K (UD75K), nearly optimally doped $T_c = 92$ K (OP92K) and overdoped $T_c = 85$ K (OD85K).

Calculated electronic Raman spectra in B_{1g} and B_{2g} geometries were obtained and they are more realistic than the ones from a well-known theory, the kinetic theory. Two-energy-scale behavior was reproduced. There is a consistency between the calculation and the experimental data in B_{2g} spectra whereas in B_{1g} spectra the difference is clearer in the underdoped region. We discuss the effect of the pseudogap to the superconducting gap and the manifestation of this effect in different measurement techniques. We also found that there is a doping dependence of the peak-intensity profile of spectral functions in k space. We confirm that the same gap profile could be used to interpret both Raman and ARPES data, in which the nodal slope of the gap profiles is independent for a wide range of doping levels.

The structure of this thesis is designed as follows. *Chapter 2* overviews high-T_c superconductivity with some different behaviors from BCS superconductors. The crystal structure of Bi2212 as well as the electronic structure of parent compounds are described. Purposes of this study are presented at the end of this chapter. In *chapter 3*, the principles of ARPES and Raman measurements are presented. Chapter 4 presents all experimental results on crystal growth, ARPES and Raman measurements. Results of calculations for electronic Raman spectra using ARPES data are presented in *chapter 5*. Calculations were done using the well-known so-called kinetic theory and using Kubo formula. Calculations are presented in a way that calculated spectra step by step are improved. The final results were obtained by a calculation using Kubo-formula, taking ARPES data over the whole-BZ, with Shirley-background-subtraction and **k**-dependence of peak-intensity profile of spectral functions. In *chapter 6*, the momentum and doping dependences of the spectral function are discussed. We also discuss the effect of pseudogap to the superconducting gap in Raman and ARPES data. *Chapter 7* summarizes the obtained results and possible issues in next studies.

Chapter 2

Background on high-temperature superconductivity, cuprates and $Bi_2Sr_2CaCu_2O_{8+\delta}$

2.1 High-temperature superconductivity

Superconductivity was discovered by H. K. Onnes in 1911 in mercury when he used liquid He to cool down Hg below 4.2 K. This phenomenon was a mystery until J. Bardeen, L. N. Cooper and J. R. Schrieffer built their microscopic theory in 1957, BCS theory [1]. Superconductivity is a quantum phenomenon that manifests in a macroscopic scale, where every electron pairs move with a coherence. In 1986, J. G. Bednorz and K. A. Müller published their results on superconductivity in $(La, Ba)_2CuO_4$ with a critical temperature (T_c) around 30 K [2]. This opens a new era of study on superconductivity because in conventional (BCS) superconductors the critical temperature is believed lower than 30 K [3] and the T_c record at that time was 23 K in Nb_3Ge system. According to the BCS theory, in order to increase T_c, the interaction constant needs to be improved. Before the discovery of J. G. Bednorz and K. A. Müller much effort was done to increase T_c, for example, by increasing electron density at the Fermi energy. However, increase of electron density leads to instability of crystal structure. J. G. Bednorz and K. A. Müller chose oxides to increase the electron-ion interaction and hence the interaction potential. The enhancement of interaction is expected because in oxides the electron concen-

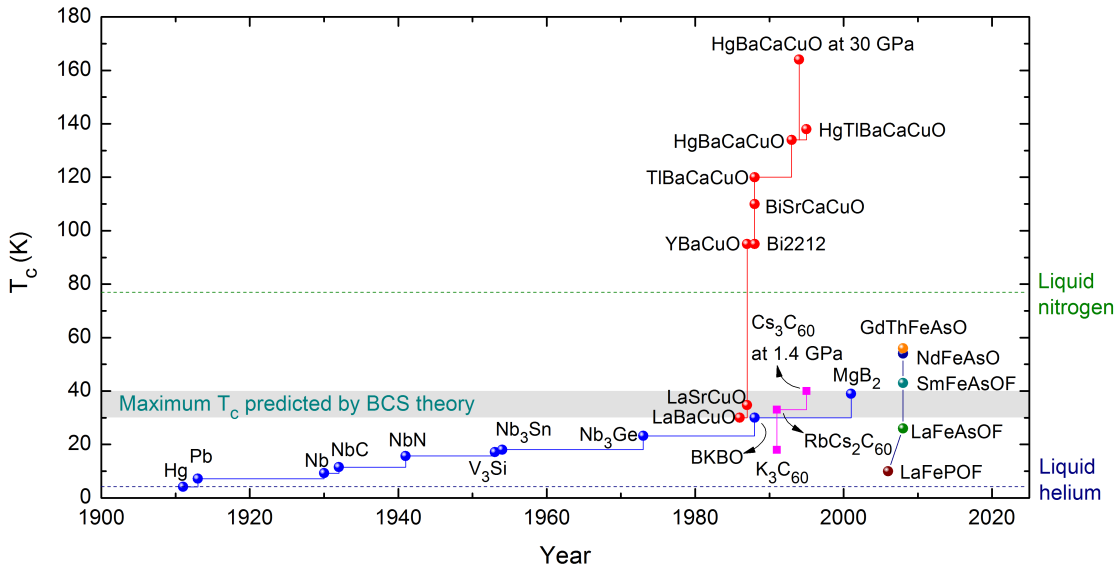

Figure 2.1: Remark discoveries by time.

tration is not so high as in metals and thus the screening effect is small [4]. Only a half year later, the superconductor with much higher T_c above the liquefying temperature of nitrogen were discovered, the first of them is $YBa_2Cu_3O_7$ (YBCO) superconductor [5]. Figure 2.1 presents the history of discoveries of superconductors. The group of superconductors which has record T_c above 77 K until now is layered-perovskite-structure copper oxides called cuprates.

The highest T_c until now is hold in the (Hg,Tl)BaCaCuO system with T_c = 133-138 K at ambient pressure [6, 7] and it can reach up to 155-164 K at 30 GPa [8, 9]. One common feature in all cuprates which should be emphasized is that they have the same CuO_2 layers on which superconductivity appears. The Hg-system is believed to have the highest T_c^{max}, even in the superconductor with one layer of CuO_2 T_c^{max} is also as high as 97 K, because its CuO_2 layers have the most ideal structure without any bending as in the other cuprates.

Recently, iron-based superconductors were discovered [12, 13] and the highest T_c in this systems up to now is about 55 K in the 1111 system [14–17]. Iron-based superconductors also have layered structures as in the cuprates and show many new properties which are under debate. Also recently another hole-doped cuprate with high T_c upto 120 K was also discovered in BaCaCuO(F,O) system [18].

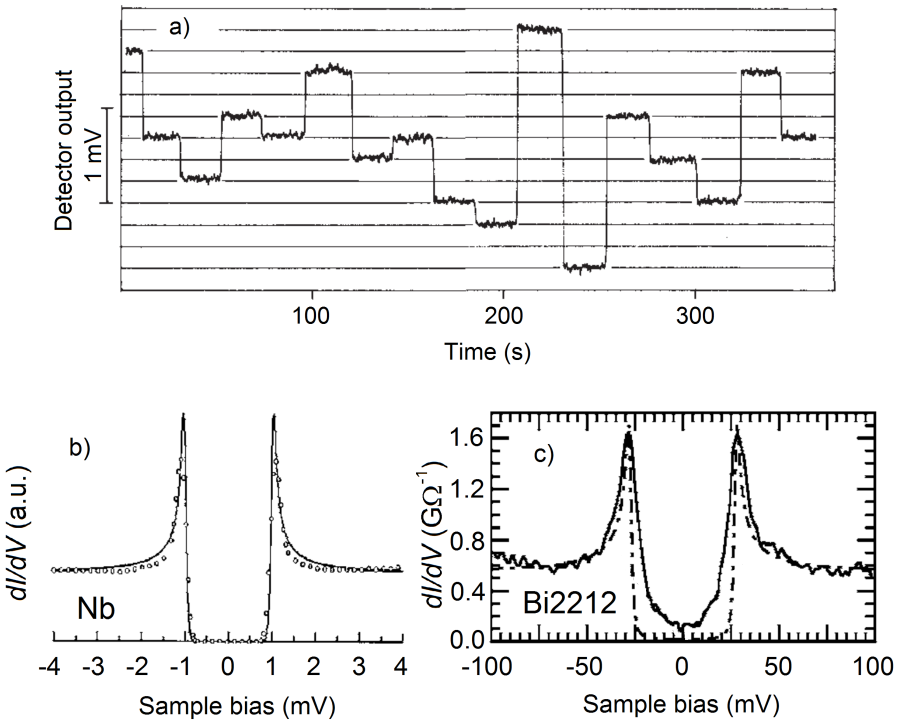

Figure 2.2: a) Change in output signal of r.f. SQUID magnetometer with integral numbers of flux quanta [10]. b) STM c-axis tunneling conductance spectra of superconductors in comparison with BCS theory. Conventional superconductor Nb at 335 mK (circles) and BCS fit (solid line) with $\Delta = 1.0$ meV; and an optimally doped Bi2212 ($T_c = 92$ K) at 4.8 K and s-wave BCS fit (dash-dotted line) with $\Delta = 27.5$ meV [11].

Just after the discovery of high-T_c superconductors, flux quantum [10] and Shapiro-step [19,20] measurements confirmed the formation of Cooper pairs in the superconducting state. An energy gap in the superconducting state as well as its behaviors different from BCS superconductors, figure 2.2, were confirmed by many measurement techniques.

Parent compounds of cuprate superconductors are antiferromagnetic charge transfer insulators. By doping carrier the antiferromagnetic order is suppressed and at certain doping around 0.05 superconductivity appears when temperature is below T_c. This is presented in the figure 2.3 of a general phase diagram. Critical temperature T_c as a function of doping shows a dome shape and usually T_c dome is divided into three regions, underdoped, optimally doped and overdoped region. In high-T_c cuprate superconductors, there is a strange region in the normal state and it is believed that understanding about this region can answer for the mecha-

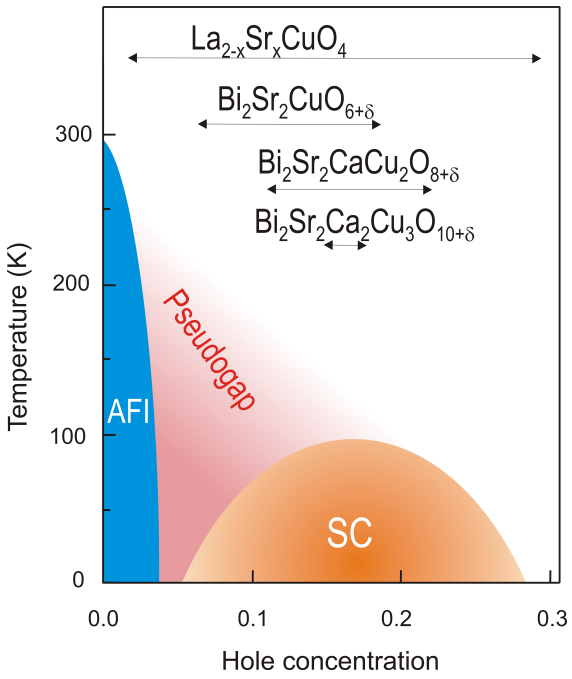

Figure 2.3: General phase diagram of hole-doped high-T_c cuprates. The superconducting dome includes a underdoped region, an optimally doped region with maximum T_c and an overdoped region.

nism of high-T_c superconductivity. In this region there is suppression in low energy region of excitation spectra measured by various techniques at temperatures below T*, which manifests an opening of a gap. In the BCS theory, when a superconductor is cooled down through the superconductivity transition temperature T_c, Cooper pairs are formed and an energy gap opens at the Fermi level. Therefore the gap opening in the normal state similar as the superconducting gap is so-called pseudogap and we have a pseudogap region in the phase diagram. A well-known empirical formula for T_c dome of cuprates is usually used to deduce dopings p [21]

$$T_c = T_c^{max}[1 - 82.6(p - 0.16)^2]. \tag{2.1}$$

Isotope effect is decisive and direct evidence to confirm the role of phonon in conventional superconductors. Its major role is to reveal the origin of attractive interaction in BCS theory where T_c scales with the isotope mass $T_c \sim M^{-\alpha}$. Therefore this effect has been studied a lot in high-T_c cuprate superconductors as well as other unconventional superconductors. In BCS superconductivity the isotope coefficient is 0.5. However in high-temperature superconductors, isotope

effect shows more complex behaviors than BCS theory, figure 2.4. Although there are some isotope studies supporting for phonon mediated mechanism [24], a general view is that it is not strong at optimally doping level where the highest T_c is observed, isotope coefficient is smaller than 0.1 at doping $p = 0.16$ as discovered in LSCO, YBCO and Bi2212 [25–27]. In $La_{2-x}Sr_xCuO_4$ (LSCO) system, isotope exponent gets maximum at the doping level of 1/8 where T_c is suppressed. Studies on optimally doped samples in bismuth system show that oxygen isotope effect exponent decreases with increasing number of CuO_2 layer [23]. These phenomena seems opposite to a phonon-mediated mechanism with electron-phonon interaction to be major role or there is certain contribution from phonons but compete with another unknown quantity.

Raman scattering is used as a strong tool to study isotope effect from shifts of phonon peaks [28–31] as one example shown in figure 2.5. By using Raman scattering we can evaluate the exchange of oxygen isotopes from appearance of phonon peaks and relativity intensities between them. Isotope effect from Raman spectra can be determined as $\frac{\omega(^{16}O) - \omega(^{18}O)}{\omega(^{16}O)}$. Raman scattering measurement also helps to assign phonon peaks to different vibration modes of different atoms at different sites in a crystal structure. Figure 2.5 presents Raman data with the site-selective isotope exchange in YBCO.

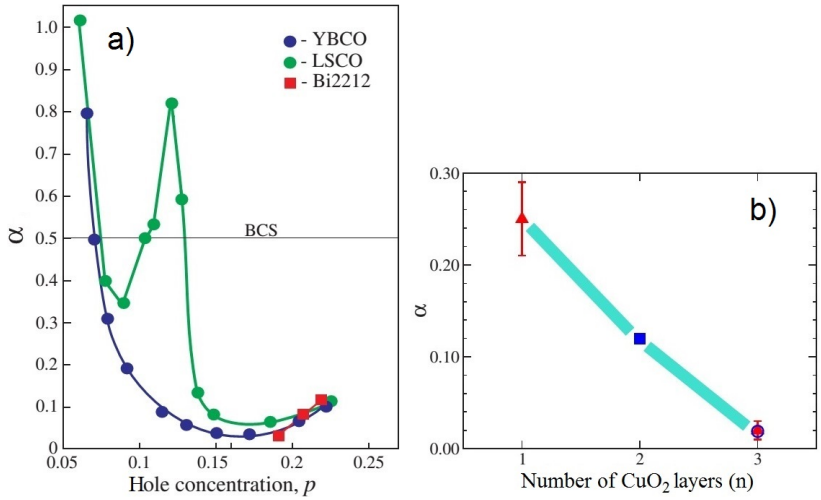

Figure 2.4: Oxygen isotope effect in high-T_c cuprates. a) Isotope effect exponent α as a function of hole concentration [22]. b) Isotope effect exponent α against number of CuO_2 layers in the optimally doped Bi-based cuprates, the square data point denotes data of Bi2212 with $T_c = 92$ K [23].

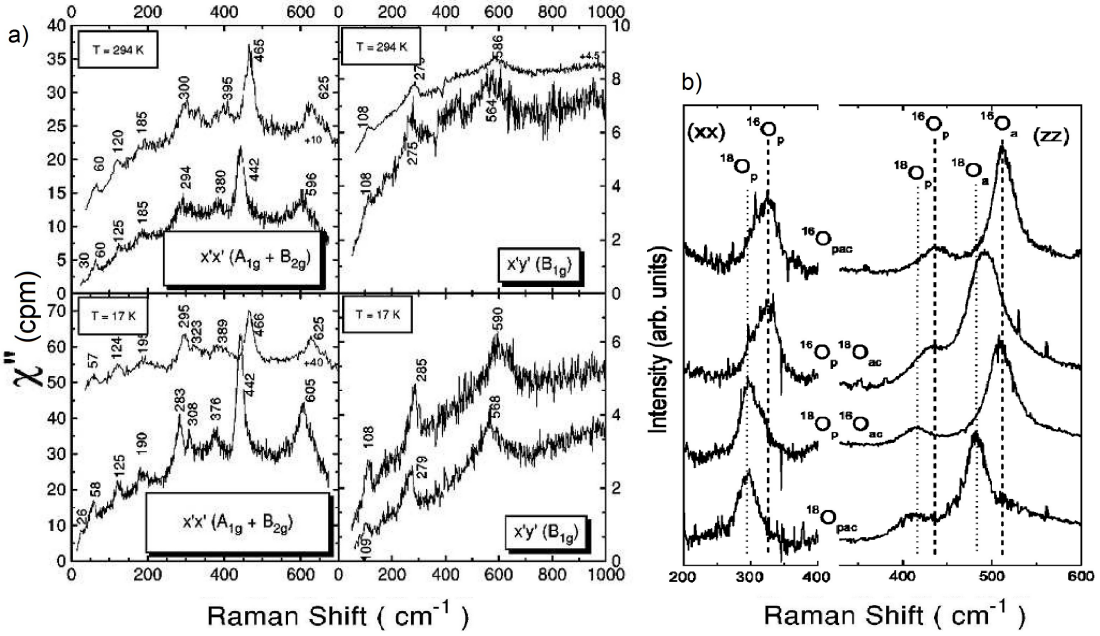

Figure 2.5: Oxygen isotope effect obtained by Raman measurements. a) Shift of phonon peaks from Raman spectra of ^{18}O exchanged (lower curve in each panel) and unexchanged ^{16}O (upper curve in each panel) Bi2212 ($T_c = 51$ K) taken at 294 K and 17 K in the $A_{1g} + B_{2g}$ and B_{1g} geometry [28]. b) Site-selective exchange in oxygen isotope effect determined from Raman spectra of YBCO. Notations p, a and c in this figure denote planar, apical and chain oxygens, respectively [29].

In BCS superconductors such as aluminum, the coherent length ξ is as very large as 16000 Å while its penetration depth λ is 16 Å [32], and therefore structural anisotropy is averaged. It is not the case of high-T_c cuprates where the penetration depth is larger than the coherent length, for example in optimally doped Bi2212 sample and at low temperature $\xi_{ab} = 13$ Å while $\lambda_{ab} = 1850$ Å [33] or in c axis direction $\xi_c = 1$ Å while $\lambda_c = 100$ μm [34]. Therefore, in the cuprates the Landau parameter $\kappa = \lambda/\xi$ is much larger than 1 and the cuprates are type-II superconductors with very high critical fields H_{c2}.

The penetration depth can be determined from relaxation rate σ in μ-spin rotation measurements because of $\sigma \sim \frac{1}{\lambda^2}$. A linear relationship between the critical temperature and the μ-spin relaxation rate for many unconventional superconductors including all high-T_c cuprate superconductors in the underdoped region was discovered by Y. J. Uemura as well known "Uemura plot" [35,36]. The linear relationship is not only in cuprates but also in other superconductors as heavy fermion,

A_3C_{60}, 3D BKBO superconductors. Therefore this behavior may show a general mechanism for these superconductors. However a magnetism-mediated mechanism is believed to be true for heavy fermion superconductors [37] while in the BKBO system with a relatively high-T_c ($\approx$ 30 K), a high isotope coefficient $\alpha = 0.41$ [38] was observed and it is interpreted as a phonon superconductor.

It was also shown that there is a linear correlation between the transition temperature and the plasma frequency [39] and the penetration depth also can be determined from optical/infrared measurements $\lambda_L^{FTIR} = 1/2\pi\omega_p$ [40]. However, for Bi2212 the values of in-plane penetration depth obtained from μ-SR and FTIR measurements are quite different, 190 nm and 680 nm, respectively.

Pairing symmetry could show information about the mechanism of superconductivity. There are several types of pairing symmetry proposed for high-T_c cuprates such as d-wave, anisotropic s-wave, extended s-wave, $s \pm id$-wave. In a conventional BCS superconductor, the pairing symmetry is isotropic s-wave where the phonon-mediated mechanism is proved. Even though, in high-T_c cuprates now it is well accepted that the pairing symmetry is d-wave. This is confirmed by many probe techniques including ERS and ARPES [41–45]. However there are also some discussions arguing that the d-wave pairing is not enough to explain behaviors of some materials where maybe a $d + s$-wave pairing exists for overdoped region [46–50]. In present study, the d-wave pairing symmetry is used and the gap size along Fermi surface is a linear function of d-wave function, $\Delta(\mathbf{k}) = \Delta_0|cos(k_x a) - cos(k_y a)|/2$ where Δ_0 is the maximum gap. The gap function has its has a minimum value (zero) along the nodal line ((0,0)-(π,π)), ARPES data showed that there is no gap in this direction even at temperatures well below T_c, and a maximum at the antinodal region ($\pm\pi$,0) or (0,$\pm\pi$), figure 2.6 a). Because of nodes in the gap function, spectra of electronic excitation in low energy region below 2Δ at low temperature is not zero as in the case of s-wave pairing. The d-wave pairing symmetry was first proposed to explain superconductivity in heavy fermion superconductors where spin fluctuation is a mechanism of superconductivity. However, even the d-wave symmetry exists in high-T_c cuprates, a underlying mechanism from magnetism is still under debate.

The deviation from the pure d-wave gap symmetry in underdopped samples shows a two-gap-like (or two-component) behavior [51–53] that manifests in the antinodal region of the gap function along Fermi surface. Figure 2.6 b) shows

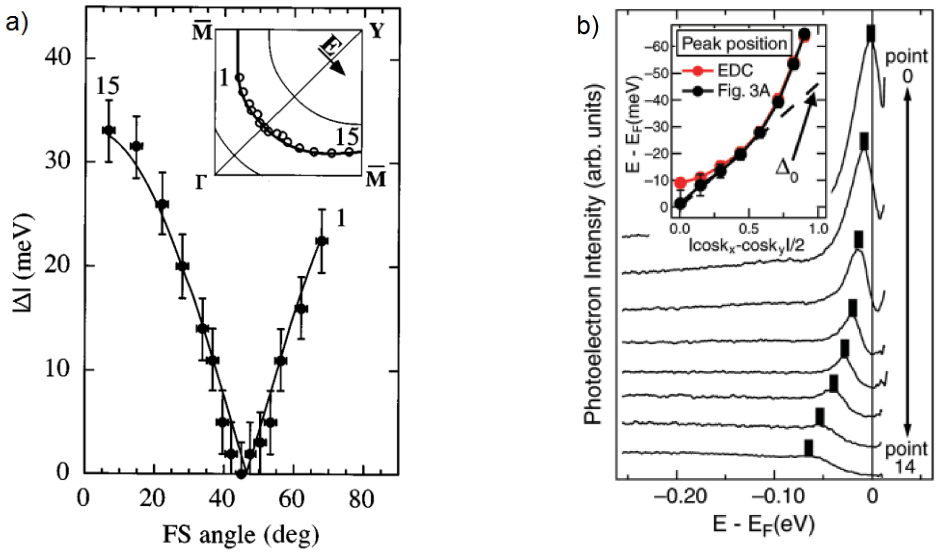

Figure 2.6: a) The *d*-wave symmetry of pairing observed by ARPES in Bi2212 single crystal with $T_c = 87$ K. [42]. The dots with error bars are experimental data taken on *k*-points on the Fermi surface shown in the inset (the circles). The solid line is fitting by *d*-wave function. b) The deviation from the *d*-wave paring observed by ARPES in a underdoped Bi2212 sample $T_c = 50$ K. Here are EDC spectra along the Fermi surface from the nodal region (point 0) to the antinodal region (point 14) after dividing for Fermi-Dirac function. Their peak position against *d*-wave function is plotted in the inset (the black-dotted curve) [51].

ARPES energy distribution curve (EDC) spectra along the Fermi surface of a underdoped Bi2212 sample $T_c = 50$ K, *k*-points are numbered from 0 (node) to 14 (antinode). The gap size defined by peak position suddenly changes at the point 8 as shown in the inset, the straight dash line is the gap function obtained from the *d*-wave symmetry with the same slope in the nodal region. The pairing symmetry with really two components from different mechanisms is still not clear yet.

2.2 $Bi_2Sr_2CaCu_2O_8$

Bi-Sr-Ca-Cu-O superconductors are the first high-T_c ones that do not contain rare-earth elements, discovered by H. Maeda in 1988 [54], which were developed after the discovery of YBCO system. Bi-based superconductors have a general formula $Bi_2Sr_2Ca_{n-1}Cu_nO_y$ in which n = 1, 2 and 3. When the number of CuO_2 plane increases from 1 to 3, the maximum T_c increases. In the other cuprate supercon-

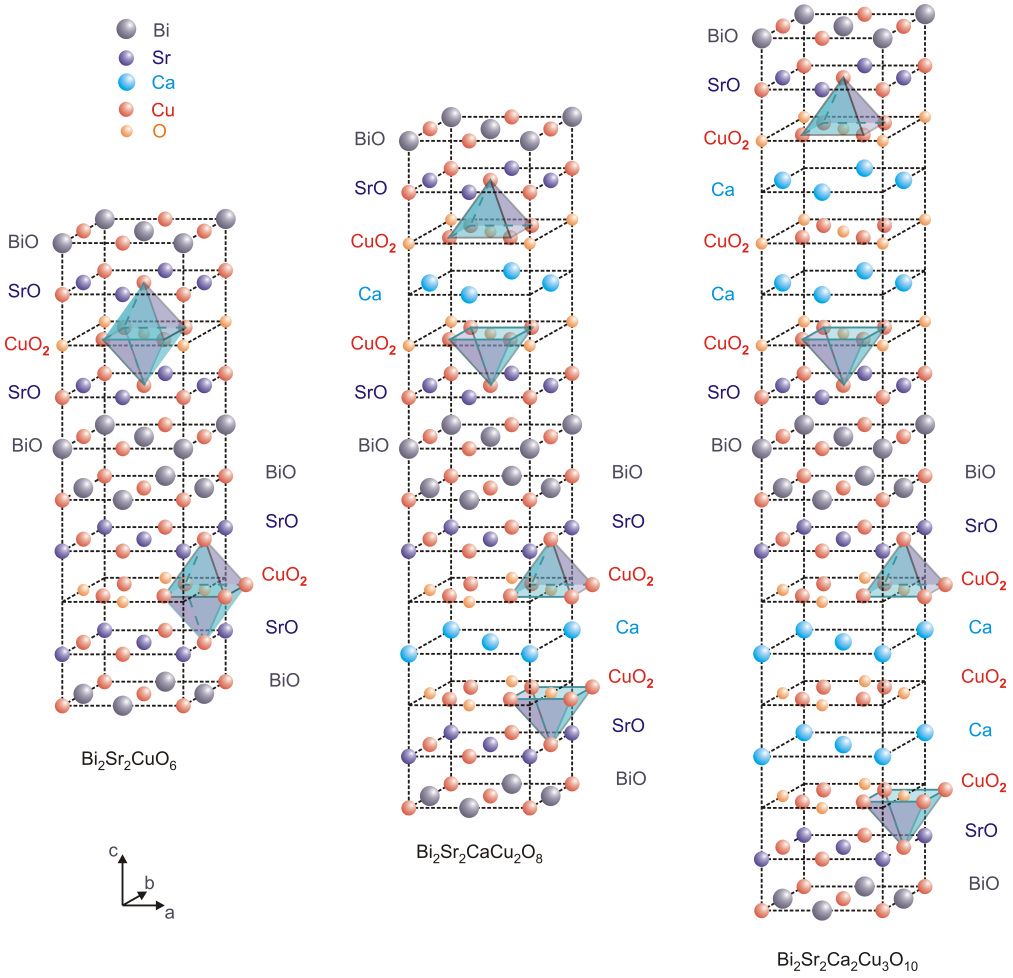

Figure 2.7: The crystalline structure of Bi-based cuprate superconductors [4]. The general formula is $Bi_2Sr_2Ca_{n-1}Cu_nO_y$ in which n = 1, 2 and 3.

ductors such as thallium and mercury systems, T_c^{max} decreases when n is more than 3 as shown in the figure 2.8. $Bi_2Sr_2CaCu_2O_{8+\delta}$ is a hole doped cuprate superconductor of Bi-based system, which has $T_c^{max} = 95$ K. In a unit cell of Bi2212, there are two CuO_2 layers separated by a Ca layer. Superconductivity occurs in the CuO_2 planes. In the case of Bi2212, both CuO_2 layers are superconducting. However in YBCO, one should distinguish the CuO_2 superconducting layer from the Cu-O chain which belongs to the charge reservoir block. Figure 2.7 shows the crystaline structure of Bi-based superconductors $Bi_2Sr_2CuO_6$ (Bi2201), $Bi_2Sr_2CaCu_2O_8$ and $Bi_2Sr_2Ca_2Cu_3O_{10}$ (Bi2223). Bi2212 has two sub-cells with 4 units of formula in one unit cell, two sub-cell are shifted $(1/2, 1/2, 0)$ with each other [4]. There is a similarity in crystalline structure between Bi-cuprates and Tl-cuprates. There is a

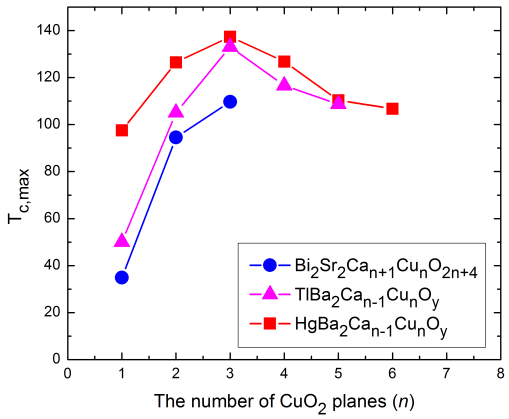

Figure 2.8: T_c^{max} with respect to number of CuO_2 layers [55].

weak binding force between BiO layers, Van der Waals force, therefore it is very easy to cleave at this layer to make a clean surface. The crystal structure of Bi2212 is pseudo tetragonal, belonging to D_{4h} group ($I4/mmm$), with lattice constants $a \approx b = 5.4$ Å and $c = 30.8$ Å [4, 56]. Values of lattice contants a and b are the same for the other Bi-cuprates, Bi2201 and Bi2223. The CuO distance in CuO_2 planes is 1.9 Å and the CuO distance along the c axis in the CuO_5 pyramid is 2.6 Å [4].

There is an incommensurate modulation of BiO layer along b axis with period $4.8b$ [57]. While the oxygen content of YBCO is easily changed, optimally doped Bi2212 samples are very stable in air at room temperature. However, Bi2212 does not have structural perfection as in YBCO. When cooling down from room temperature, LSCO and YBCO [4] have structural transitions. LSCO shows a complex structure transition between high-temperature tetragonal, low-temperature orthorhombic and low-temperature tetragonal. YBCO also has a transition between tetragonal insulating and orthorhombic metalic when oxygen content changes. On the other hand, in Bi2212 there is no structural transition.

There are certain requirements for each experimental technique. Therefore, each technique is suitable for some superconductors. Magnetic neutron scattering and optical measurements need large single crystals, therefore they are mostly used to study YBCO and LSCO. Tunneling and ARPES measurements are sensitive to sample surface, the escape length of electrons in a typical ARPES measurement

is about 5 Å and the observed depth in tunneling spectroscopy is shorter than that [58]. Therefore, they are usually used to study the Bi-based system which can be cleaved easily in vacuum leaving a fresh surface. One reason why superconductors such as YBCO are not measured by ARPES is that these superconductors have polar surfaces with charge distribution different from inside part [59] whereas Bi2212 has a neutral BiO layer on its surface. D.c. conductivity and magnetic nuclear resonance measurements are used for many superconductor because of less strict requirements in samples.

Single crystal Bi2212 was used in present study because of its properties that are suitable for both Raman and ARPES measurements. The oxygen annealing is efficient at least within a few micrometer from the sample surface, which is satisfactory for performing Raman scattering where the penetration depth of light is in order of 100 nm [58,60], and for ARPES because the escape length 5 Å is much smaller. If we compare the penetration depth of light with the lattice constant c of Bi2212, $c \approx 30.8$ Å, Raman scattering spectroscopy can be considered as a bulk probe.

Disadvantages of Bi2212 are its inhomogeneity and the structural modulation in BiO layer. Inhomogeneity could make it difficult to get a sharp superconducting transition as in the case of YBCO, and in general leads to a wide peak in measured spectra (for example, the magnetic resonance excitation at 41 meV near the $\mathbf{k}$ vector $(\pi/a, \pi/a)$ [61]). The modulation along b axis also can produce extra vibrations.

Resistivity data of Bi2212 shows metallic behavior in the ab-plane and insulating behavior in the c axis in wide range of doping. In the other cuprates, metallic behavior in the c axis is recovered in overdoped region. For other cuprates as LSCO, YBCO and Bi2201, with very low doping the insulating behavior in ab-plane also can be observed [62].

In high-T_c cuprate superconductors, from d.c transport measurements in the normal state, it was shown that there is an anisotropy of resistivity between a and b axes [62–72] and this anisotropy is about a factor of two. However the anisotropy of resistivity between ab-plane and c-axis is very large, for example the anisotropy ratio $\rho_c(T)/\rho_{ab}(T)$ in LSCO is about 300 and it can increase upto a power of 5 as in the case Bi2212, figure 2.9. Resistivity in c-axis $\rho_c(T)$ and the anisotropy ratio $\rho_c(T)/\rho_{ab}(T)$ decrease rapidly with increasing doping [63].

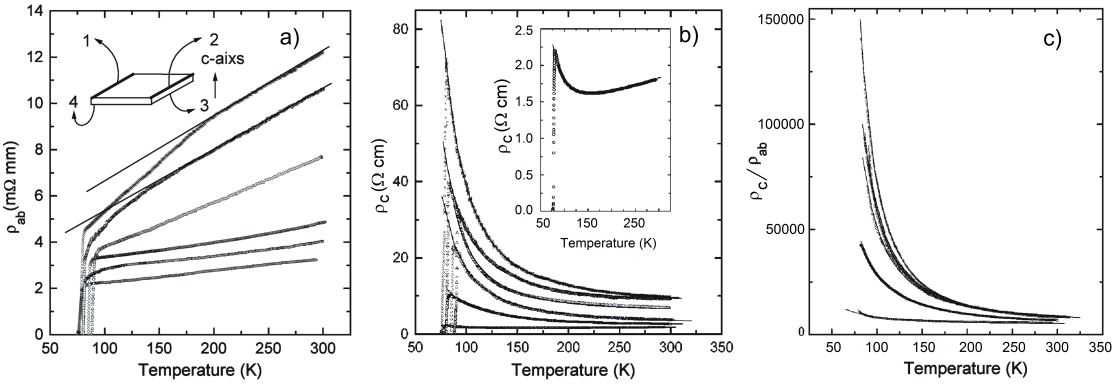

Figure 2.9: Temperature dependence of resistivity of Bi2212 single crystals with different doping from underdoped (top) to overdoped (bottom). a) in-plane resistivity ρ_{ab}. The inset shows measurement method b) out-of-plane resistivity ρ_c. The inset is the enlargement of the overdoped sample, the lowest curve. c) the ratio ρ_c/ρ_{ab} [63].

The anisotropy of conductivity was also confirmed by optical measurements [73–75]. An effective mass ratio m_c^*/m_{ab}^* estimated from plasma frequency ($\omega_p \sim \sqrt{n/m^*}$) is larger than 10^4 for Bi2212 showing that currents along c axis is a Josephson tunneling current through insulating layers BiO and conductivity is essentially dominate in the in-plane direction.

It is also clear that the anisotropy of in-plane conductivity in the normal state is not only between the a and b axes but also between the antinodal and nodal directions from magnetoresistance measurements [76]. Figure 2.10 shows the normal state resistance in the c axis of an overdoped $Tl_2Ba_2CuO_6$ single crystal as a function of the oriental angle of magnetic field $\mathbf{B}$ in ab-plane. The four fold symmetry is clear and resistance gets maxima when $\mathbf{B}$ is aligned along the (110) and equivalent directions which are 45^o to the Cu-O bonds.

The anisotropy of the effective mass between the ab-plane and the c axis also shows the anisotropy of penetration depth because $\lambda_c/\lambda_{ab} = \sqrt{m_c^*/m_{ab}^*}$. Whether 2D conductivity is necessary for high-T_c superconductivity or not is still unclear until now.

2.3 Electronic structure of parent compounds

The parent compound of cuprate superconductors is a charge-transfer insulator. The electronic band is half filled but instead of a good metal as expected from band

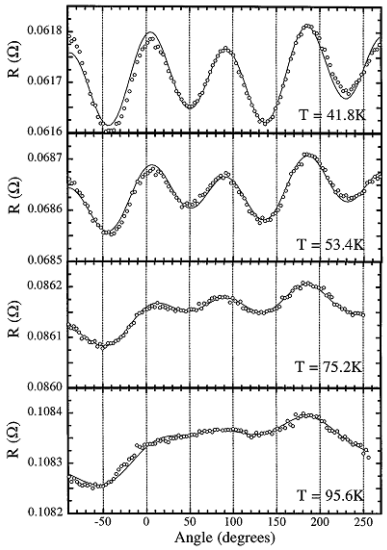

Figure 2.10: Angular dependence of the c-axis transverse magneto-resistance at various temperatures of a $Tl_2Ba_2CuO_6$ crystal with $T_c = 25$ K measured in a magnetic field B = 13 T [76].

theory it is antiferromagnetic insulator because of a strong Coulomb interaction between electrons on neighbor sites.

For simplicity we consider the cuprate superconductor $La_{2-x}Sr_2CuO_4$ which has one CuO_2 layer in a unit cell and the whole doping range can be obtained. The parent compound of this superconductor is the undoped insulating compound La_2CuO_4. There are nine electrons in the outer shell $3d$ of ion Cu^{2+} while $2p$ orbitals of O^{2-} are fully filled by 6 electrons. In a crystal field of cubic symmetry O_h with a proper octahedron CuO_6, the atomic energy level $3d^9$ of Cu splits into t_{2g} and e_g levels, the value of this splitting is 1-2 eV [4]. And because of reduction of symmetry of the octahedron to tetragonal D_{4h} with shorter bonds in the CuO_2 plane (the Cu-O bond in the c direction in the tetragonhedral is 2.4 Å whereas the in-plane Cu-O bond is 1.9 Å [4]), these energy levels split into $d_{x^2-y^2}$, $d_{3z^2-r^2}$, d_{xy}, d_{xy} and d_{yz}. The atomic energy level of O $2p^6$ in crystal field of D_{2h} splits into $p_{\pi/\!/}$, $p_{\pi\perp}$ and p_σ. The hybridization of the π-orbitals (which are perpendicular to Cu-O bonds, $p_{\pi/\!/}$ is in-plane and $p_{\pi\perp}$ is out-of-plane) with Cu orbitals is weak leading to narrows (π) bands. The oxygen σ-type states are in-plane and along the Cu-O bonds. These σ orbitals can hybridize strongly with the $d_{x^2-y^2}$ orbitals of copper leading to antibonding ($\sigma^\star$) and bonding (σ) bands. Therefore in the

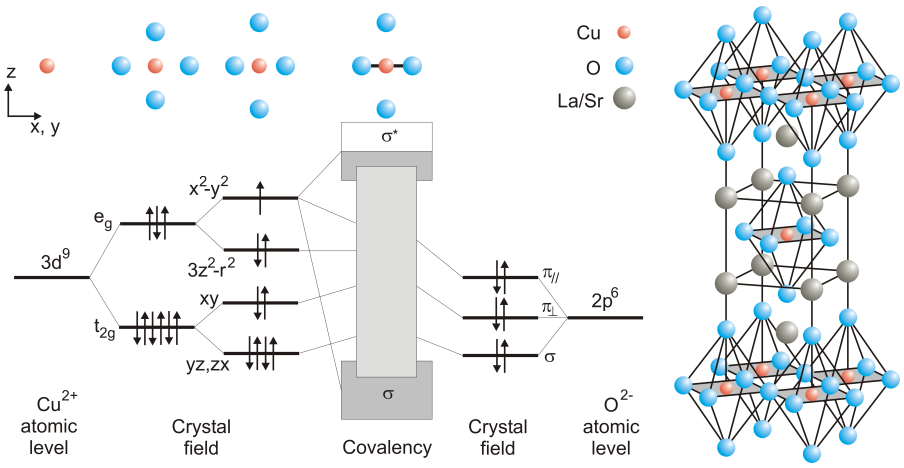

Figure 2.11: Electronic structure of the parent compound. In crystal field the atomic levels $3d^9$ of copper and $2p^6$ of oxygen spit and hybrid to make the most upper band is half-filled while the others are filled completely. The crystal structure of the cuprate $La_{2-x}Sr_2CuO_4$ with an octahedron CuO_6 is also shown [77].

upper most antibonding band, there is only one electron with spin 1/2, or in other words this band is half-filled with spin 1/2 located at Cu sites. Figure 2.11 shows the splitting and the bonding in CuO_2 plane.

On a model that charge carriers do not interact with each other and for a square lattice, the band structure can be solved from the Hamiltonian [78]

$$H_0 = \epsilon_d \sum_{i\sigma} n_{d\sigma}(i) + \epsilon_p \sum_{j\sigma} n_{p\sigma}(j) + \sum_{\langle ij\rangle\sigma} V_{ij}(d^\dagger_{i\sigma} p_{j\sigma} + p^\dagger_{j\sigma} d_{i\sigma}), \tag{2.2}$$

where $\langle ij\rangle$ is a pair of the nearest neighbors i and j. $d^\dagger_{i\sigma}$ creates a hole with spin σ in Cu $3d_{x^2-y^2}$ orbital at site i. $p^\dagger_{j\sigma}$ creates a hole in O p_x (or p_y) orbital at site j. n is operator of hole number. V_{ij} is matrix element describing the hybridization between two types of orbital, $V_{ij} = (-1)^{\alpha_{ij}} t_{pd}$ with t_{pd} is hoping integral, and $\alpha_{ij} =$ 0 or 1 depending on relative position of the O atom to the Cu atom.

Figure 2.12 [77] shows configurations of p-d bonding between oxygen atoms and copper atoms making bonding, non-bonding and antibonding bands, together with the band structure calculated from the Hamiltonian 2.2. The parent compound should be a good metal but an insulator gap with values 1-2 eV was found from experiments in undoped stoichiometric cuprates La_2CuO_4 and $YBa_2Cu_3O_6$ [4]. A similar problem was solved by N. F. Mott and J. Hubbard previously for compounds so called Mott insulators, where repulsion interaction between electrons on neighbor

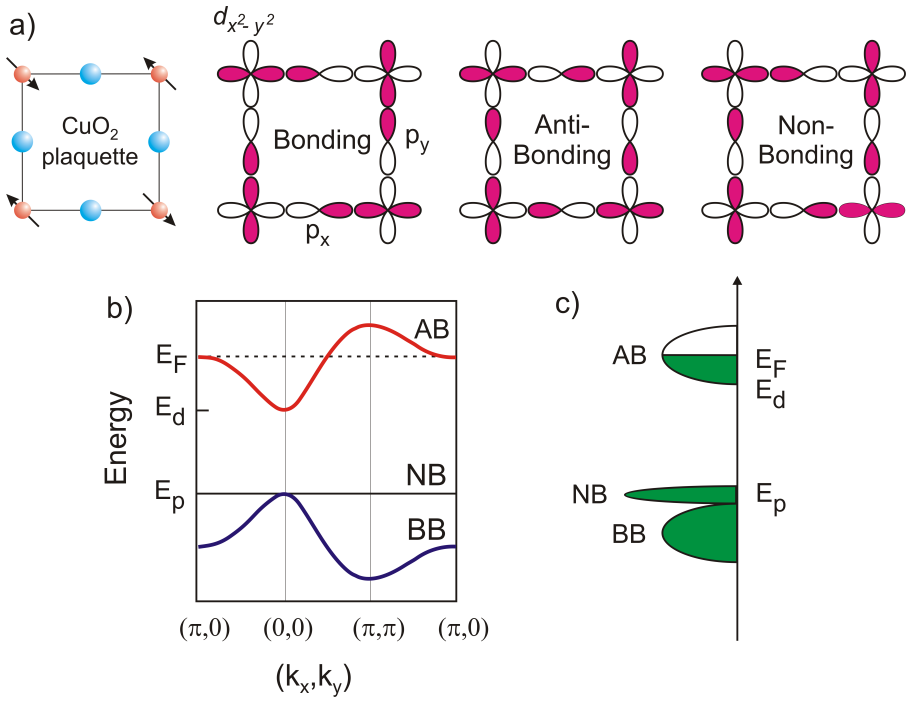

Figure 2.12: a) CuO_2 plaquette and phase at (π, π) of Cu $d_{x^2-y^2}$ and O p orbitals for bonding, antibonding, and nonbonding hybridized wave functions b) Band calculation obtained from tight-binding model, 2.2, in which only nearest-neighbor hopping is concerned c) corresponding density of states [55, 77].

sites is taken into account.

A multi-band Hubbard Hamiltonian containing d states on Cu sites, p states on O sites, hybridization between Cu and O states, hybridization between O and O states, and Coulomb repulsion terms can be used to describe the electronic structure of the parent compound of the cuprates [55, 79]

$$\begin{aligned} H =& \epsilon_d \sum_{i\sigma} d^\dagger_{i\sigma} d_{i\sigma} + \epsilon_p \sum_{j\sigma} p^\dagger_{j\sigma} p_{j\sigma} \\ &+ t_{dp} \sum_{\sigma\langle ij\rangle} (d^\dagger_{i\sigma} p_{j\sigma} + h.c.) + t_{pp} \sum_{\sigma\langle jj'\rangle} (p^\dagger_{j\sigma} p_{j'\sigma} + h.c.) \\ &+ U_d \sum_i n^d_{i\uparrow} n^d_{i\downarrow} + U_p \sum_j n^p_{j\uparrow} n^p_{j\downarrow} + U_{pd} \sum_{\sigma\langle ij\rangle} n^d_{i\sigma} n^p_{j-\sigma}, \end{aligned} \tag{2.3}$$

where the operator $d^\dagger_{i\sigma}$ creates a hole in $3d_{x^2-y^2}$ orbital at Cu site i, and $p^\dagger_{j\sigma}$ creates a hole in $2p_x$ (or $2p_y$) orbital at O site j. $d_{i\sigma}$ and $p_{j\sigma}$ are correspondingly annihilation operators. U_d is the on-site Coulomb repulsion between two holes on a Cu site and the U_p is the similar quantity for O site. The third term is the

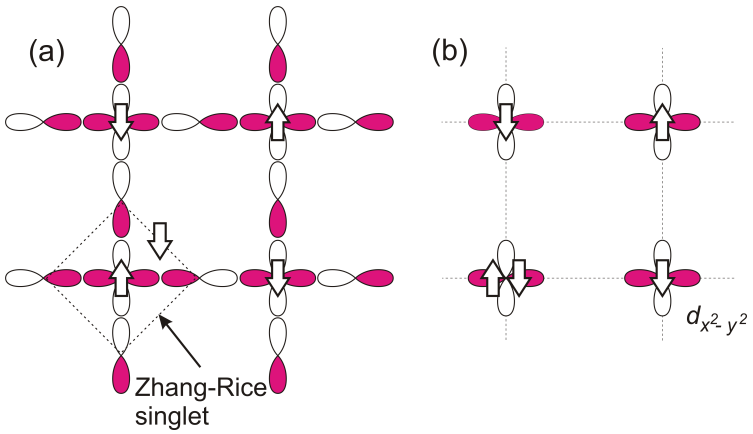

Figure 2.13: a) A hole is doped in the oxygen site of CuO_2 plane, and the d hole and p hole create a Zhang-Rice singlet b) The Zhang-Rice singlet makes an effective one band model with only $d_{x^2-y^2}$ band is considered [55].

direct overlap between Cu orbitals and O ones. The fourth term is direct hopping between nearest-neighbor oxygen orbitals, and U_{pd} in the sixth term is the Coulomb repulsion between holes on nearest neighbor Cu and O atoms. With this model, a three-band model (or p-d model) including bonding (B), nonbonding (NB) and the half-filled antibonding (AB) band, and because the Coulomb repulsion potential $U_d \sim 8 - 10$ eV is much larger than the typical width of the antibonding band $W \sim 3$ eV [4], the antibonding band is split into a upper Hubbard band and a lower Hubbarb band. If we consider the energy of anion-cation charge transfer Δ_{pd}, here $\Delta_{pd} = E_d - E_p$, there are two cases. One case is the Coulomb interaction is smaller than the charge transfer energy, $W < U_d < \Delta_{pd}$, we have antiferromagnetic Mott-Hubbard insulator. The other case is the Coulomb interaction larger than the charge transfer energy, $U_d > \Delta_{pd} > W$. In our case of the parent compound of the cuprates, because U_d is larger than the charge transfer energy $\Delta_{pd} = E_d - E_p = 3 - 4$ eV [4], the material is a charge-transfer insulator instead of a Mott-Hubbard insulator.

The three-band model above can be simplified into an one-band model, after the work by F. C. Zhang and T. M. Rice [80], which can be applied for low-energy physics of high-T_c superconductivity. They considered a CuO_4 plaquette where one Cu atom is surrounded by four O atoms as in the figure 2.13, and with a doped hole. Because the Coulomb repulsion interaction at Cu site is large, the hole will locate on one p orbital of the O sites. The hole at O site can be in symmetric

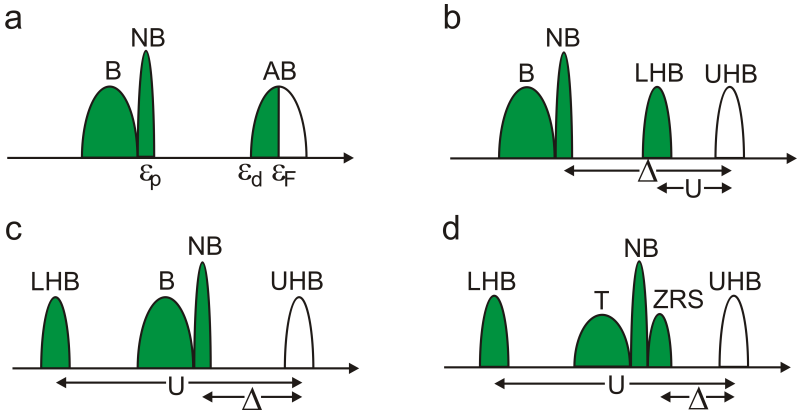

Figure 2.14: Different types of electronic structure a) a metallic state of AB band for Mott-Hubbard potential $U_d = 0$, (b) a Mott-Hubbard insulator for $\Delta_{pd} > U_d > W$, (c) a charge-transfer insulator for $U_d > \Delta_{pd} > W$ and (d) charge-transfer insulator with a splitting of bonding band into a triplet T ($S = 1$) and a Zhang-Rice singlet ZRS ($S = 0$) [4, 77].

or antisymmetric states (parralel or antiparallel) to the state of the d orbital hole on the Cu site, center of plaquette. These states can combine or hybridize to form a triplet (spin S=1) and a singlet (S=0), respectively. From calculation in pertubation theory, F. C. Zhang and T. M. Rice have shown that the singlet state has the lowest energy, i.e the hybridization in singlet state is the strongest. The separation energy between singlet and triplet is as large as 3.5 eV as calculated by H. Eskes et al. [81], and this rules out the role of the triplet in low-energy physics. The hole at first locating at oxygen site is now replaced by the singlet at copper site as shown in figure 2.13. Hopping of the Zhang-Rice singlet (ZRS) between the CuO_4 plaquettes over the entire CuO_2 plane can be described by an effective Hamiltonian which is for a single Hubbard model. And as shown by Zhang and Rice, that effective Hamiltonian is the one of t-J model [77, 80]

$$H = -t \sum_{\langle ij \rangle \sigma} [c^{\dagger}_{i\sigma}(1 - n_{i-\sigma})(1 - n_{j-\sigma})c_{j\sigma} + H.c.] + J \sum_{\langle ij \rangle} \left[S_i \cdot S_j - \frac{1}{4} n_i n_j \right], \quad (2.4)$$

where $c_{i\sigma}(1-n_{i-\sigma})$ excludes double occupancy, $J = 4t^2/U$ is the antiferromagnetic exchange coupling constant, and S_i is the spin operator.

Figure 2.14 summarizes different types of electronic structures discussed above. The Hubbard models can explain the antiferromagnetic insulating state in the undoped parent compound, however it is unclear until now how the charge transfer

insulator evolves into the metallic states. Even though, the present study was performed in view of the single-band Hubbard model.

2.4 Pseudogap

The origin of pseudogap is not clear upto now and it is believed that understanding the origin of pseudogap can solve the problem of high-T_c superconductivity in cuprates and therefore pseudogap has been studied and discussed intensively. Pseudogap state is the state just above T_c in which there is a gap. The gap opens more when the superconductor goes into the superconducting state. The pseudogap usually manifests itself as a suppression of a spectral weight in low energy region when temperature decreases and usually observed in underdoped samples (figure 2.3). This behavior was observed by many techniques in many superconductor cuprates [82] but we do not know its role in superconductivity [83]. The pseudogap was first discovered in nuclear magnetic resonance measurements where suppression of spin-lattice relaxation rate above T_c (61 K) was observed in a underdoped $YBa_2Cu_3O_{6.7}$ sample [84, 85]. The spin-lattice relaxation rate relates to magnetic susceptibility which should be constant as expected for a Pauli paramagnetism, therefore the suppression makes a gap in magnetic susceptibility above T_c and the gap was considered as a spin gap. The pseudogap temperature, usually denoted by T^*, at which the gap starts to open/close was observed as high as 100 K. Experiments after that also uncovered the existence of a gap above T_c. For example, from transport measurement, as one can see in the figure 2.9, there is deviation from T-linear behavior in *ab*-plane resistivity of underdoped Bi2212 samples starting at a temperature above T_c as high as 190 K for the underdoped sample with $T_c = 76$ K, and 150 K for the sample $T_c \approx 80$ K. The change in slope of resistivity in the pseudogap state can be understood as a decrease of scattering due to opening of a gap.

The data of *ab*-plane optical conductivity of underdoped Bi2212 also shows opening of a gap from a temperature above T_c to well below T_c, continuously through superconductivity transition temperature T_c. This behavior can support for the idea that the pseudogap is the precursor of superconductivity. However this gap is very strange because the gap size is quite large comparing to $k_B T_c$. As one example the data from J. Hwang et al. [86] is presented in the figure 2.15. In

this data the change of spectra in the pseudogap state was observed for a wide range of doping of the T_c dome. There are three scenarios of the phase diagram. First, the pseudogap might open and stop at T_c, this is competition between the pseudogap and superconductivity. Second, the pseudogap also covers all T_c dome then it could be a precursor of superconductivity. Third, the pseudogap opens and exists independently of superconductivity, in this case the pseudogap phase could cross T_c dome [83].

Scanning tunneling spectroscopy (STS) measures density of state in both occupied and unoccupied states in real space. Pseudogap was obtained from STS measurements in a underdoped Bi2212 sample with $T_c = 83$ K [87] and specially in a range from underdoped to overdoped Bi2212 [88] as well as in overdoped Bi2201 [89]. Similar to ARPES results, there is a gap which opens at temperature above T_c in the antinodal region and continuously evolves into superconducting state supporting for being precursor of superconductivity. As a precursor of superconductivity pseudogap is understood to be the phase where pairing is formed but not in long range. There is one review in STS data by Ø. Fischer [11]. Figure 2.16 shows the data of Ch. Renner et al. on Bi2212 in comparison with STS data of Nb where a gap opens just below T_c [11].

ARPES probes electronic structure of materials and it is an energy and momentum resolved measurement. Therefore, it is a strong tool to figure out the existence of an energy gap such as the pseudogap. Indeed, ARPES data shows clearly a gap above T_c, some first data was presented in Refs. [42, 90]. Figure 2.17 a)-c) shows temperature dependence of ARPES EDC spectra of a underdoped sample measured at different k-points a, b and c on the Fermi surface. The EDC spectra of a polycrystalline Pt which is connected electrically to the sample, were also taken as references and to determine the chemical potential. It is clear that for point a and b, the shift of leading edges of EDC spectra starts at temperatures above T_c, 150 K and 120 K, respectively, which show opening of a gap. This gap opens continuously into the superconducting state, and because at temperatures well below T_c, the superconducting gap has d-wave symmetry, it implies that pseudogap also has the same symmetry. Whereas at the point c, a gap opens just below T_c. This behavior shows existence of a Fermi arc around the nodal region and a pseudogap in the antinodal region. The panel **e** shows clearer about evolution of gap value in antinodal region with lowering temperature [91].

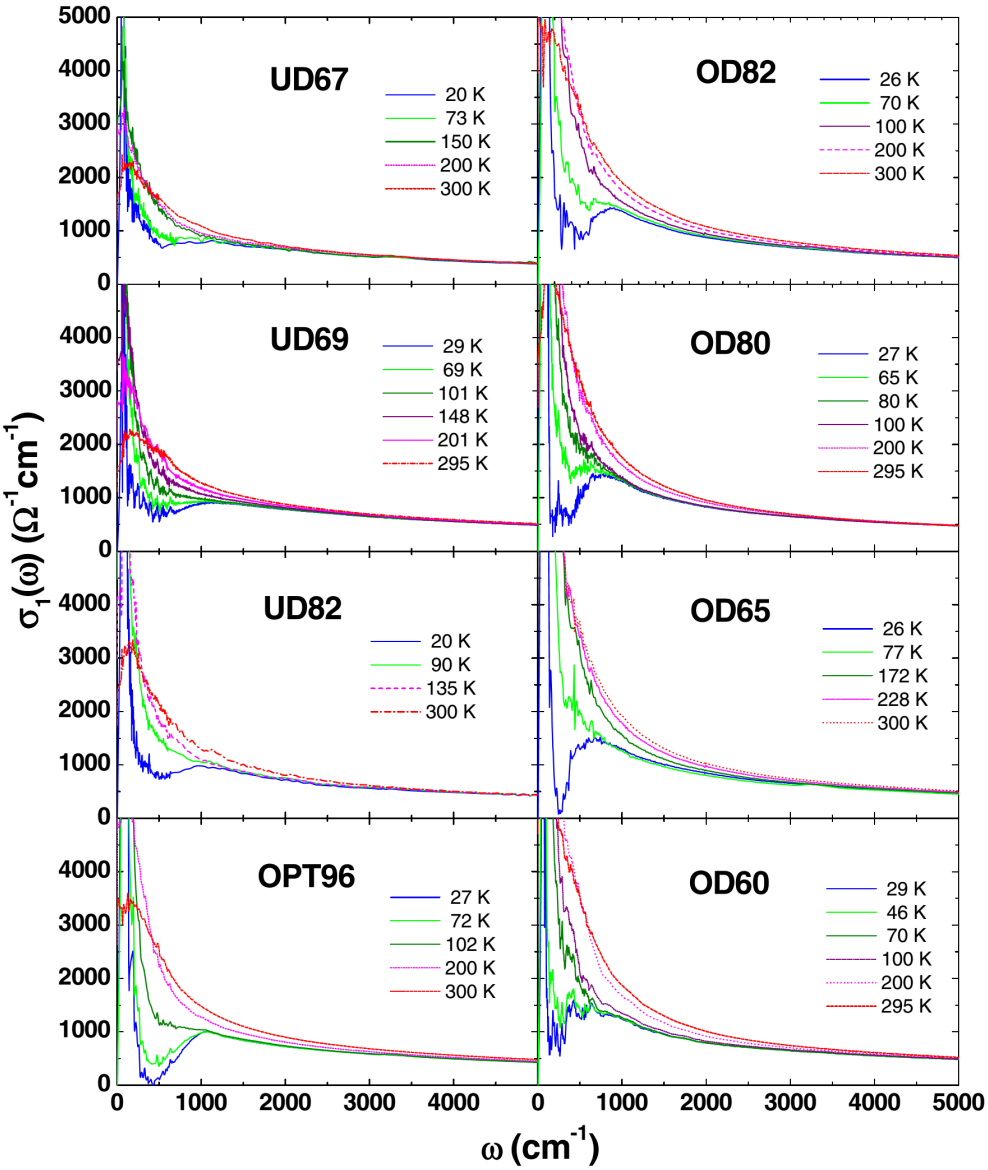

Figure 2.15: Temperature and doping dependences of *ab*-plane optical conductivity of Bi2212. The suppression of spectra in low frequency region in the normal state was observed in underdoped to optimally doped samples [86].

As presented previously (figure 2.6), there is a deviation from *d*-wave symmetry of gap function in the antinodal region of heavy underdoped samples. This deviation could be originated from the pseudogap. With this viewpoint, the pseudogap and the superconducting gap are distinct.

While ARPES is a strong tool to capture the pseudogap, Raman is not. The pseudogap in Raman is very subtle. Previously there are some studies showing

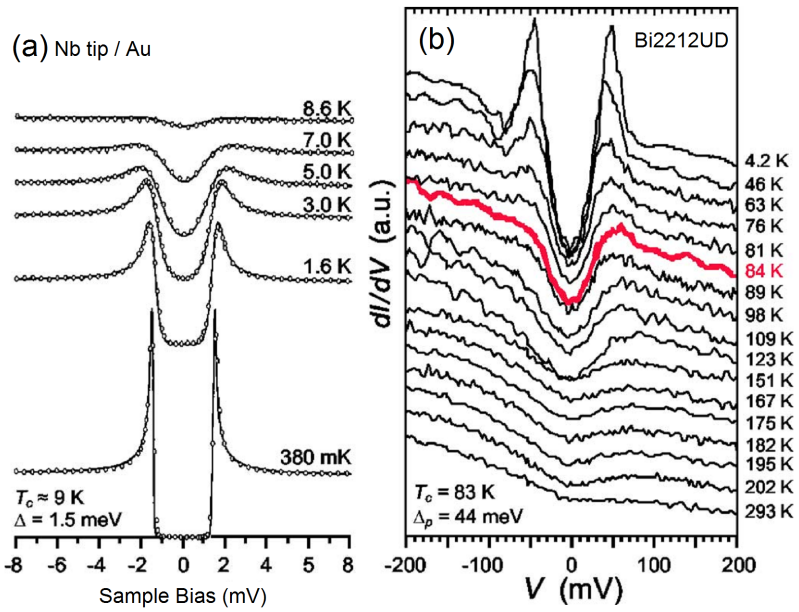

Figure 2.16: Pseudogap observed by scanning tunneling microscope (STM). a) Temperature dependence of density of state of Niobium, a conventional superconductor. It is well known that the gap closes at $T_c = 9$ K although it is not clear in this figure. b) A pseudogap exists above $T_c = 83$ K of a underdoped Bi2212 sample and opens continuously at T_c into a superconducting gap [11].

that psedogap occurs in B_{2g} but not B_{1g} spectra, where there is suppression of spectral weight with decreasing temperature [92–95]. This is strange from the ARPES viewpoint because in ARPES pseudogap open in the antinodal region where B_{1g} probes. One difficulty in capturing the pseudogap in B_{1g} spectra is that B_{1g} spectral intensity decreases with underdoping leading to smaller resolution. There are also some studies inversely reporting the pseudogap in B_{1g} but not B_{2g} spectra [96,97] however the authors did not take into account the Bose factor hence it is hard to have exact conclusions. Recently, W. Guyard et al. [98] reported B_{1g} pseudogap in underdoped Hg2201 with $T_c = 92$ K, S. Sakai et al. [99] and A. Sacuto et al. [100, 101] reported pseudogaps both in B_{1g} and B_{2g} spectra of underdoped Bi2212 $T_c = 75$ K and specially clear in the B_{1g} spectrum. Figure 2.18 presents the data of A. Sacuto for pseudogap in Bi2212 UD75K sample, the pseudogap temperature from this data is as high as 150K or 180K.

From this data the pseudogap manifesting in B_{2g} is not strong and at intermediate energy region instead of low energy region, which also can be seen in data

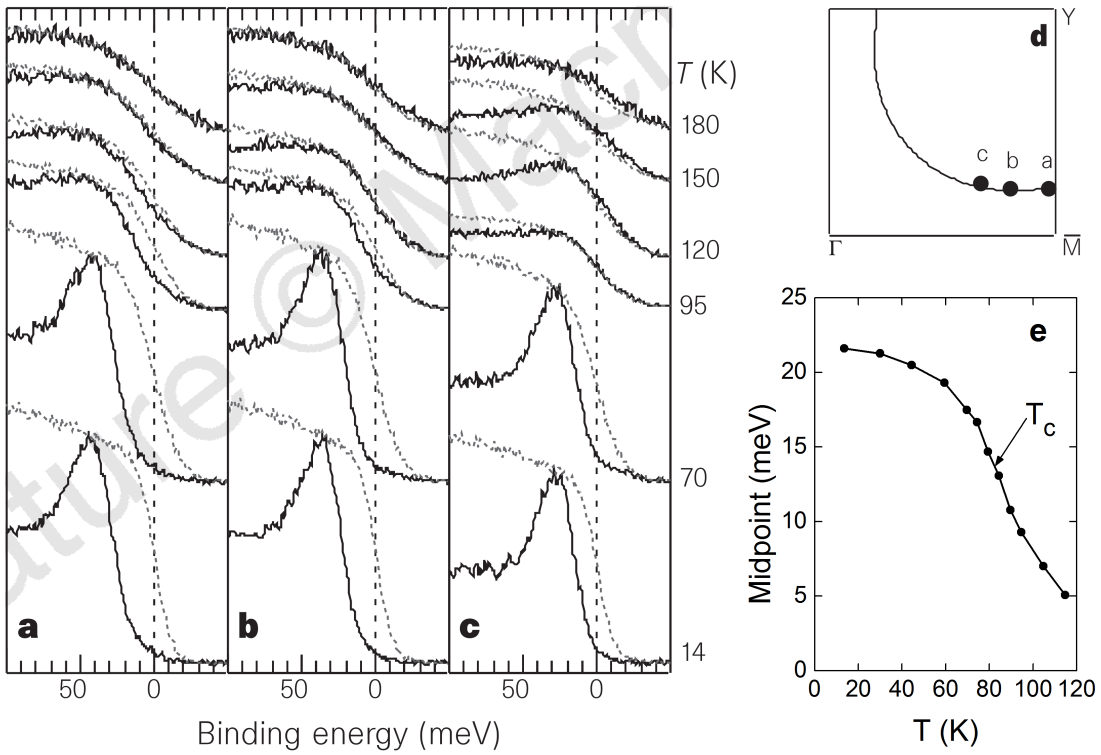

Figure 2.17: Pseudogap obtained by ARPES. a)-c) Temperature dependence of ARPES EDCs of a underdoped Bi2212 sample ($T_c = 85$ K) taken at k-points a, b and c shown in d), respectively. The dotted curves are reference spectra of a polycrystalline Pt which is electrically connected to the sample to determine the chemical potential. The shift of the leading edge is clear in for points near $(\pi, 0)$, points a and b [90]. e) Smooth evolution through T_c of a midpoint of the leading edge of an ARPES EDC taken near $(\pi, 0)$ of an $T_c = 83$ K underdoped Bi2212 [91].

of M. Opel et al. [94]. S. Sakai et al. [99] and A. Sacuto et al. [100] discussed this behavior as a s-wave pseudogap. It is different from the other data such as ARPES where pseudogap develops smoothly into the superconducting state and manifests a d-wave gap as the same as superconductivity. Because the pseudogap is not observed in many samples, from many materials and by many groups with Raman technique, the pseudogap in Raman data should be studied more.

2.5 Theory for high-T_c superconductivity

Mechanism of high-T_c cuprates is under debate. In BCS conventional superconductors the mechanism is related to phonons. Although there are some supports

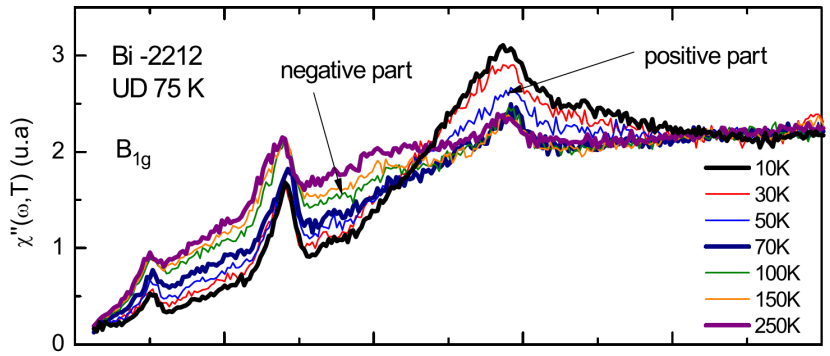

Figure 2.18: Evolution of B_{1g} spectra with temperature of a underdoped Bi2212 sample ($T_c = 75$) K from well above T_c to well below T_c shows a suppression (negative part) and an emergence (positive part) in different energy regions. The suppression in low energy region in the normal state occurs continuously similar to other techniques [100].

for the phonon mechanism for high-T_c cuprates there is no consensus and no rigid evidence for it. Besides, because of the proximity of superconductivity to antiferromagnetism, a magnetism-mediated mechanism is possible. Spin fluctuation, proposed by P. Monthoux and D. Pines, was used to explain superconductivity in heavy-fermion superconductors. In this theory, for the parent compound with half-filling, the spin state is fixed on copper atoms. By carrier doping, an electron can move to a new position and its spin will affect other spins around and then make a new pattern of spin lattice. Recently a coexistence of superconductivity and antiferromagnetism was observed in many iron-based superconductors although it is not clear that superconductivity and antiferromagnetism are in separated phases or only in one phase [102,103]. If spin fluctuation is the mechanism of superconductivity, this is totally different from BSC superconductors where superconductivity and magnetism compete with each other. To study the effect of magnetism both magnetic and non-magnetic impurities such as Zn and Ni were doped, however both types of substitution show decrease of T_c [104]. Another theory for high-T_c cuprates which people now concentrate on, that is resonating-valence-bond theory. This theory was proposed by P. Anderson in which neighboring copper atoms share their electrons which have opposite spins making a valence bond with electrons in a singlet state. With doping and at low temperatures the electron pair becomes mobile and can move in the superconductor [105].

2.6 Puzzles in Raman and ARPES

In study of high-T_c cuprate superconductors, by electronic Raman scattering measurements, with B_{1g} geometry one can get information around the antinodal region while with B_{2g} geometry we can measure the nodal region. General viewpoint from Raman data is that B_{2g} peak energy traces T_c in a T_c-dome but B_{1g} peak energy does not, B_{1g} peak energy increases monotonically with underdoping as one can see in figure 2.19. Two different doping dependences of B_{1g} and B_{2g} peak energies could imply two energy scales in cupartes and it is unclear which one or both of them relate directly to the mechanism of superconductivity because both B_{1g} and B_{2g} peaks become stronger below T_c, and B_{2g} but not B_{1g} traces to T_c. Therefore, there is one puzzle in Raman data that *what is the* B_{1g} *peak?* Does it relate to the pseudogap? ARPES pseudogap energy in the cuprates also increases with underdoping as B_{1g} peak energy does. The pseudogap opens continuously into the superconducting state and B_{1g} peak develops stronger and stronger below T_c. However, in the normal state the pseudogap exists clearly whereas the change of the electronic Raman spectra is not widely confirmed. Therefore, the relationship between the B_{1g} peak and the pseudogap is still an open question.

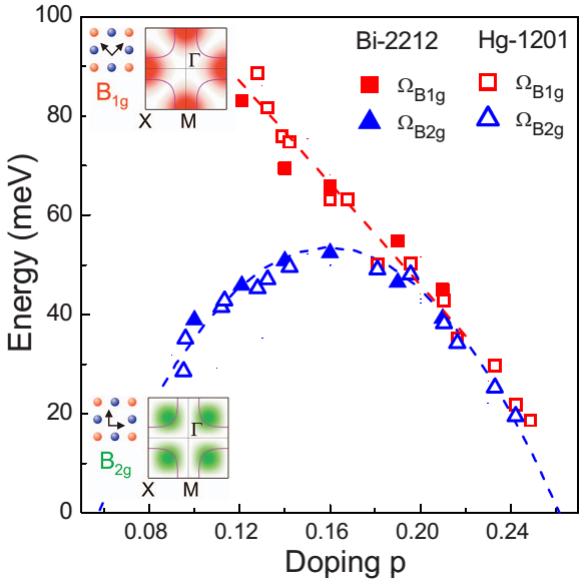

Figure 2.19: Doping dependence of B_{1g} and B_{2g} Raman measured at temperature well below T_c [45].

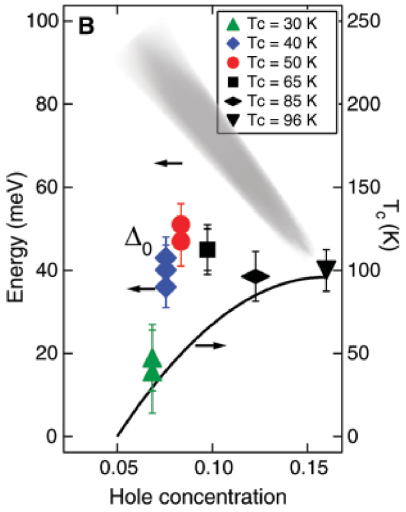

Figure 2.20: Doping dependences of the ARPES antinodal gap (the shaded area) and the ARPES nodal gap Δ_0 [51] (Δ_0 is defined in figure 2.6).

In ARPES data, it is also clear that the ARPES antinodal and nodal gaps show different doping dependences (figure 2.20). Both of them do not follow the T_c-dome. By underdoping, the antinodal gap also increases as the B_{1g} peak energy, and the same tendency with ARPES pseudogap in the normal state. And it should be reminded that there is a deviation from *d*-wave pairing in the antinodal region of ARPES antinodal gap (figure 2.6), which can be caused by the pseudogap. Therefore, one puzzle in ARPES data is that *what is the ARPES antinodal gap?* Does it relate to the pseudogap?

Comparing Raman and ARPES data, there are many groups reporting that B_{1g} Raman peak energy is the same as the antinodal gap in ARPES, figure 2.21 a). On the other hand, some groups show that their energies are different. It seems that B_{1g} Raman peak energy is lower, figure 2.21 b). Therefore one question raised is which scenario is correct. And if B_{1g} Raman peak energy is different from energy of ARPES antinodal gap, then the B_{1g} Raman peak should be understood more clearly.

While B_{2g} peak energy traces T_c as a quadratic function of doping, the tendency of the nodal gap from ARPES is nearly unchange in the doping range 0.15-0.2 and abruptly decreases below 0.08, figure 2.22 [107]. Therefore understanding the doping dependence of B_{2g} peak energy from the electronic structure obtained by ARPES should be clarified.

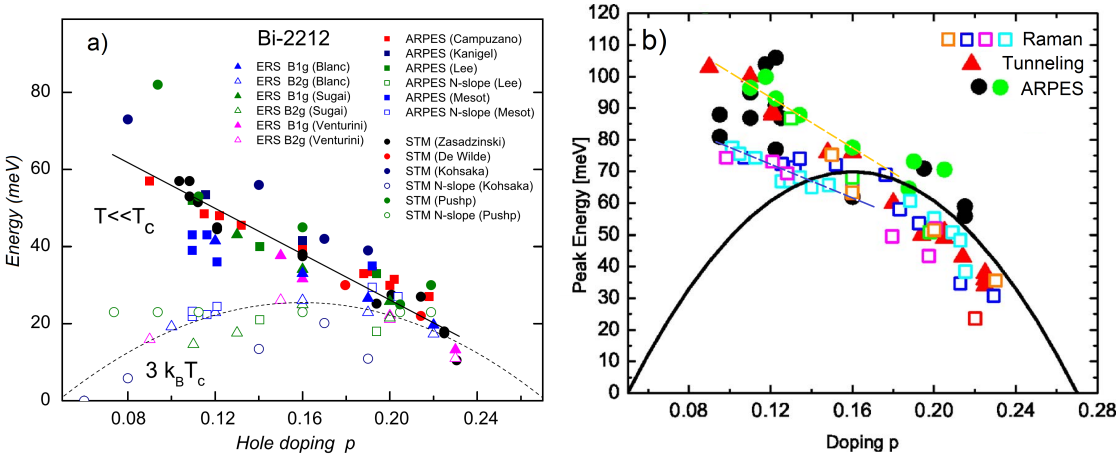

Figure 2.21: Different viewpoints on Raman and ARPES data. a) Raman and ARPES are the same, the B_{1g} peak energy and the ARPES antinodal gap keep increasing with underdoping in the same line [100]. b) Raman and ARPES are different, B_{1g} peak energy is lower than the ARPES antinodal gap [106].The two dashed lines are added to guide eyes, the green line is for ARPES data and the blue one is for Raman data.

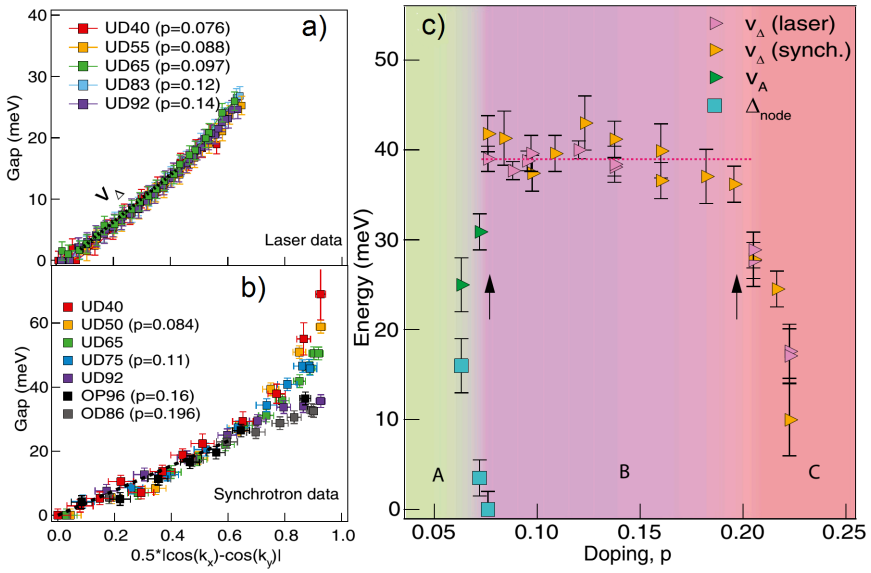

Figure 2.22: The nodal gap is unchange in the doping range 0.08-0.2 and drops in both sides. a) and b) the gap profiles along Fermi surfaces of Bi2212 with different dopings. c) The nodal gap, an extrapolation value of the linear *d*-wave gap at the antinodal region, divides the doping range into three regions A, B and C [107].

2.7 Open problems of previous ERS calculations

There are some calculations for electronic Raman spectra, which are successful in some aspects but still not fully satisfied. The early kinetic theory calculation proved that the polarization dependence of Raman spectra indicates a *d*-wave pairing symmetry in cuprates. It shows that the B_{1g} Raman peak is located at $2\Delta_0$ (the maximum gap) which means that the B_{1g} peak originated from superconductivity. However, as mentioned above, the relationship between $2\Delta_0$ and T_c is strange. The kinetic theory calculation successfully explained the ω-cubic and ω-linear behaviors of B_{1g} and B_{2g} spectra, respectively. Nevertheless, to get a good agreement with experimental data a scattering rate must be applied, which allows to broaden the theoretical spectra (see more in section 5.1.1). This scattering rate was larger than the value based on ARPES data.

Trying to explain the two-energy-scale behavior of B_{1g} and B_{2g} spectra, A. Sacuto's group [45, 100, 108] calculated electronic Raman spectra, based on kinetic theory where a parameter so called quasiparticle spectral weight $Z\Lambda$ was introduced, as in equation 2.5. This parameter enhances excitations in a Fermi arc around the nodal point and acts as a key role controlling the doping dependence of B_{1g} peak intensity as well as the opposite tendencies of the Raman peak energy in the underdoped region. The Raman response χ'' as a function of Raman shift Ω including the spectral weight parameter is

$$\chi''_{B_{1g},B2_{2g}}(\Omega) = \frac{2\pi N_F}{\Omega}\left\langle \gamma^2_{B_{1g},B2_{2g}}(\phi)(Z\Lambda)^2(\phi)\frac{\Delta^2(\phi)}{\sqrt{\Omega^2-4\Delta^2(\phi)}}\right\rangle_{FS}, \tag{2.5}$$

where N_F is density of state at Fermi level, γ is a Raman vertex, ϕ the angle described in figure 2.23, $\langle\cdots\rangle$ denotes an average along the Fermi surface. In this model, T_c will be simply controlled by a fraction of the Fermi surface called Fermi arc $k_BT_c \sim f_{arc}\cdot\Delta_{max}$ which is the arc around the nodal point. There are some reports sharing the same viewpoint about the relationship between an Fermi arc and T_c [109]. Step-like function of $Z\Lambda$ restricts the real contribution of all the Fermi surface to the Raman response. The calculation was performed simply only for the Fermi surface and with three scenarios where symmetry of the gap profile is in *d*-wave and not in *d*-wave. All of these scenarios show results with the same behaviors of B_{1g} and B_{2g} spectra explaining successfully two energy scales as shown in the figure 2.23 d) and e), in which the *d*-wave gap with different slopes of gap

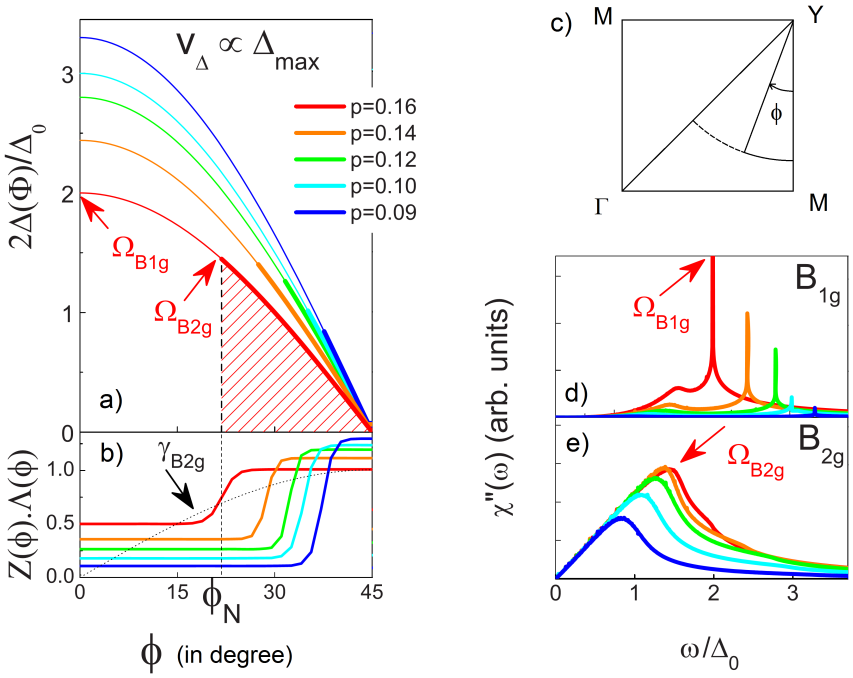

Figure 2.23: One of the three scenarios was proposed to explain two energy scales in ERS data of cuprates using kinetic theory. a) The doping dependence of gap profile along the Fermi surface. The gap profile of the underdoped sample has larger gap and higher nodal velocity than the optimally doped one. The B_{1g} peak energy is affected by full gap size Ω_{B1g} while the B_{2g} peak energy is affected by energy Ω_{B2g} which is corresponding to a Fermi arc and is controlled by the function $Z(\phi)\Lambda(\phi)$ shown in b). ϕ is the angle along the Fermi surface and is described in c). b) A simple type of $Z(\phi)\Lambda(\phi)$ function was chosen to enhance the contribution from the Fermi arc as well as control the length of the Fermi arc. c) Illustration for the Fermi surface of hole-doped cuprates and the angle ϕ. d) and e) Doping dependences of the calculated B_{1g} and B_{2g} spectra, respectively, which show the two-energy-scale behavior [45]. However, the scenario is different from the doping dependence of experimental gap profiles of Bi2212 along the Fermi surface obtained from ARPES [53, 107], figure 2.22.

profile at the node (a velocity which is proportional to the maximum gap in the antinodal region) shows a good quantitative agreement with the other ARPES data on the Fermi arc. However, this (the best) scenario of doping dependence of gap function, in which the slope of gap profiles along the Fermi surface at the nodal region increases with underdoping, is not consistent with the ARPES data as shown in figure 2.22 [53, 107], where the velocity at the node is the same in a wide range of doping. In addition, the calculated spectra look simple as other calculations based on the kinetic theory.

Recently, there is a study presented by W. Prestel et al. [110] for electronic Raman spectra. In that study the authors tried to figure out the many body effect based on self-energy analysis from ARPES data. The authors calculated Raman B_{1g} and B_{2g} spectra in the normal state as well as in the superconducting state and compared to the experimental data of LSCO and Bi2212 with different dopings. Figure 2.24 shows the results obtained by W. Prestel et al. They got quite good fits in overdoped side of T_c dome $p > 0.21$ and in the normal state. However for overdoped samples in superconducting state as well as underdoped, optimally doped regions in both the normal and superconducting states, they did not succeed specially in B_{1g}.

To get these results, they did as follow. For the normal state, starting from a self-energy function which is a complex function of energy and temperature, including a real part and an imaginary part $\Sigma = \Sigma' + i\Sigma''$. The imaginary part is of the form

$$\Sigma'' = -\left[\sqrt{(\alpha\omega)^2 + (\beta T)^2 + c_0^2} + c_k\right], \tag{2.6}$$

which is inspired by the marginal Fermi-liquid approach. The quantities α, β, c_0 and c_k are parameters. The real part is deduced from the imaginary part by using

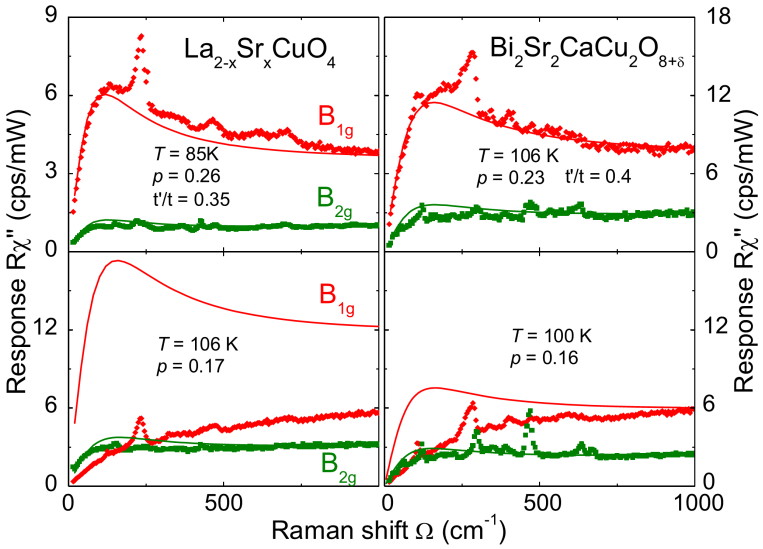

Figure 2.24: Calculation results for ERS B_{1g} and B_{2g} spectra in normal state using ARPES data and a model for self-energy (the thin smooth curves) in comparison to experimental data (the bold dotted curves) of overdoped and optimally doped LSCO and Bi2212 samples. The good fit is obtained for overdoped region [110].

Kronig-Kramers relation. Using the tight-binding model for band structure where coefficients nearest and next nearest neighbor hopping integral t, t' and chemical potential μ are chosen suitably for each superconductors, Bi2212 and LSCO.

Experimental ARPES spectra were reproduced satisfactory to get a set of the parameters for self-energy function. After that the matrix of Green's functions, which is a 2 by 2 matrix, can be obtained from the band structure and self-energy. And finally, electronic Raman responses in Nambu representation can be read as

$$\chi_{\gamma,\Gamma}(i\Omega) = \frac{T}{N}\sum_{k,\sigma}\sum_{m} Tr\left[\hat{\gamma}(\mathbf{k})\hat{G}(\mathbf{k}, i\omega_m)\hat{\Gamma}(\mathbf{k})\hat{G}(\mathbf{k}, i\omega_m + i\Omega)\right], \qquad (2.7)$$

which can be reproduced from Green's functions. Here γ and Γ respectively are bare and renormalized Raman vertices represented in matrix form through Pauli matrices, N is number of k-points, σ is spin, ω_m and m denote Matsubara frequencies, Tr denotes the trace of the matrix and $\hat{G}$ is the matrix of Green's functions. The self-energy can give information about interactions between particles therefore in general the approach could tell us the mechanism in high-T_c cuprates.

For the superconducting state, they followed the phenomenology of D.S. Inosov et al. [111] that can give the imaginary part of self-energy which includes an eletron part and a boson part, $\Sigma'' = \Sigma''_{el} + \Sigma''_{bos}$. The electron part $\Sigma''_{el} = \alpha\omega^2$ is the Fermi-liquid component of the scattering rate that originates from the electron-electron interactions, and the boson part Σ''_{bos} models the coupling to a bosonic mode, which is different between nodal region and antinodal region.

The conclusion from W. Prestel is that there is no equivalent between Raman and ARPES in superconducting state and for optimally doped and underdoped regions where the effect of the pseudogap could exist. And because of no match between ARPES and Raman, it is possible to need another type of self-energy that expresses for a new type of interaction instead of marginal Fermi liquid. In their model, they obtained self-energy information only from nodal spectral and applied for the whole BZ (momentum independent self-energy), which may cause the difference between Raman and ARPES.

2.8 Purposes of present study

To solve the puzzles related to superconducting gap problems in high-T_c superconductivity: (i) what is the B_{1g} peak? and (ii) what is the ARPES antinodal gap?,

we need a unified picture to understand the Raman and ARPES data.

In this study, the approach is as follows. We measure Raman spectra and ARPES for Bi2212 on the same sample or samples from the same batch at temperature well below T_c. After that, from ARPES experimental data, we calculate Raman spectra. Since ARPES spectra are used, the momentum dependence of self-energy is automatically involved. The calculated spectra then are compared to the experimental ones. From the obtained results, we try to understand the electronic state of high-T_c superconductivity and answer the questions. This approach is the first trial in the world.

Chapter 3

Experimental Methods

3.1 Angle-resolved photoemission spectroscopy

All high-T_c cuprate superconductors have layered structure, specially Bi2212 can be easily cleaved in high vacuum to leave a clean surface which is very suitable for ARPES measurement. Therefore, ARPES has been developed much for Bi2212 in the last two decades. Today energy resolution of 0.1 meV and resolution of angle 0.1^o can be achieved. While Raman scattering is a photon-in photon-out process, ARPES is a photon-in electron-out process. ARPES allows us to measure both energy and momentum of electrons in occupied states. Therefore, it gives information about band dispersion. In ARPES measurements a beam of monochromatic high-energy photons $h\nu$ is illuminated on the surface of a sample whose crystal orientation is known already. A three-step model can be used to understand the photoemission process [77]. Three-step model is the one with three independent steps; (i) an electron in a bulk sample is excited by absorption a photon (ii) the excited electron moves to the surface of the sample without scattering (iii) the electron overcomes the potential of work function Φ and escapes into vacuum with a kinetic energy E_{kin}. In the photoemission process, the momentum of photon is negligible in comparison to the size of BZ. Therefore, the momentum of the electron is conserved when it is excited from the initial state to the final state. However, when the excited electron moves into vacuum, its momentum in the direction perpendicular to sample surface is lost because of the work function, while the parallel component is conserved because of transition symmetry. Figure 3.1 describes the

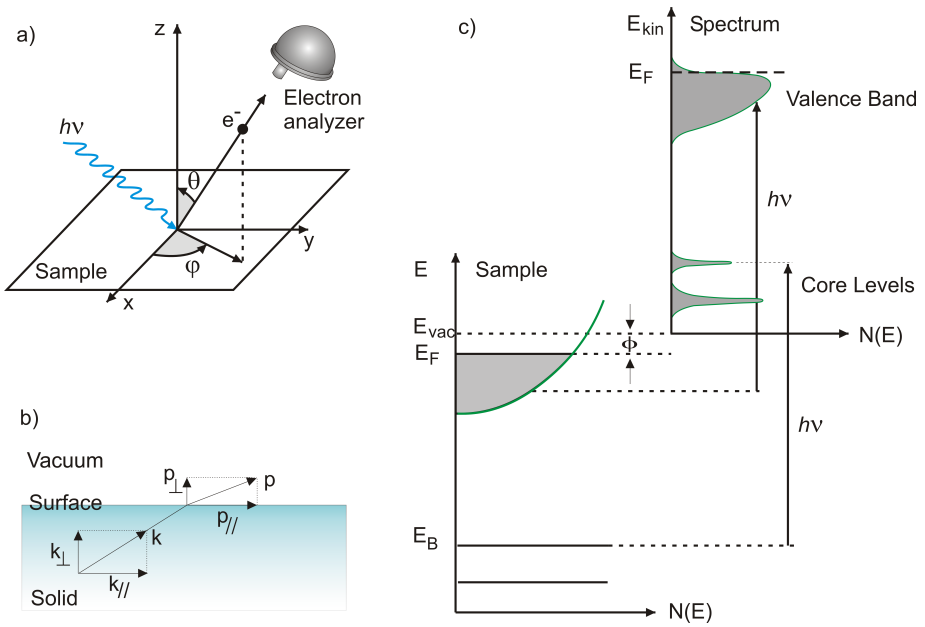

Figure 3.1: Angle-resolved photoemission spetroscopy. (a) geometry of an ARPES experiment. A beam of photons with energy $h\nu$ is irradiated on cleaved sample surface and electrons emit in a direction specified by the polar angle θ (ϑ) and the azimuthal angle φ. (b) The emission of an electron from a cuprate single crystal to vacuum. (c) Energies of the photoemission process. An electron at binding energy $\mathrm{E_B}$ absorbs energy $h\nu$, excites to vacuum state in which it overcomes the work function ϕ then emits with a kinetic energy $\mathrm{E_{kin}}$. Therefore binding energies can be determined through the kinetic energies of photoelectrons [77].

photoemission process. The equations 3.1 and 3.2 are the ones of energy conservation and momentum conservation, respectively, where E_B is binding energy, $\mathbf{p}$ is momentum of the electron in vacuum, θ is pole angle and m is the mass of electron

$$E_{kin} = h\nu - \Phi - |E_B|, \tag{3.1}$$

$$\mathbf{p}_{/\!/} = \hbar\mathbf{k}_{/\!/} = \sqrt{2mE_{kin}} \cdot \sin\theta. \tag{3.2}$$

The work function is the energy difference between E_F and vacuum energy E_{vac}, $\Phi = E_{vac} - E_F$. In practice both $\mathrm{E_F}$ and $\mathrm{E_{vac}}$ are connected to the ground hence it is convenient to write

$$E_{kin} = h\nu - |E_B|. \tag{3.3}$$

Therefore by measuring kinetic energy of the electron together with position of detector (or direction) we can determine binding energy and momentum of the

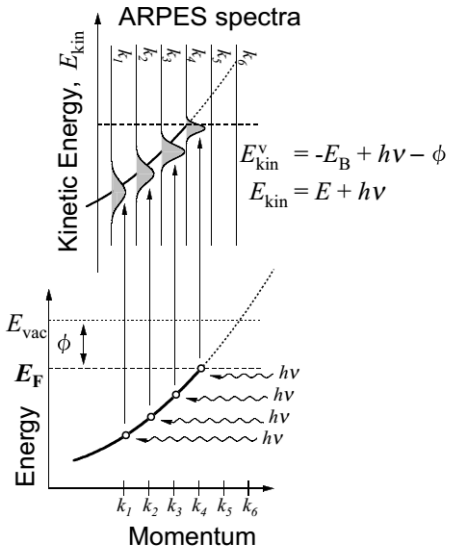

Figure 3.2: Because of monochromatic photons and the energy conservation law, band dispersions in material can be determined from ARPES spectra.

electron on the CuO_2 plane in the crystal. Figure 3.2 illustrates the principle to which the occupied band dispersion is obtained in ARPES measurements.

By collecting all electrons with different energies but have the same momentum we will get an energy distribution curve (EDC). Whereas collecting all electrons which have different momentum but the same energy we will get a momentum distribution curve (MDC). EDC shows density of state from which information about gaps will be analyzed while MDC can provide information about the Fermi surface (for example, see Ref. [112]). In practice, we measure along many cuts on BZ.

Figure 3.1 shows trajectories of photoelectrons in a hemisphere analyzer. Photoelectrons emitted from the sample surface go through electromagnetic lens and pass the entrance slit of the hemisphere analyzer. The photoelectrons with higher energy will be in a trajectory with larger radius. The photoelectrons with different wave vectors will come to different slides of a 2D charge-coupled-device (CCD) detector. This gives information about dispersion of one cut on BZ. By changing the angle between sample surface and the detector we will measure different parallel cuts and if we change the orientation of crystal we can measure cuts in different direction. ARPES is one technique to observe directly the band dispersion. While Raman probes an average density of state of a region on BZ, ARPES can probe

for each k-point of BZ.

To determine Fermi level, the sample is connected electrically to a metal like platinum or gold, then the Fermi level in the sample and the metal are the same. The photoemission process from the metal is measured and its EDC has a form of Fermi function.

In some ARPES measurements such as in the case we use Helium lamp the extreme ultraviolet Helium light with energy 21.2 eV is irradiated on the surface of the sample and can cover the area as wider as $2 \times 2\,\mathrm{mm}^2$, it may be wider than the sample size. Therefore, the surface of sample holder is covered by a carbon layer to exclude the low energy background near Fermi level. We cannot forget the role of vacuum or clean surface because ARPES measurement is extremely sensitive to state of surface of the sample, usually a vacuum as high as 10^{-11} Torr is applied.

To describe the ARPES spectra the sudden approximation is usually used, where the photoelectron absorbs photon, emits suddenly out the sample and does not interact with the left-behind crystal as well as other electrons. In this approximation the intensity of ARPES (EDC) spectrum of on a 2D single-band system can be written as [77]

$$I_{\mathbf{k},\omega} = I_0(\mathbf{k}, \nu, \mathbf{A}).A_{\mathbf{k},\omega}.f(\omega), \tag{3.4}$$

where $\mathbf{A}$ is a vector potential (of what), $A_{\mathbf{k},\omega}$ is a spectral function, $\mathbf{k} \equiv \mathbf{k}_{/\!/}$, ω is the electron energy with respect to the Fermi level, $f(\omega)$ is the Fermi function $f(\omega) = (e^{\omega/k_BT})^{-1}$ which implies ARPES probes occupied states only. The spectral

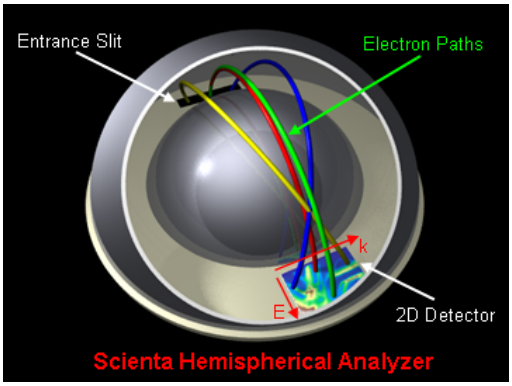

Figure 3.3: Trajectory of photoelectrons in a hemispherical analyzer [113].

function is the imaginary part of a single-particle Green function

$$A_{\mathbf{k},\omega} = \frac{-1}{\pi} G''_{\mathbf{k},\omega}. \tag{3.5}$$

I_0 is the intensity proportional to the squared one-electron matrix element M

$$I_0(\mathbf{k}, \nu, \mathbf{A}) \propto |M^{\mathbf{k}}_{f,i}|^2 \propto |\langle \phi^{\mathbf{k}}_f | \boldsymbol{\varepsilon} \cdot \mathbf{r} | \phi^{\mathbf{k}}_i \rangle|^2, \tag{3.6}$$

where $\phi^{\mathbf{k}}_i$ and $\phi^{\mathbf{k}}_f$ are the wave functions of the photoelectron in the initial state and the final state with momentum $\mathbf{k}$, respectively, $\boldsymbol{\varepsilon}$ is unit vector along the polarization direction and $\mathbf{r}$ is position of the electron. Therefore I_0 depends on the electron momentum, on the energy and the polarization of the incident photon (see more in the appendix A).

In a strong correlation system a self-energy can be introduced into the Green function. Self-energy is a complex function, $\Sigma_{\mathbf{k},\omega} = \Sigma'_{\mathbf{k},\omega} + \Sigma''_{\mathbf{k},\omega}$, which shows the renormalization of the spectral function. The imaginary part indicates the life-time and the real part shows the change in energy. The Green function with renormalization is

$$G_{\mathbf{k},\omega} = \frac{1}{\omega - \epsilon_k - \Sigma_{\mathbf{k},\omega}}, \tag{3.7}$$

and the spectral function becomes

$$A_{\mathbf{k},\omega} = -\frac{1}{\pi} \frac{\Sigma''}{[\omega - \epsilon_k - \Sigma'_{\mathbf{k},\omega}]^2 + [\Sigma''_{\mathbf{k},\omega}]^2}. \tag{3.8}$$

Determination of an exact self-energy is a difficult task. There are some studies in this field [110, 111].

ARPES figured out many properties of the cuprates such as d-wave symmetry, a pseudogap in the normal state, a kink in the nodal-line dispersion, steep dispersion in the nodal region but flat in the antinodal region [114]. When the temperature decreases through the superconducting transition temperature T_c, the coherence peak at antinodal region increases its intensity [52, 115] showing that the peak is correlated to superconductivity. However, a clear gap forms from this peak (both determined from peak to peak and from leading edge) at temperature above T_c, raising the question what origin of this peak is. Since the peak position in the antinodal region does not show clear temperature dependence (figure 3.4), this behavior is considered as an evidence for the precursor forming of Cooper pairs.

It is well known from ARPES data that Fermi surface is not full at a range of temperatures above T_c and in a wide range of doping from underdoped to overdoped [90, 116]. A Fermi arc is a gapless arc lasting from the node to a middle point in between the nodal and the antinodal direction at temperatures above T_c. Figure 3.5 shows that the other part is gapped in the normal state. The gap around the antinodal region in the normal state is a pseudogap which is in the center of debate in high T_c superconductivity. Understanding the Fermi arc is related to the pseudogap. The arc behavior is distinct from that of the normal metals where exists a continuous Fermi surface, therefore there are some studies claiming that the Fermi arc is a part of a Fermi pocket [117]. Concerning doping dependence, the Fermi arc length becomes shorter with lower doping. As discussion in Ref. [90], a measurement sensitive to Fermi surface such as d.c. resistivity should be affected by the Fermi arc, and the collapse of the Fermi arc by lowering doping should correlate to superfluid density.

Although there are many strange behaviors and differences from BCS superconductors, the fact that a gap just opens in the superconducting state and follows BCS prediction is clear in ARPES data. Figure 3.6 shows a gap opening below T_c in an optimally doped sample $T_c = 92$ K Bi2212 [52] at point C shown in the inset of this figure.

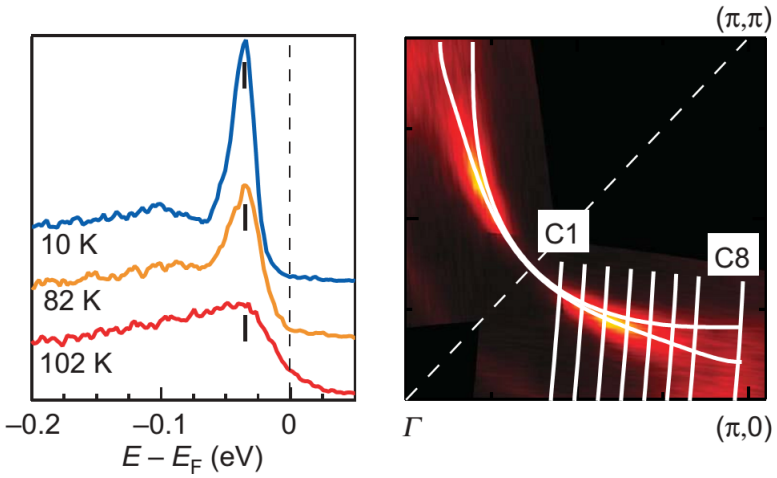

Figure 3.4: Temperature dependence of ARPES EDC spectrum of an optimally doped Bi2212 ($T_c = 92$ K) measured near k_F of the cut C8 in the antinodal region; C8 is shown in the figure on the right. The intensity of coherence peak increases with lowering temperature while the energy gap does not change. [52]

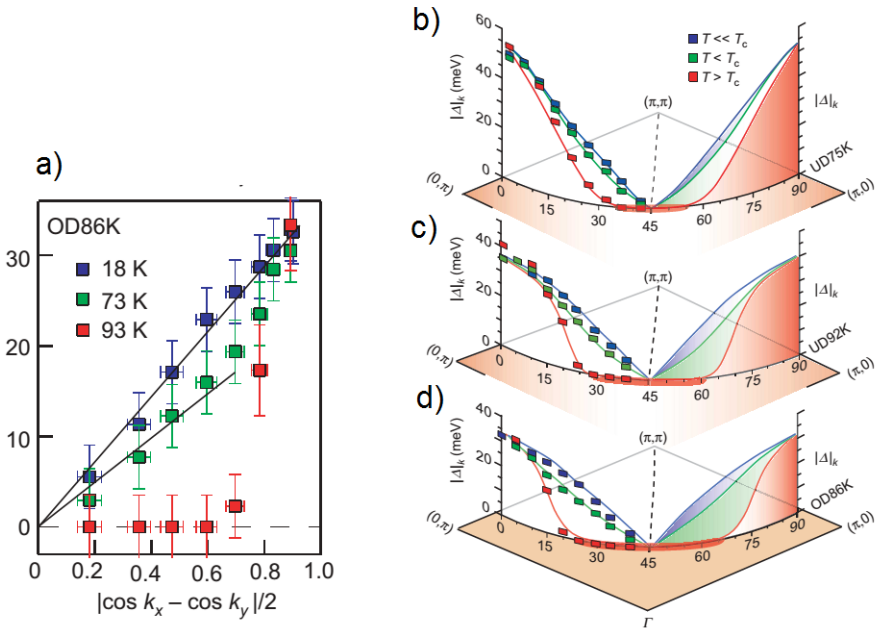

Figure 3.5: a) Temperature dependence of gap profile against the d-wave function along the Fermi surface of an overdoped Bi2212 sample ($T_c = 86$ K). The data in the normal state shows the existence of a Fermi arc around nodal point and/or a gap in antinodal region. b) Doping and temperature dependences of Fermi arc length from three samples underdoped $T_c = 75$ K, nearly optimally doped $T_c = 92$ K and overdoped $T_c = 86$ K. [52]

In Bi2212 system and especially in the overdoped side, ARPES data shows a bilayer splitting of band into an antibonding band and a bonding band [118] because of hoping between two layers in one unit cell. This splitting becomes stronger in the antinodal region.

The matrix element represents the interaction between an electromagnetic wave and electrons. It is well known that the matrix element strongly depends on photon energy and the polarization of the light, and sometimes behaves tricky. For instance, photon energy dependence of ARPES spectra for overdoped Bi2212 which show bilayer splitting was reported for $h\nu$ 18-65 eV [119]. As shown in Ref. [119], intensity for two bands shows a complicated photon energy dependence, and this behavior also shows doping dependence. This result shows that it is really hard to completely understand the effect of matrix element and hence the $A_{\mathbf{k},\omega}$.

In our ARPES measurements, we used lights from both synchrotron source and Helium lamp. The samples OP92K and UD75K were measured at the synchrotron beamline 5-4 at Standford Synchrotron Radiation Lightsource (SSRL), and the

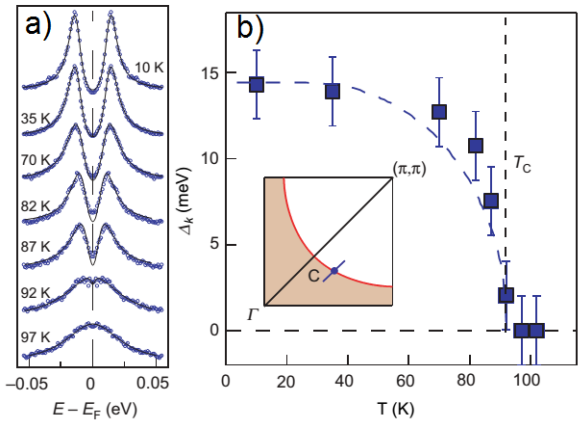

Figure 3.6: Gap follows BCS theory. a) Temperature dependence of EDC ARPES spectra at the point C shown in the inset of b) from normal state to well bellow T_c of an obtimally doped Bi2212 sample ($T_c = 92$ K). b) The gap closes just above T_c and the gap size follows the prediction of BCS theory [52].

sample OD85K was measured at Institute for Solid State Physics, Tokyo University, Japan, using HeIα line.

Although photoemission process needs photons with high energy but photons in the range of ultra violet are preferable, that is because, with lower-energy photons, momentum of the electron is conserved with the contribution from photon is ignored and the resolution of energy and momentum is better [77]. Recently people use very low energy photons (6-8 eV) to get very high resolution [120].

It was shown that in photonemission and high energy X-ray data there is a large contribution of secondary electrons making an intrinsic background in measured spectra. This is violation of sudden approximation that the primary electron loses its energy when moving to the surface by inelastic scattering and also other electrons get energy from these collisions. Usually background subtraction is ignored when people analyze just tendency of the coherence peak of spectral function. However to get more exactly about the peak position or the spectral weight, the background should be concerned.

There is one good way usually applied to subtract the background in ARPES data. That is subtraction for a phenomenological background called Shirley background [77, 121–125]. Shirley background has the form:

$$bg_{Shirley} = c \int_{\omega}^{\infty} P(\omega')d\omega', \tag{3.9}$$

where c is a coefficient, P is the primary spectral function which is from unscat-

tered electrons. The form of Shirley background indicates that the intensity of the background at certain energy (or number of electrons which have certain energy) is originated from all unscattered electrons with higher kinetic energy. The spectrum after subtracting background I or the primary scattering P will be

$$I(\omega) \equiv P(\omega) = R(\omega) - c\int_{\omega}^{\infty} P(\omega')d\omega', \tag{3.10}$$

where R is the raw measured EDC spectra. To calculate Shirley background a convolution should be applied with the initial value is zero. One advantage of Shirley background is that there is only one free parameter c.

Another way which could be used is subtracting for k-independent background. This background is actually one ARPES EDC spectrum taken at momentum area on Brillouin zone far from Fermi surface originated from roughness of the sample surface, which usually has a step-like form [112,119,120,126–128]. There are some other ways including linear background that is continuous spectrum upon which the coherence peak superimposes, and integrated background whose intensity at certain energy comes from all electrons having higher kinetics energy [129]

$$bg_{integrated} = c\int_{\omega}^{\infty} R(\omega')d\omega'. \tag{3.11}$$

In present study background subtraction for ARPES data is applied to obtain the coherence peaks to help look insight the physics of photoemission phenomenon in high-T_c cuprate.

3.2 Electronic Raman Scattering

Raman phenomenon is an inelastic scattering process of photons, which was discovered by C. V. Raman in 1928 and it is used widely in study on vibration and rotation of atoms in solids. Electronic Raman spectrum is caused by electronic density fluctuation and is the electronic continuum where phonon modes and two-magnon modes superimpose. Optical phonon modes appear at well-identified frequency in each Raman measurement geometry while broad two-magnon modes that occur in compounds with antiferromagnetic order stay at very high energy [130]. Electronic Raman scattering was not used so much in the study of conventional superconductors because these superconductors have high carrier concentration leading to a

strong screening effect and it is difficult to get ERS spectrum. However after the discovery of high-T_c cuprate superconductors in which charge carrier concentration is not so high, it was shown that ERS can be a strong tool in the study of this material system. In addition, cuprate superconductors have many atoms in their unit cells, together with their symmetric behavior of crystal structure, which allow high-T_c cuprates to hold many Raman active modes [131].

A Raman process in which the scattered light has longer wave-length, lower energy, is called Stockes process and in the inverse case of shorter wave-length we have anti-Stockes process. Figure 3.7 shows the Stockes process where an electron from initial level absorbs a photon (which usually is laser light) with energy $\hbar\omega_L$, excites to a virtual level and then emits a longer wavelength photon with energy $\hbar\omega_S$ and gets the final state. In an ERS spectrum we measure intensity of scattered light with respect to the change of wavelength (or frequency) called Raman shift. Energy and momentum conservation laws of Raman process are:

$$\begin{aligned} \hbar\omega_R &= \hbar\omega_L - \hbar\omega_S, \\ \mathbf{k}_R &= \mathbf{k}_L - \mathbf{k}_S - \mathbf{Q}, \end{aligned}$$

where $\mathbf{Q}$ is a vector belonging to the reciprocal lattice. Figure 3.7 presents Stockes process in electronic Raman scattering.

In conventional superconductors the Raman excitations which break Cooper pairs into pairs of quasiparticles with momenta **k** and **-k** result in a threshold in scattering spectra at 2Δ [82]. ERS is one of the first tools showing that there is

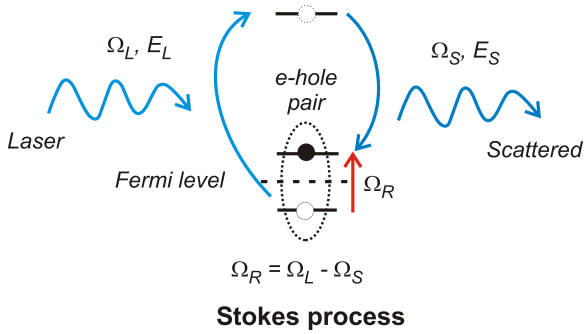

Figure 3.7: Electronic Raman scattering - Stockes process. A laser beam with a monochromatic wavelength Ω_L is irradiated on surface of a crystal and scattered to wavelength Ω_S. The difference between the laser and scattered wavelengths is called the Raman shift, Ω_R, which is corresponding to the energy of an electronhole pair excitation around the Fermi level [100].

a gap in high-T_c cuprates however people also soon realized that with different geometries of measurement, different gaps on BZ were observed. In the present study, we concentrate on B_{1g} and B_{2g} electronic Raman scattering. For phonon Raman active one can see in appendix B. Figure 3.8 describes B_{1g} and B_{2g} geometries which show how polarization vectors of incident (in-coming) light and scattered (out-going) light orient to the crystal. With B_{1g} geometry polarization of incident light and scattered light are 45° to the Cu-O bonds while in B_{2g} they are parallel to the Cu-O bonds. Laue measurements are performed in order to determine the orientation of crystal axes. Ideally both incident light and scattered light are perpendicular to the CuO_2 plane, however in practical it is quasi-back scattering with incident light is about $30 - 45°$ to the c axis this is to avoid the reflected light coming into the CCD detector.

For a certain sample, different spectroscopic techniques have different sampling depths. For high-T_c cuprates, while ARPES is restricted to a depth of few layers from the measured surfaces (5-10 Å [58, 131]), Raman (and also IR) measures a medium depth about several hundreds to one thousand Å [58, 60]. Comparing to the c lattice constant of Bi2212 (30.8 Å) Raman measurement can be considered as a bulk probe. However Raman is still a surface-sensitive measurement therefore clean surface is preferable and hence a high vacuum is better. Laser light is focused on sample surface with a spot size about 50-100 μm in diameter.

Figure 3.9 shows the typical scheme of a Raman measurement. Where a monochromatic laser light (in our case $Ar^+ - Kr^+$ laser) goes to the sample through an optical path including some devices such as gratings, pinholes, lenses, polarizers and mirrors. Some part of in-coming laser is reflected and some part is scattered,

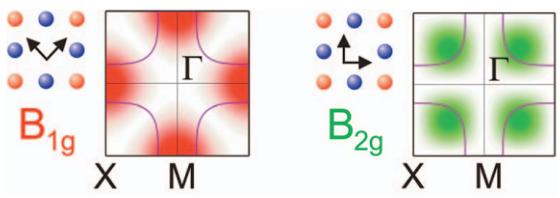

Figure 3.8: The polarization orientations of the incident laser and scattered lights with respect to the Cu-O bonds of a D_{4h} crystal in B_{1g} and B_{2g} geometries are denoted by vectors. B_{1g} and B_{2g} geometries probe respectively the antinodal region and nodal region in BZ. The solid lines denote Fermi surface of a optimally doped cuprate [130].

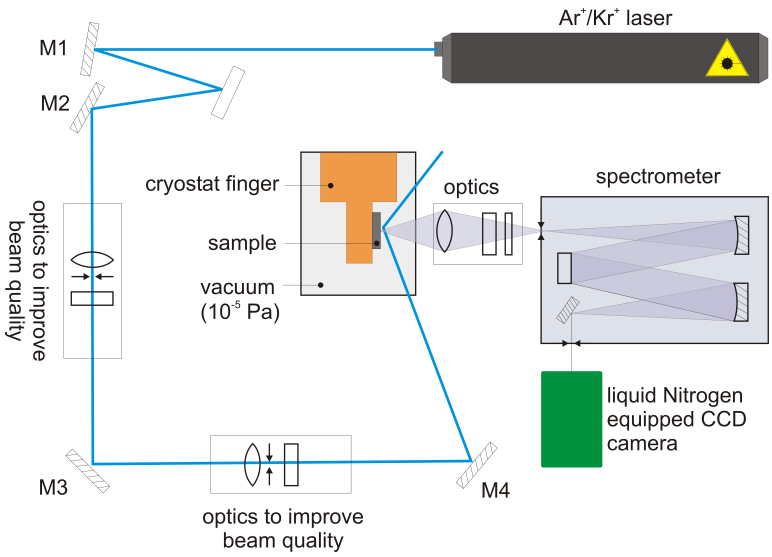

Figure 3.9: Scheme of Raman system. A monochromatic laser light is chosen by grating and pass an optical path to improve the beam quality before irradiate on sample surface. The scattered lights are collected by optical lens and come into the triple-gratings spectrometer and collected by the charge-coupled device detector.

the scattered light goes through a lens and a polarizer then comes into the spectrometer and finally comes to the detector.

In the present study, the Raman system Jobin-Yvon T64000 coupled to a liquid-nitrogen-cooled CCD detector was used. The spectrometer is a triple-grating one which can operate in two modes, subtractive and additive modes. Gratings have density of 1800 gr/mm. In subtractive mode, the spectrometer can measure in a wide range of energy. It also can reject stray lights well and therefore collect Raman signal at very low energy, 5 cm^{-1}, and actually the low-energy limit we measured (from 50 to 150 cm^{-1}) is much higher than this limit. The resolution of energy is 0.3 cm^{-1} in this mode. In additive mode a narrow range of energy with a ultrahigh resolution (0.1 cm^{-1}) can be achieved and this mode is usually used to study the band splitting.

Figure 3.10 shows the optical diagram and figure 3.11 presents the optical path of the subtractive mode. A polychromatic radiation enters the pre-monochromator through the entrance slit S1 and is dispersed by grating G1. The exit slit of the first stage which is the entrance slit of the second stage, the intermediate Si1/2, selects a bandpass between λ_1 and λ_2. The grating G2 in the second stage recombines all the dispersed radiations on the intermediate slit Si2/3 which is the entrance slit of

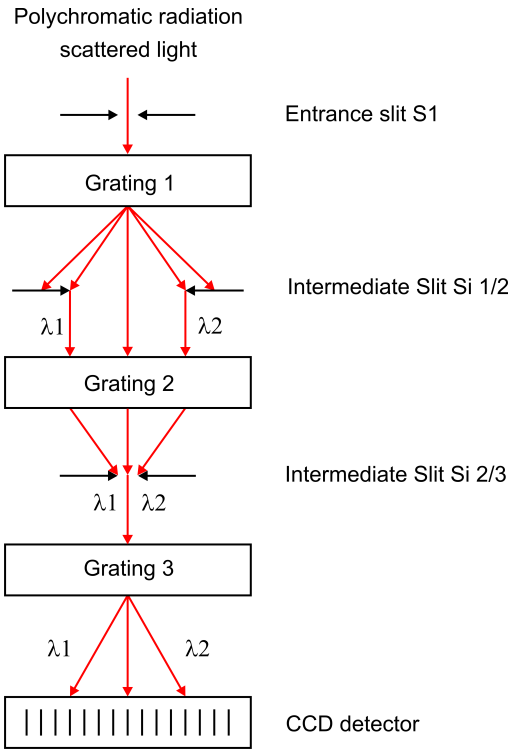

Figure 3.10: Optical diagram of the subtractive mode.

the spectro-monochromator giving a polychromatic radiation, but limited to only the spectral range between λ_1 and λ_2. The grating G3 disperses the poly radiation on the CCD detector. For the configuration of the additive mode, one can see in appendix C.

Most electronic Raman scattering studies use incident lasers which have photon energy in the range 2.0-2.5 eV. This range of energy is the charge-transfer energy gap of a antiferromagnetic insulator, the parent phase of cuprates [132]. With a $Ar^+ - Kr^+$ laser generator, different wavelengths of visible laser light can be used, 458, 514.527 and 632.8 nm. With different photon energies it was shown that in Bi2212 some phonons will be enhanced or wiped out [60, 96, 133, 134]. This behavior also was observed in Hg1201 [100, 135, 136] or in Tl2201 [137]. In detail, with the blue light laser 458 nm (2.72 eV) the phonon peaks at 290 and 110 cm^{-1} in B_{1g} spectrum of an optimally doped Bi2212 sample ($T_c = 91$ K) are clear and strong, while with the red laser 633 nm (1.95 eV), intensity of these peaks are very small [133]. Using ultraviolet lights can enhance phonon peaks and overcome the electronic response. Using red wavelengths can also enhance

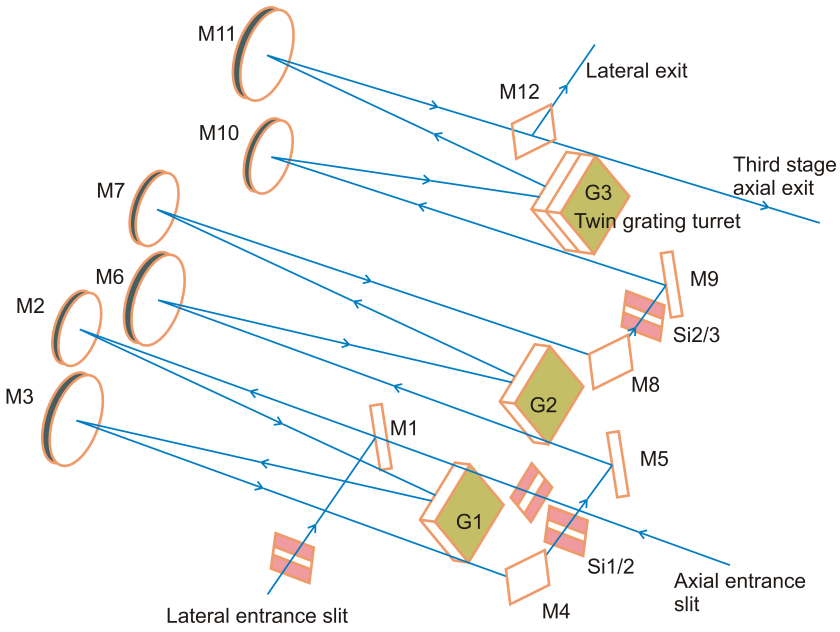

Figure 3.11: Optical path of the subtractive mode inside the spectrometer. In the subtractive mode, the spectrometer can reject stray light well then allow to collect Raman signal at very low energy. M notation denotes a mirror, G is for grating and S is for slit.

intensity of electronic spectra but do not change the electronic peak position as the case of Hg1201 [135, 136, 138] and Bi2212 [139], this is also observed in the electron-doped cuprate $Nd_{2-x}Ce_xCuO_4$ [140]. The different excitation lines do not affect the symmetry of the Raman vertex but can change its intensity [138]. These properties can help to analyze electronic Raman data easier when using red laser. For Bi2212 people usually use green light because there are some phonon peaks but their intensity are not too strong to cover features of the electronic response. Well identified phonon peaks such as the ones at 110, 290 and 590 cm^{-1} in B_{1g}, 450 cm^{-1} in B_{2g} can be used as references for measurements. It was also mentioned that green light shows higher efficiency than the others to probe the nodal B_{2g} spectrum. In our Raman measurement, laser wavelength of 514.527 nm (2.4097 eV) was used.

To investigate the electronic structure of cuprates, Raman measurements have been performed [141–144], recently A. Sacuto's group did a detailed investment for Bi2212 superconductors [45]. The behaviors can be briefly summarized as follow. For pairing symmetry, the ω-cubic behavior in B_{1g} and ω-linear in B_{2g} spectra which are expected from *d*-wave symmetry are observed.

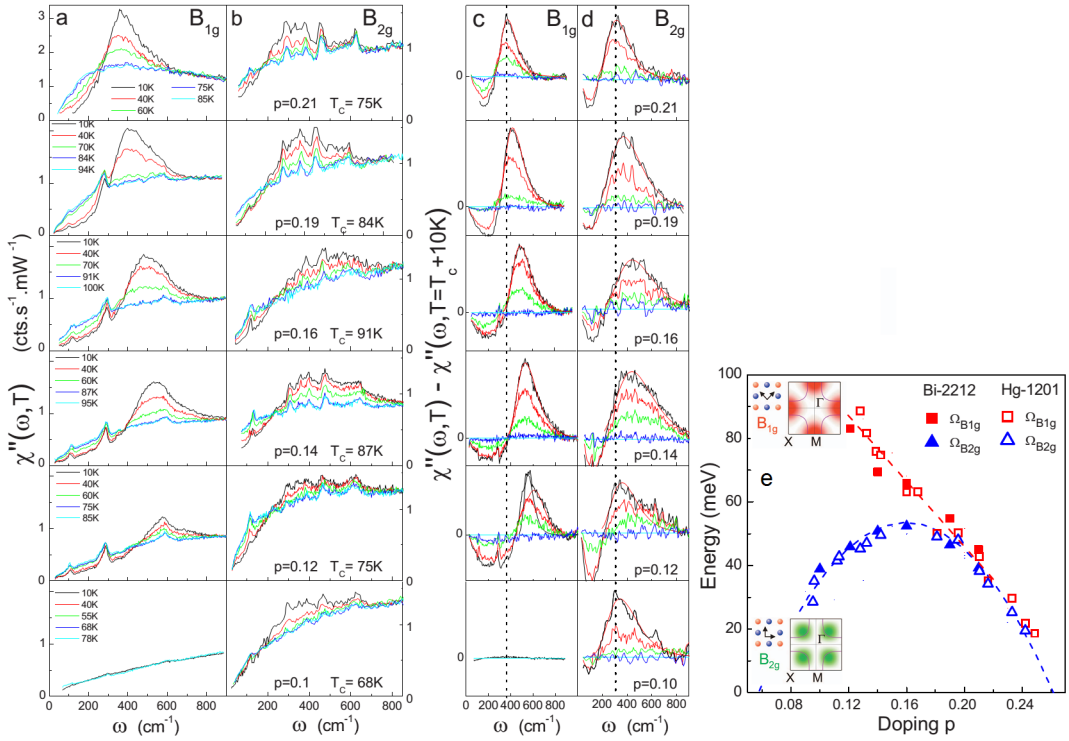

Figure 3.12: Two energy scale in Raman spectra. a) and b) B_{1g} and B_{2g} Raman spectra, respectively, of Bi2212 at different temperatures from well below T_c to 10 K above T_c and with different doping from underdoped to overdoped. c) and d) B_{1g} and B_{2g} Raman spectra subtracted from the one measured at 10 K above T_c. The dashed lines are plotted to guide eyes to the change of peak energies. e) Summary of B_{1g} and B_{2g} peak energies with respect to doping, data of Hg2201 is included. [45].

For the doping dependence, at the lowest temperature (10 K) well below T_c, the B_{1g} peak increases energy monotonically when doping decreases, while B_{2g} peak energy increases when carrier doping changes from overdoped side to optimally doped side and then decreases when doping moves to underdoped side. These behaviors are consistent with the previous reports in Bi2212 as well as other cuprates that the B_{2g} peak energy traces the doping dependence of T_c while the B_{1g} does not, which show two energy scales in the cuprates. It is clear that although energy of the B_{1g} peak increases with lowering doping its intensity decreases. For doping below 0.1, the B_{1g} peak disappears even in superconducting state while the B_{2g} peak still remains. With increasing the doping level, these peak energies merge.

For temperature dependence, in this data both B_{1g} and B_{2g} peaks disappear just above T_c, and in superconducting state when temperature decreases both these

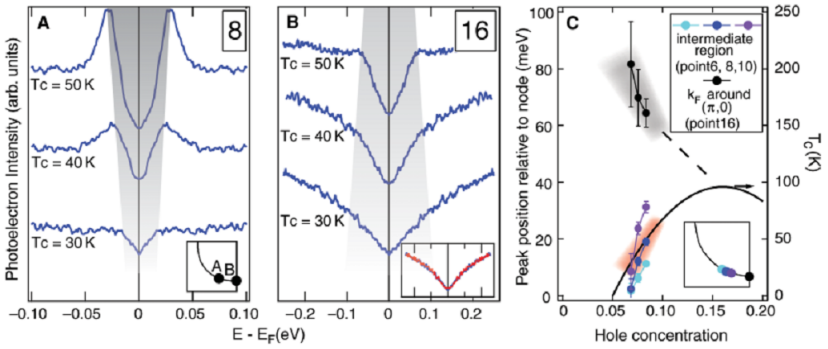

Figure 3.13: Two energy scales ARPES data. a) and b) Doping dependence of symmetrized EDC spectra of Bi2212 at point A (or point 8) and B (or point 16) on Fermi surface shown in the inset of a), measured at temperature 10 K in superconducting state. The shaded area guides eyes for two energy scales. (The inset in (b) shows the EDCs at point B at temperature 50 K (in normal state) and 10 K (in superconducting state) of the sample $T_c = 30$ K). c) Doping dependence of peak energy from EDCs at different points on Fermi surface, which are shown in the inset of c). The solid line is the empirical curve of doping dependence of T_c, $T_c = 96[1 - 82.6(p - 0.16)^2]$ [51].

peaks increase their intensity. This behavior is also confirmed from temperature dependence of spectral weight and supports that these B_{1g} and B_{2g} peaks are coherent superconducting peaks. However all of these behaviors raise questions that what the B_{1g} peak is, and/or which energy scale of those is the energy of pairing. N. Munnikes et al. claimed that B_{1g} neither relates to superconductivity or pseudogap [145].

For each doping level B_{1g} and B_{2g} Raman peak energies show weak temperature dependence as one can see from figure 3.12 for Bi2212 or from data of Hg1201 [98, 100, 146] in which only heavily overdoped samples follow BCS prediction.

Figure 3.12 presents the Raman data of Bi2212 with two energy scales in B_{1g} and B_{2g} obtained by A. Sacuto group. ARPES seemingly shares with ERS on the existence of two-gap feature where ARPES also observed two energy gaps with distinct behaviors as shown in the figure 3.13 [51]. It raises a question that whether we need two gaps to get high-T_c superconductivity or not as discussed by S. Hüfner [147]. Here we want to emphasize that the electronic Raman data of Bi2212 of A. Sacuto group is the one we used the most to refer to.

Chapter 4

Experimental results

4.1 Bi2212 single crystal growth

To grow Bi2212 single crystal, people usually use the traveling solvent floating zone (TSFZ) method under oxygen or air flow [56, 57, 148]. Self-flux method, the KCl flux method and the vertical Bridgman method are other approaches could be used to grow Bi2212. In TSFZ method we do not use any crucible. Therefore, it reduces contamination. In our study, TSFZ method was used to grow Bi2212 single crystals. Figure 4.1 shows the principle of TSFZ method. Infrared light is emitted from halogen lamps and focused by four mirrors to the connection point between the feeding rod and the seeding crystal. The temperature can be elevated above the melting point of Bi2212 to make a molten zone. Four mirrors move up with a very low speed (0.2 mm/hour) during growth process while the seeding rod and the feeding rod rotate in inverse directions (10 rounds/min) with the aim of making a uniform thermal field in all directions in the molten zone. A gas flow of the air or oxygen was used to supply oxygen for chemical reaction. The as grown samples are usually in overdoped side or nearly optimaly doped with T_c around 90 K.

The sample preparation for Bi2212 single crystals is presented in the figure 4.2 and described as follow. Oxide powders Bi_2O_3, $SrCO_3$, $CaCO_3$ and CuO with a purity 99.99% were used, balanced with the ratio of the nominal formula $Bi_{2.1}Sr_{1.9}CaCu_2O_{8+\delta}$, ground and mixed together few times alternately with heating at 800 °C in 24 hours for two times. The chemical reaction in solid phase

is

$$Bi_2O_3 + 2SrCO_3 + CaCO_3 + 2CuO + O_2 \longrightarrow Bi_{2.1}Sr_{1.9}CaCu_2O_{8+\delta} + CO_2. \quad (4.1)$$

The powder was pressed by a hydrostatic compressor to make a rod with a length of $\sim$ 10 cm, a diameter of 5 mm and followed by heating at 850 °C in 48 hours. Growth crystal was performed two times, the first growth is a rapid scan with speed 20 mm/hour and the second growth is the one with a very low speed 0.2 mm/hour. The role of the rapid scan is to make a uniform rod for the second scan as well as partly pre-reaction. The obtained crystal is cut into many small pieces and then annealed for expected doping levels. Figure 4.3 shows a piece of Bi2212 single crystals which were grown by us and the magnetic susceptibility of the as grown sample. Figure 4.4 shows a Laue image of Bi2212 sample. Because of the modulation, there is a dot-line in ΓY direction in Laue image.

Making high quality crystals with a big size is the first requirement in the study of high-T_c cuprates and by time people were successful in this issue [57,149]. Whereas it is very difficult to synthesize stoichiometric Bi2212, J. S. Wen et al. has shown that a starting composition of $Bi_{2.1}Sr_{1.9}Ca_{1.0}Cu_{2.0}O_{8.0}$ combining with

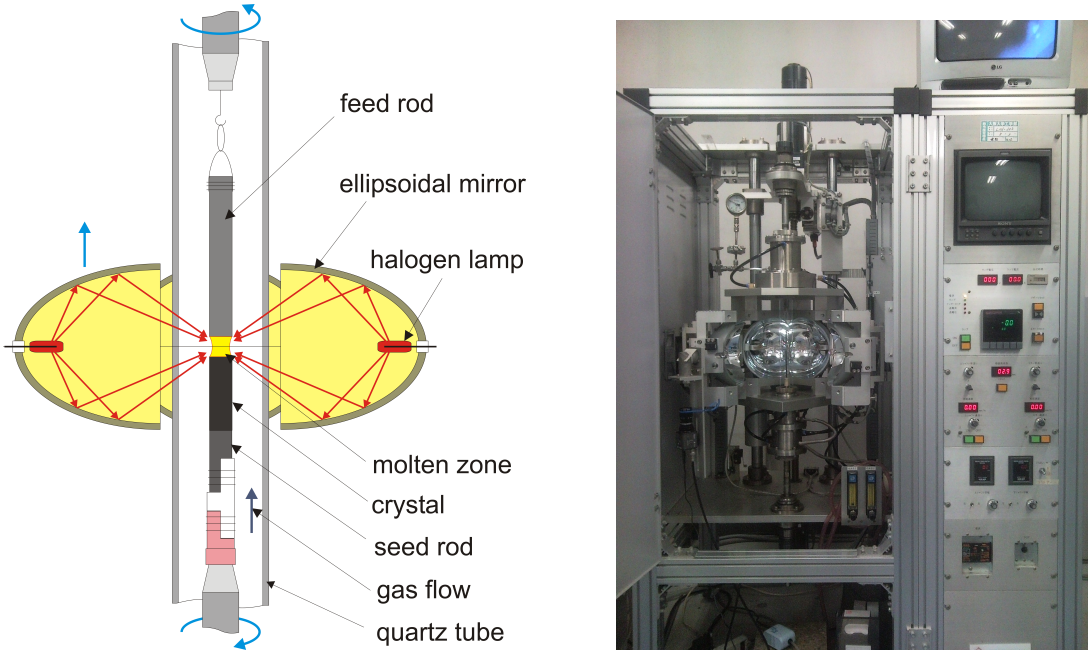

Figure 4.1: Illustration of operation of a floating zone method (left) and a photo of a four-ellipsoidal-mirror floating zone system at S. TAJIMA group, OSAKA University (right).

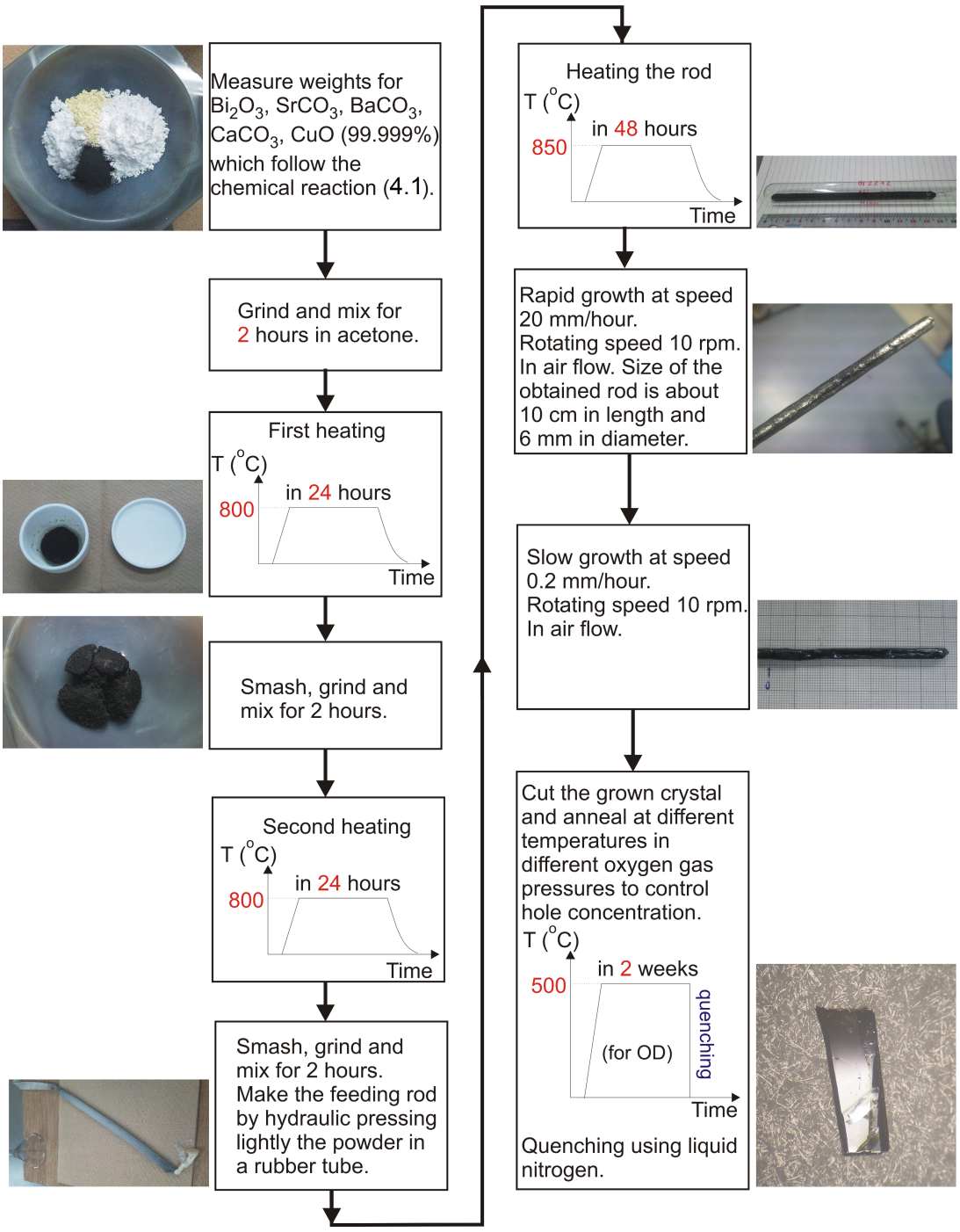

Figure 4.2: Sample preparation process for $Bi_2Sr_2CaCu_2O_8$ single crystals grown using TSFZ method.

a growth speed lower than 0.25 mm/h are helpful to make a large Bi2212 single crystal with $T_c = 91$ K and $\Delta T_c(10-90\%) = 2$ K where a smooth planar interface between solid and liquid phases is maintained in the growth process. By Pb substi-

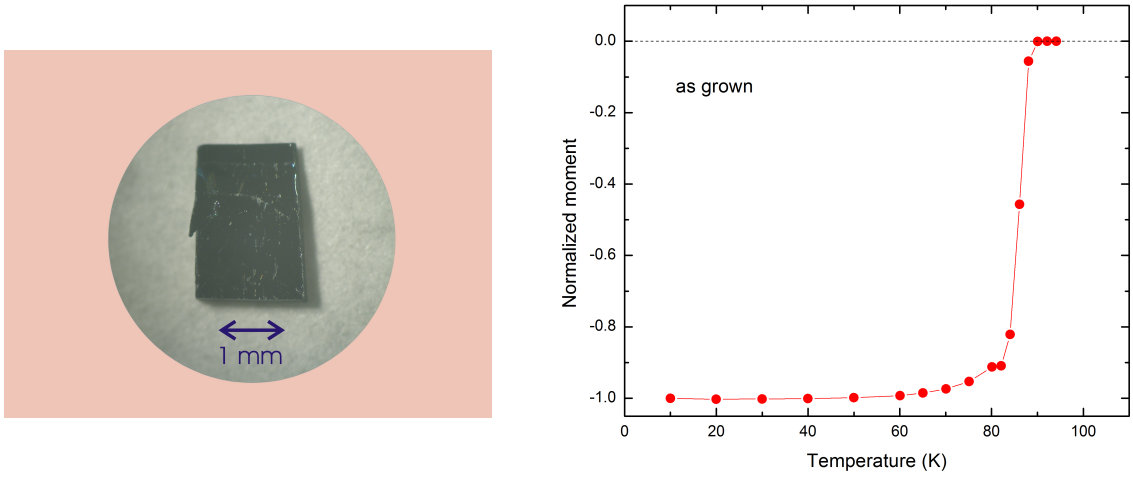

Figure 4.3: A piece of Bi2212 single crystals and the susceptibility of an as grown single crystal.

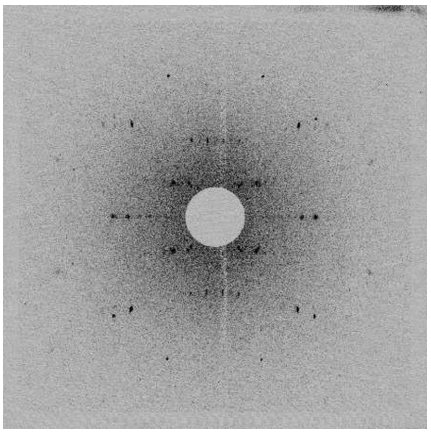

Figure 4.4: A Laue image of an as grown Bi2212 single crystal with the incident X-ray along the c axis. It shows tetragonal structure D_{4h} together with modulation along b-axis.

tution for Bi the incommensurate modulation in Bi2212 can be removed [150–152]. To go further from optimally doped region to underdoped and overdoped regions, the single crystal need to be doped less or more holes. There are two approaches to dope holes in Bi cuprate superconductors, one method is ionic substitution and the other one is modifying the oxygen stoichiometry. Trivalent cations such as Y^{3+} are usually used to substitute for divalent Ca^{2+} to obtain heavily underdoped samples. It was also shown that with Y substitution for Ca, disorder at Sr sites can be min-

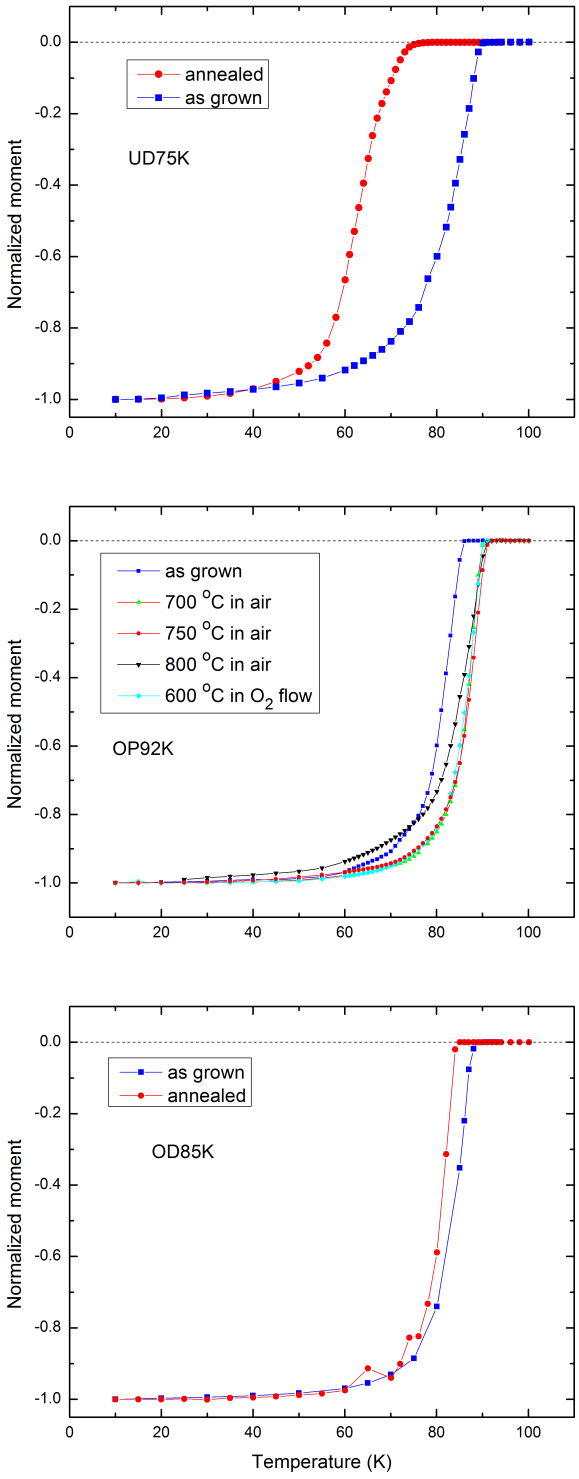

Figure 4.5: Annealing Bi2212 in different conditions to get different hole concentration. Upper panel UD75K in vacuum at 550 °C, middle panel OP92K in air at 700-750 °C and the lower panel OD85K in air flow at 500 °C.

imized leading to a high T_c value of 96 K [153]. Modifying oxygen contents is an easier way in which excess oxygens are doped into BiO layers however for doping levels higher than 0.23, oxygens can diffuse out even at room temperature [130].

In the present study, to control hole carriers, samples were annealed in different conditions such as in the air, in O_2 or vacuum, at different temperatures and in different periods of time (4 days, 7 days, 10 days, 2 weeks). There are some studies in Bi2212 annealing to get a sharp transition [148, 153–155]. The figure 4.5 shows the results of annealing in comparison with as grown samples for underdoped samples with $T_c = 75$ K, optimally doped samples with $T_c = 90 - 92$ K, and overdoped samples with $T_c = 85$ K. The procedure for underdoped sample is from the supplement of Ref. [52], which is annealing in a quartz ampul in vacuum $< 10^{-4}$ Torr at temperature 550 °C. It is difficult to get a sharp transition in underdoped side for Bi2212 because the structure could become unstable. For optimally doped samples, T_c^{max} can be obtained with temperatures $700 - 750$ °C. With a higher temperature 800 °C, T_c increases slightly but transition is broader, a good transition is recovered by annealing in oxygen flow at 600 °C. This means that there are various ways to get optimally doped samples. For the overdoped region, samples were annealed in the air at 500 °C. This is a quite good way because T_c is the same for all annealed samples.

When samples are cooled down from annealing temperatures to room temperature, if this process is slow, oxygens can diffuse in or out leading to changes in oxygen content as well as the homogeneity of oxygen in these samples resulting a broader superconducting transition. To avoid this effect, samples must be quenched by dropping them on a copper plate or into liquid N_2, the period of time samples are in the air before quenching is in 10 s. One reason for the wide transition in the underdoped sample is that the sample in a quartz ampul cannot be cooled down rapidly enough for quenching process.

4.2 ARPES measurements

The ARPES measurements for the samples OP92K and UD75K were taken at Stanford Synchrotron Radiation Lightsource beamline 5-4 using 22.7 eV photons and an energy resolution of 5 meV and the angular resolution is 0.1^o and with polarizations along Cu-O directions. ARPES data of these samples was reported

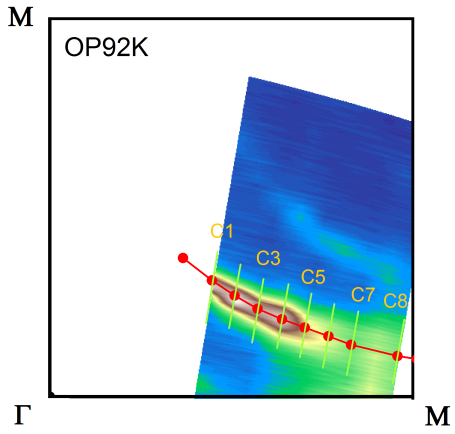

Figure 4.6: The Fermi surface mapping image of the sample OP92K. The green lines are the cuts along which energy distribution curves were obtained. The red dotted curve is the k-points on the Fermi surface, the k_F point at the node is added to see full Fermi surface.

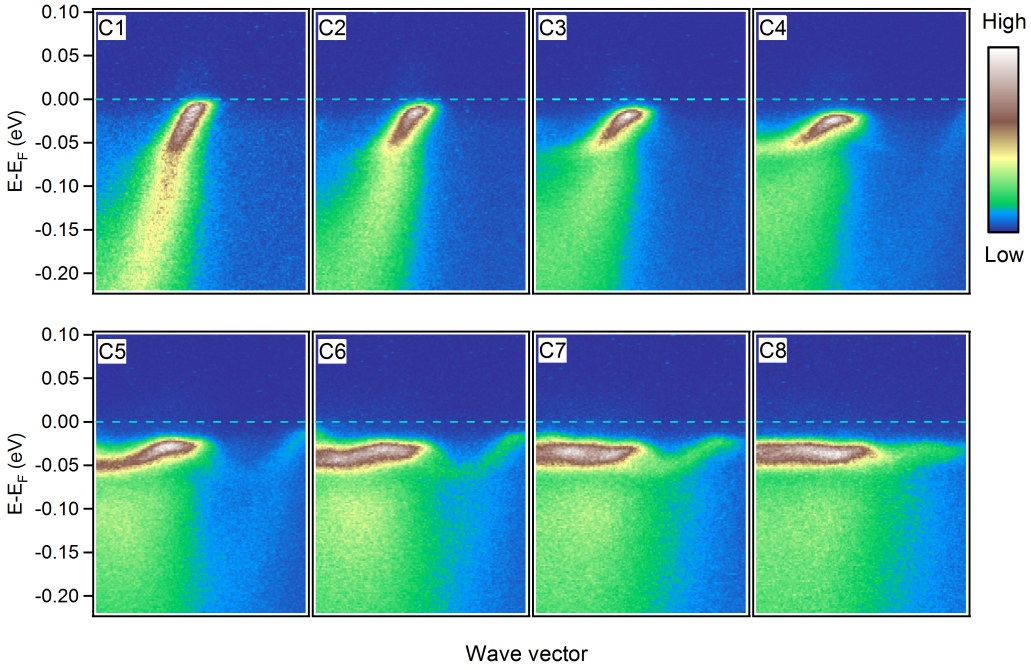

Figure 4.7: Momentum dependence of the low energy excitations in the nearly optimally doped sample Bi2212 OP92K, measured at 10 K. The dash horizontal line is the Fermi level. [52]

in Ref. [52,107] already. The image of Fermi surface of the sample OP92K is shown in figure 4.6 where the yellow lines are cuts in the direction from $(\pi, 0)$ to (π, π) along which energy distribution curves were obtained. The red dotted curve is the

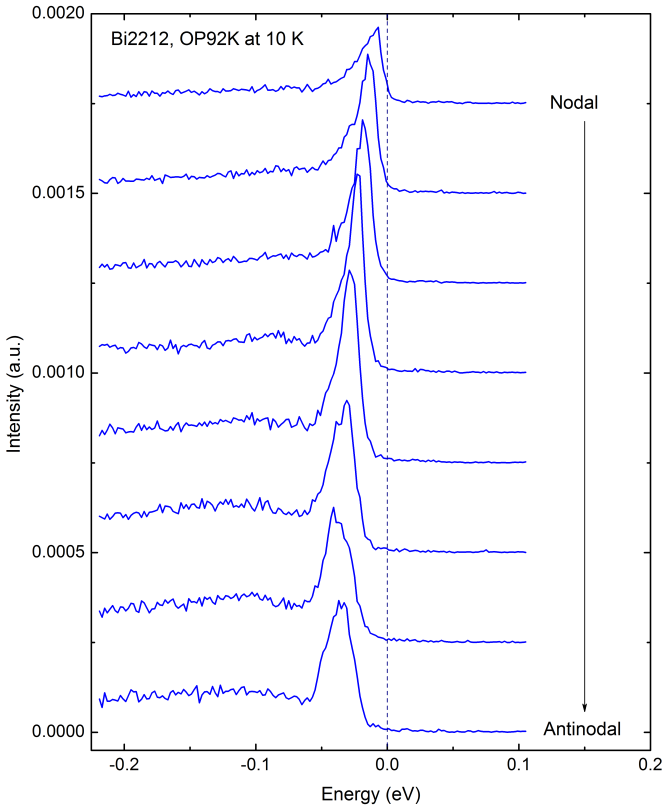

Figure 4.8: ARPES EDC spectra of the sample OP92K along the Fermi surface at different temperatures. Spectra were offset in the vertical axis.

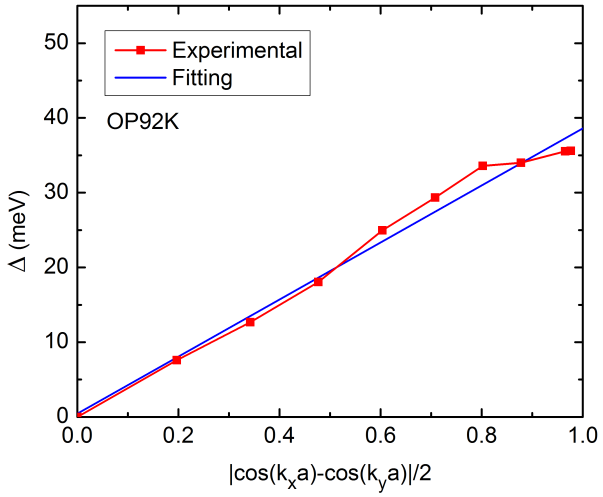

Figure 4.9: The gap profile of the sample OP92K along the Fermi surface against the *d*-wave function.

k-points on the Fermi surface k_F.

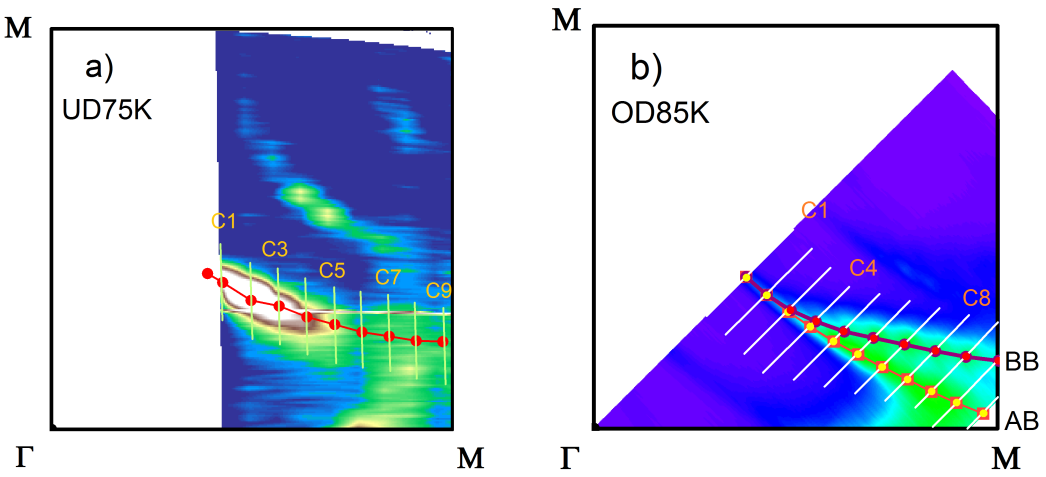

Figure 4.10: Fermi surface mapping images of the sample UD75K a) and OD85K b). The green lines are cuts along which EDC spectra were obtained. The red curves are k-points on Fermi surfaces. In the sample OD85K there is a bilayer splitting of band structure.

Figure 4.7 shows band dispersion of the sample OP92K at well below T_c(T = 10 K). One can see that the dispersion at the node is steep whereas in the antinodal region it is flat. In figure 4.8, the EDC spectra along the Fermi surface at k_F are plotted. It is clear that the superconducting gap is getting larger from the node to the antinode. From analysis of peak position, one can get the gap profile along Fermi surface as shown in figure 4.9. The gap profile for the sample OP92K along Fermi surface at 10 K fits well to d-wave gap that is linear line with respect to d-wave function $|\cos(k_x a) - \cos(k_y a)|/2$.

The similar data of the sample UD75K is shown in the figure 4.10 a) for Fermi surface mapping and in the figure 4.11 for band dispersion at 10 K along cuts in the direction from $(\pi, 0)$ to (π, π) shown in figure 4.10. The gap profile along Fermi surface at 10 K deviates from d-wave behavior around the antinodal region as one can see in figure 4.13, which can be caused by the pseudogap.

The sample OD85K was measured at the laboratory of Prof. S. SHIN, Institute for Solid State Physics, Tokyo University using Helium lamp light with photon energy of 21.2 eV without polarization. Energy resolution is 10 meV and angular resolution 0.1^o. The cuts are parallel to the nodal line, from $(0, 0)$ to (π, π). We observed a band splitting from two CuO_2 layers into a antibonding band (AB) and a bonding band (BB), that is usually observed by synchrotron photons but not by

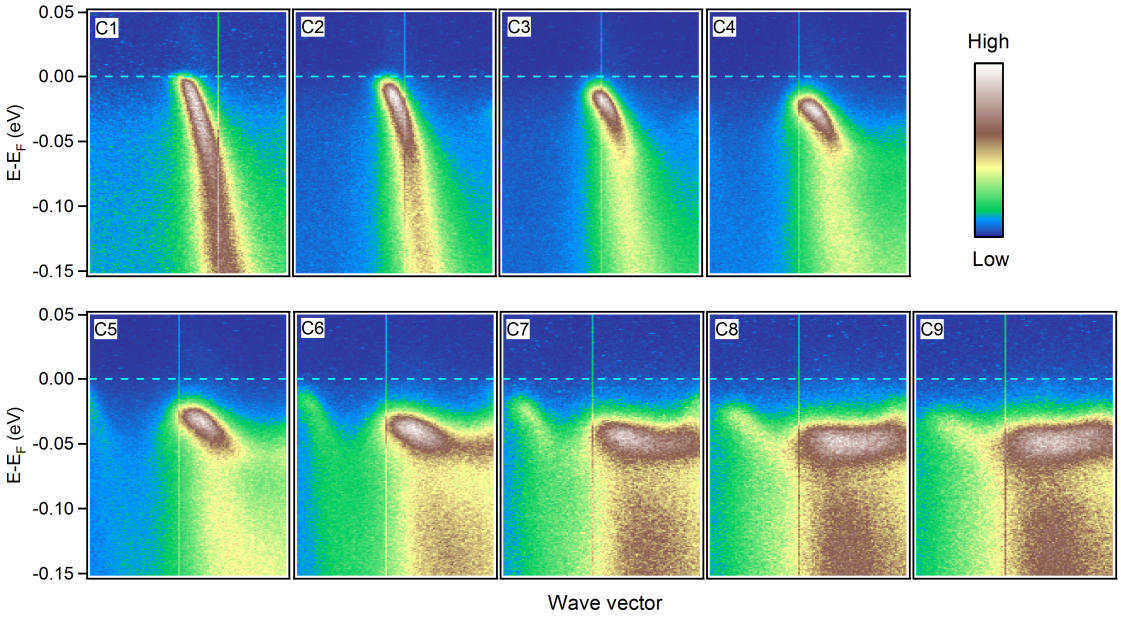

Figure 4.11: Band dispersion at 10 K along cuts shown in the figure 4.10 of the sample UD75K.

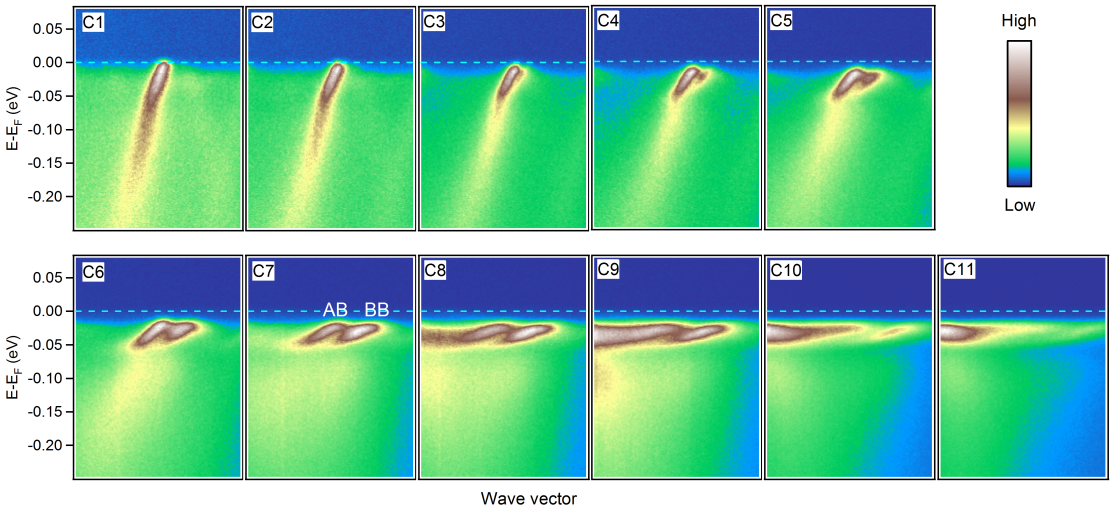

Figure 4.12: Band dispersion at 10 K along cuts shown in the figure 4.10 of the sample OD85K. From cut C4 the bilayer splitting starts to be clear.

helium light. Figure 4.10 b) and 4.12 show Fermi surface mapping image and the band dispersion at 10 K of the sample OD85K, respectively.

Figure 4.13 summarizes the doping dependences of the Fermi surfaces and the gap profiles of the three samples UD75K, OP92K and OD85K. We observed less

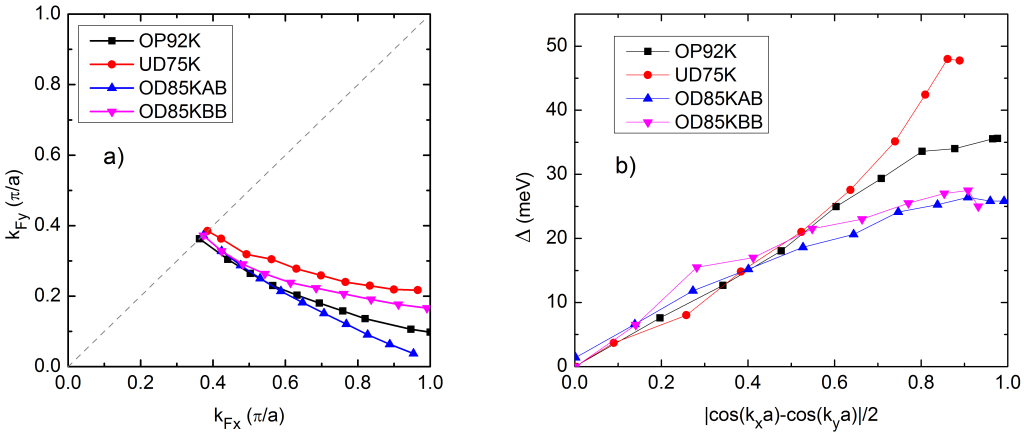

Figure 4.13: Experimental Fermi surfaces a) and gap profiles b) obtained from ARPES data of the three samples underdoped ($T_c = 75$ K), nearly optimally doped ($T_c = 92$ K) and overdoped ($T_c = 85$ K) Bi2212. The notations AB and BB of the sample OD85K are corresponding to antibonding and bonding bands.

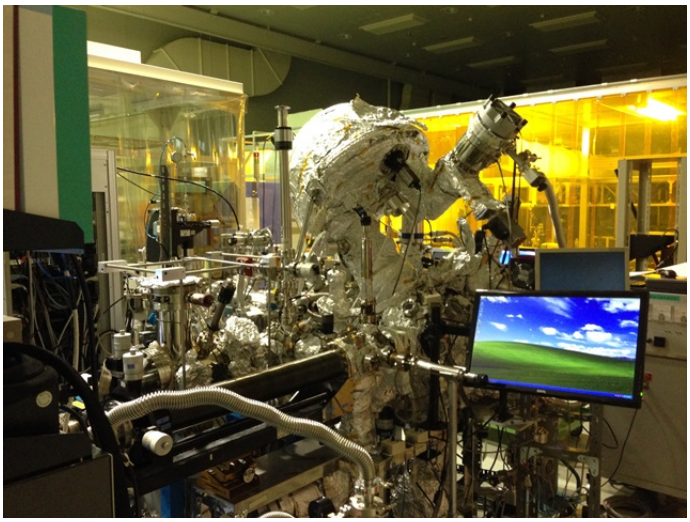

Figure 4.14: The ARPES system at S. SHIN group, Institute for Solid State Physics, Tokyo University.

doping dependence of gap slope around the nodal region in these dopings, which is consistent to recent ARPES report [107].

Figure 4.14 is a photo of the ARPES system at S. SHIN group, Tokyo University.

4.3 ERS measurements

A photo of our Raman system, a triple-grating T64000, is shown in figure 4.15. A sample is mounted on a copper sample holder by using silver paste, cleaved in the air and then the sample holder is connected to the cryostat finger by screws. The sample chamber is evacuated to as low pressure as 5×10^{-5} Pa by a Turbo pump. To measure at low temperatures a Helium gas refrigerator cryostat was used. With this cryostat we can save cost of He, however the sample vibrates during measuring. Temperature can be lowered down as low as 5 K.

ERS measurements were performed in B_{1g} and B_{2g} geometries on the samples from the same batch (OP92K and UD75K) or on the same sample (OD85K) with ARPES measurements. ERS spectra were probed at different temperatures with a triple grating T64000 spectrometer with a liquid-nitrogen cooled CCD detector using ArKr laser line 514.527 nm. The laser beam was focused into a spot of 100 μm in diameter and the laser power was kept $\sim$5 mW to avoid overheating. A closed cycle cryostat was used with temperature stabilization better than 1 K. The B_{1g} geometry is obtained when crossed polarizations for incident and scatterd light are 45^o from the Cu-O bond directions while B_{2g} polarizations are along them. In these geometries the antinodal and the nodal regions corresponding to the principal axes and the diagonal of the Brillouin zone are probed, respectively. All the Raman

Figure 4.15: The Raman system triple-grating T64000 at S. TAJIMA group in OSAKA University.

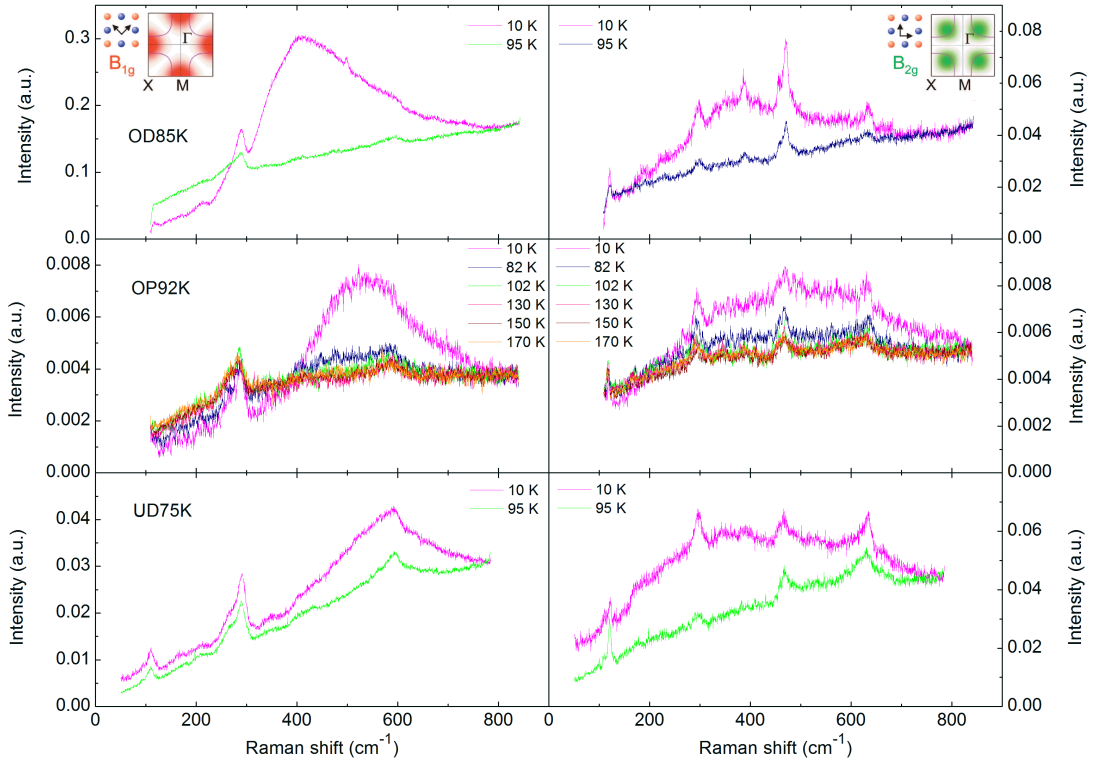

Figure 4.16: Doping and temperature dependences of experimental electronic Raman B_{1g} and B_{2g} spectra of Bi2212.

spectra have been corrected for the instrumental spectral response and the Bose factor.

Figure 4.16 summarizes all ERS results on doping and temperature dependences of the three samples UD75K, OP92K and OD85K. Their behaviors are consistent with other previous reports in two energy scales and on tendency of intensity of B_{1g} peak as well as B_{2g} peak. For the spectra in the normal state in the optimally doped sample all spectra above T_c coincide and we don't clearly see any pseudogap. For the overdoped and underdoped samples, there are small differences that are easily to conclude that their origin is from pseudogap.

The differences between spectra in the normal state and the superconducting state are clearly seen in figure 4.16. To see more clearly the superconducting-induced behavior, the Raman spectra at the lowest temperature was subtracted from the one measured just above T_c (10 K above T_c) and presented in figure 4.17.

In this chapter, details on crystal growth for Bi2212 single crystals by traveling solvent floating zone method were presented. Different doping levels were

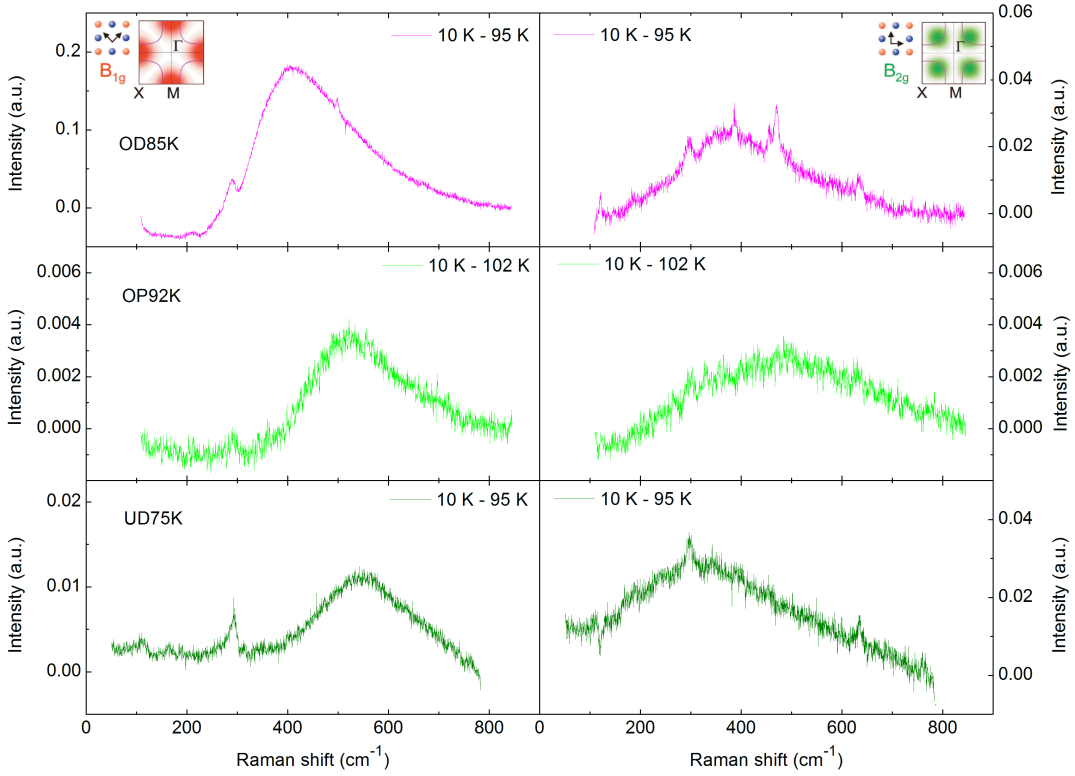

Figure 4.17: The difference between normal state (10 K above T_c) and superconducting state (at 10 K) of experimental ERS B_{1g} and B_{2g} spectra of Bi2212.

controlled by oxygen content from annealing single crystals in different conditions. Superconducting transition temperatures were checked by magnetic susceptibility. The ARPES and ERS experimental data of three Bi2212 samples with different doping levels, UD75K, OP92K and OD85K, was presented. The ARPES data of UD75K and OP92K is from previous studies. Both ARPES and ERS data is consistent with other previous reports.

Chapter 5

ERS Spectra Calculation for Cuprates $Bi_2Sr_2CaCu_2O_{8+\delta}$ in The Superconducting State

---

5.1 Kinetic theory calculation

5.1.1 Description for kinetic theory calculation

Symmetry of gap can give information about mechanism of pairing. In conventional superconductors, pairing is symmetric in BZ and the BCS s-wave pairing with phonon mediated mechanism was proposed and successfully explained their behaviors.

Unlike as BSC superconductors, in high-T_c superconductors, anisotropy of electron pairing was observed in experiments (figures 2.6, 3.12) and this was confirmed by so called kinetic theory of electronic Raman [43, 44]. In this theory electronic Raman response χ'' at a finite temperature is determined as

$$\chi''_{\gamma,\Gamma}(\omega) = \frac{\pi N_F}{\omega} \tanh\left(\frac{\omega}{4T}\right) Re\left\langle \frac{\gamma_{\mathbf{k}}\Gamma_{\mathbf{k}}|\Delta_{\mathbf{k}}|^2}{\sqrt{\omega^2 - 4|\Delta_{\mathbf{k}}|^2}} \right\rangle_{FS}, \tag{5.1}$$

in which N_F is density of state at Fermi level, Re denotes the real part and $\langle ... \rangle_{FS}$ denotes the average over the Fermi surface:

$$\langle A_{\mathbf{k}} \rangle = \frac{\int \delta(E_F - \epsilon_{\mathbf{k}}) A_{\mathbf{k}} d^2k}{\int \delta(E_F - \epsilon_{\mathbf{k}}) d^2k}. \tag{5.2}$$

γ and Γ are the bare and renormallized Raman vertices, ω is Raman shift and Δ is superconducting gap. From this theory by using different polarization geometry we can detect different region of BZ through Raman vertices.

In this theory δ function of density of state (DOS) was assumed along the Fermi surface and energy transferring between initial state and final state is sum up as illustrated in the figure 5.1. Strength of scattering is determined by Raman vertices, and for small momentum transfer (and incident light energy is smaller than optical band gap) Raman vertex is the curvature of a band dispersion:

$$\gamma_{\mathbf{k}} = m \sum_{\alpha,\beta} e^S_\alpha \frac{\partial^2 \epsilon_{\mathbf{k}}}{\partial k_\alpha \partial k_\beta} e^I_\beta, \tag{5.3}$$

where m is the electron mass, ϵ is conduction band dispersion, e^S and e^I denote respectively the polarizations of scattered light and incident light, α and β are coordinate indices.

The tight-binding model is usually applied for cuprates to study band structure which is a single band and has large density of state at Fermi level. For a tetragonal crystal in cuprates and with the tight binding model, the Raman vertices of B_{1g} and B_{2g} spectra are:

$$\gamma_{B_{1g}} = ma^2t[cos(k_xa) - cos(k_ya)],$$

$$\gamma_{B_{2g}} = 4ma^2t[sin(k_xa).sin(k_ya)].$$

With these Raman vertices B_{1g} spectrum probes the antinodal region ($(\pi, 0)$ or $(0, \pi)$) while B_{2g} spectrum probes the nodal region in the nodal direction (from (0,0) to (π, π)).

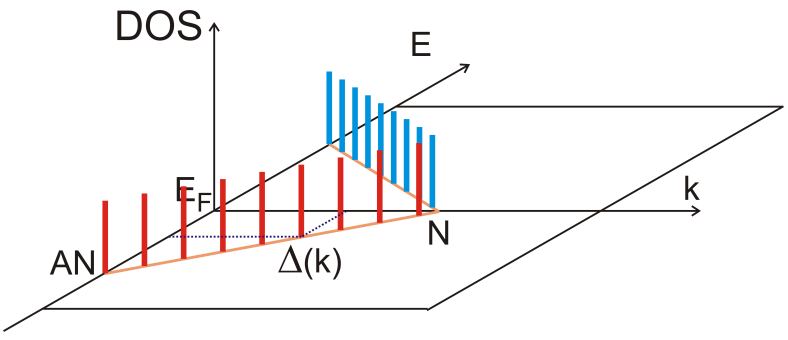

Figure 5.1: Illustration for kinetic theory calculation method. δ-function DOS along Fermi surface from node to antinode was used.

A d-wave gap profile which has a maximum gap at antinodal and a node in nodal line was used. The theory shows that B_{1g} spectrum will probe a superconducting coherent peak at 2Δ and B_{2g} spectrum will show a smaller gap at around 1.3Δ. The theory can explain successfully different behaviors of Raman spectra in low energy region, namely linear and cubic against Raman shift ω in B_{1g} and B_{2g} spectra, respectively. Here we have to emphasize that if the theory applied for superconductors which other symmetry of pairing including isotropic s-wave, mix $s+id$-wave, anisotropic s-wave, all of these symmetries cannot explain behaviors of Raman responses in cuprates. Therefore the kinetic theory confirmed the d-wave behavior of gap along Fermi surface in high-T_c cuprate superconductors. Figure 5.2 shows the original results of the kinetic theory and the ones applied for Bi2212 in superconducting state. The A_{1g} spectrum will probe both antinodal and nodal regions. However, to get good fit with the experimental data of Bi2212, a smearing width of $\Gamma/\Delta_0 = 0.15$ was used, which account for experimental resolution and possible additional scattering rate. In addition, in the calculation for simplicity the authors applied a cylindrical Fermi surface centered at $(0, 0)$.

As one can see from figure 5.2 that with a scattering rate B_{2g} peak position shifted a lot, namely it increases nearly to B_{1g} peak position 2Δ. The effect of scattering rate, that may come from impurity was more clarified in another study of these authors [156] where under the effect of scattering rate, when the scattering

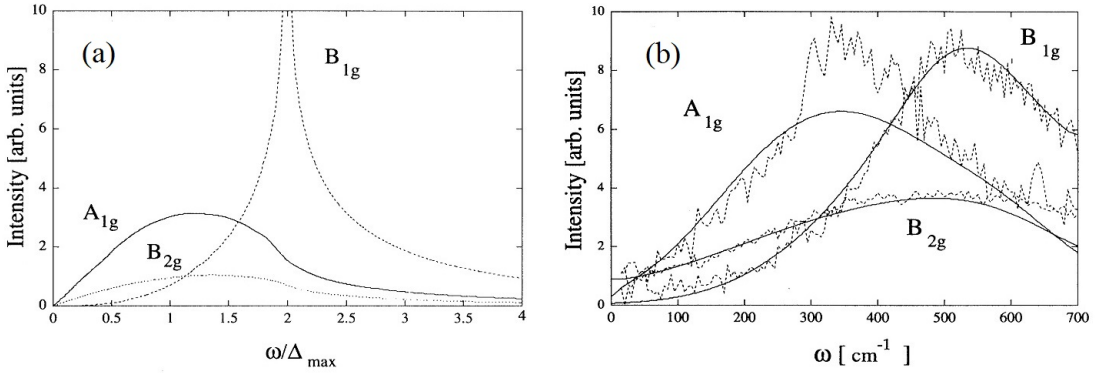

Figure 5.2: Calculation results of kinetic theory. a) electronic Raman response evaluated for d-wave pairing on a cylindrical Fermi surface for three symmetries B_{1g}, $B_{2g}$and A_{1g}. The Fermi surface is derived from tight-binding model. b) The kinetic calculations are compared to experimental results of an as-grown Bi2212 ($T_c = 90$ K) measured at 20 K in superconducting state. To get a good fit a smearing width $\Gamma/\Delta_0 = 0.15$ was applied [44].

rate increases, both B_{1g} and B_{2g} spectra become broader but the B_{1g} peak does not change the position much whereas the B_{2g} can shift strongly.

Before electronic Raman response of a *d*-wave gap superconductivity was derived by T.P. Devereaux and probed for high-T_c cuprates, a theory of electronic Raman scattering in an anisotropic-gap superconductor was presented by M.V. Klein and S.B. Dierker [157]. The theory was applied for V_3Si, a conventional superconductor with $T_c = 16.85$ K and saw that the peak in E_g symmetry is lower than the one in A_{1g} at least 10%. The Klein's theory was deduced by using Green function method and the derived formula is identical with the one of T.P. Devereaux when the wave vector $\mathbf{q}$ is zero.

The kinetic theory was verified for a lot of experimental Ramman data after its proof on *d*-wave pairing symmetry. It tells us that by choosing various geometries, electronic Raman scattering can probe different areas of BZ, and because of this, some characteristics of cuprates such as two energy scales were observed. So far there is a high consensus on *d*-wave pairing symmetry in cuprates although still there are some evidences for deviations. And so far the theory is the simplest one to describe electronic Raman scattering in cuprate superconductors.

5.1.2 Calculation for the optimally doped sample

For the kinetic theory calculation, only information of the Fermi surface and the gap profile is required with implication of tight-binding model for the band structure and bare Raman vertex for the renormalized vertex. Here, the density of states N_F can be considered as a constant. First of all, I will present the kinetic theory calculation for the nearly optimum-doped Bi2212 sample (OP92K). Figure 5.3 shows the Fermi surface and the *d*-wave gap profile along the Fermi surface of the sample OP92K, which were taken from ARPES data. The Fermi surface and gap profile were fitted to get fine input data for the kinetic theory calculation.

Figures 5.4 and 5.5 show kinetic theory calculation results for B_{1g} and B_{2g} spectra, respectively. These are calculated from the ARPES data in figure 5.3. In comparison, the experimental data at 10 K are presented, in which their intensities are normalized. The ω-cubic and ω-linear behaviors of B_{1g} and B_{2g} spectra, respectively, in the low-energy region were reproduced. The calculated B_{2g} peak is broad and appears at an energy lower than that of B_{1g} peak. This is the same as original

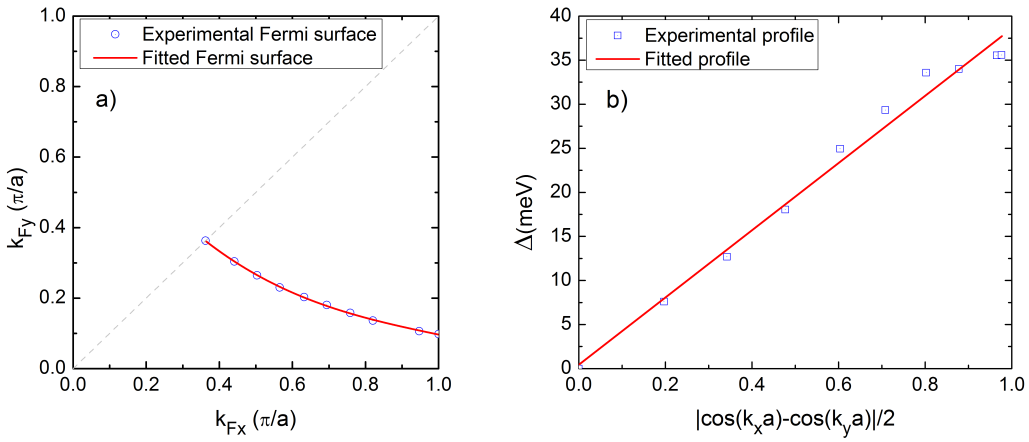

Figure 5.3: The Fermi surface in a) and gap profile along Fermi surface against *d*-wave function in b) of the sample OP92K (the nodal point is added). The red curve and linear line are fitted ones.

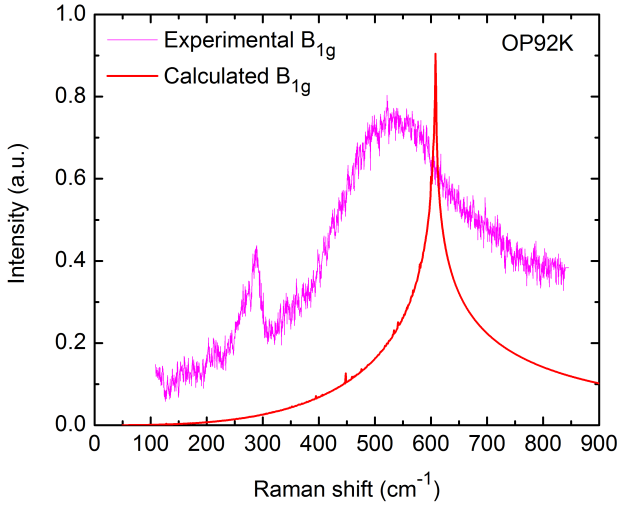

Figure 5.4: The B_{1g} kinetic calculation spectrum (red) using Fermi surface and gap profile in figure 5.3 in comparison to the experimental data (magenta) for the sample OP92K.

calculations of the kinetic theory (figure 5.2). However, one can clearly see that the B_{1g} peak energy is higher than the experimental one whereas inversely the B_{2g} peak energy is lower. The difference in B_{1g} spectra is $\approx$ 70 cm^{-1} ($\approx$ 9 meV) and in B_{2g} spectra it is 100 cm^{-1} (12 meV). This is unexpected from the kinetic theory where a sharp peak at energy 2Δ appears in B_{1g} spectrum. Since the gap profile

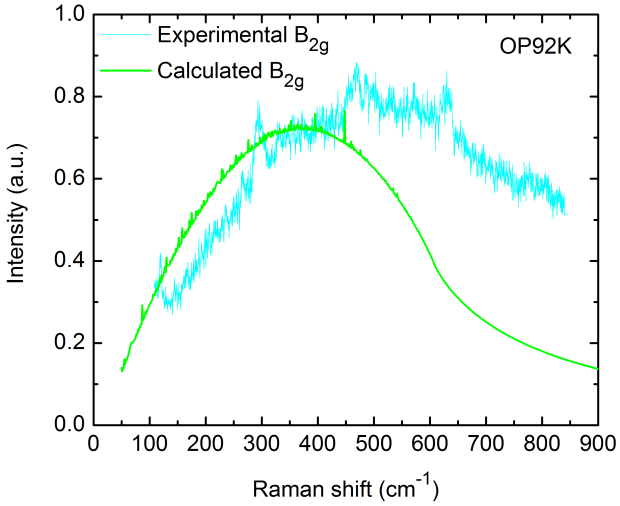

Figure 5.5: The B_{2g} kinetic calculation spectrum (green) using Fermi surface and gap profile in figure 5.3 in comparison to the experimental data (cyan) for the sample OP92K.

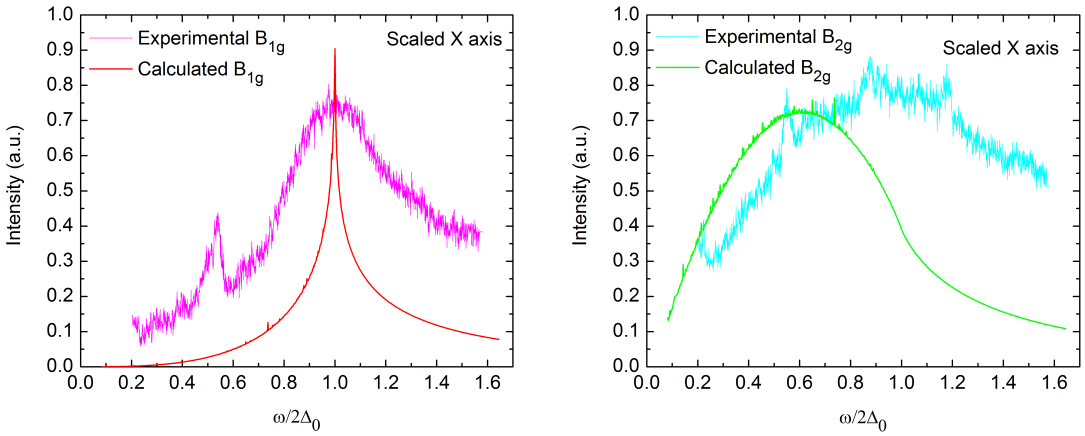

Figure 5.6: Comparison between kinetic calculation and experimental data of B_{1g} and B_{2g} spectra of the sample OP92K in which the energy axis is normalized for the B_{1g} peak energy.

is obtained from ARPES measurement, one can say that $2\Delta_{Raman} < 2\Delta_{ARPES}$.

The difference in B_{2g} spectra can be seen more clearly in figure 5.6 where the energy axis is scaled to get the same peak position in B_{1g} spectra. This discrepancy tell us that it requires a new approach to calculate electronic Raman spectra to get a good agreement between calculation and experiment in both B_{1g} and B_{2g}.

5.1.3 Doping dependence of kinetic theory calculation

Kinetic theory calculations were also done for the other samples with different doping levels, the underdoped sample UD75K and the overdoped one OD85K. The Fermi surface and the gap profile of the sample UD75K can be seen in figure 4.13.

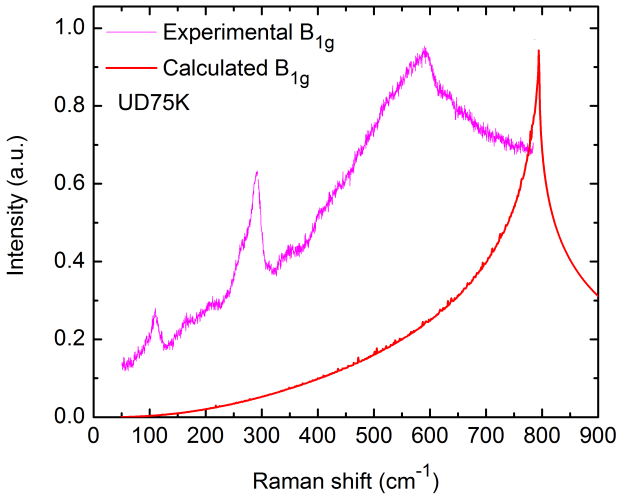

Figure 5.7: The B_{1g} kinetic calculation spectrum (red) in comparison to the experimental data (magenta) for the sample UD75K.

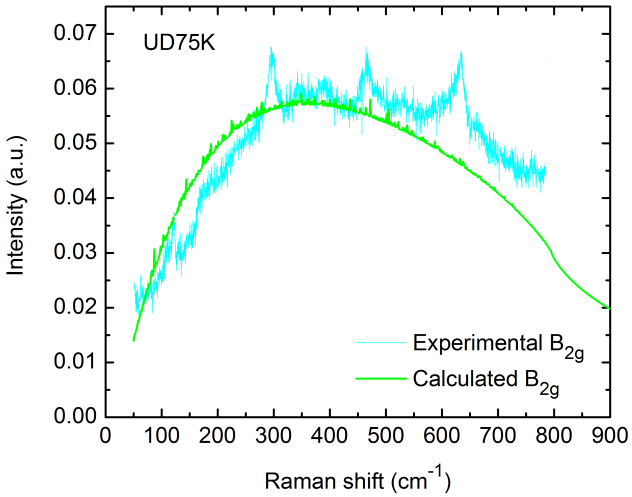

Figure 5.8: The B_{2g} kinetic calculation spectrum (green) in comparison to the experimental data (cyan) for the sample UD75K. While there is a big different in B_{1g}, the B_{2g} spectra quite fit each other.

There is a deviation from *d*-wave behavior near the antinodal region where the antinodal gap of UD75K is enhanced. Compared to the experimental data, the calculated B_{1g} peak position is at an energy much higher than the experimental one, up to 210 cm^{-1} (26 meV), as one can see in figure 5.7.

While there is no consistency in the calculated and experimental B_{1g} spectra in

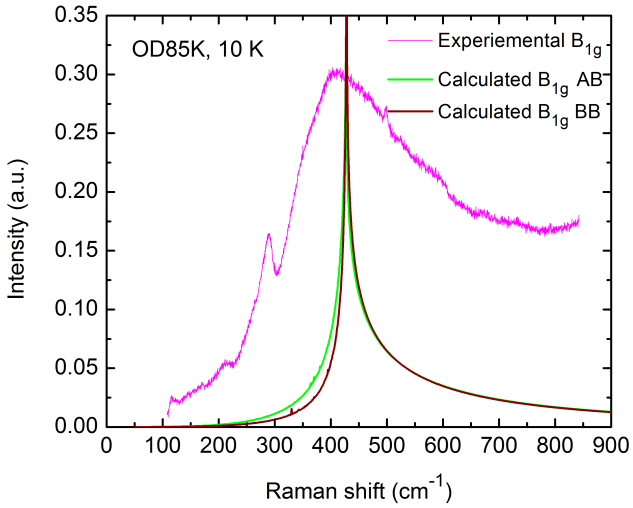

Figure 5.9: The B_{1g} kinetic calculation spectra with the bonding and antibonding band in comparison to the experimental data (magenta) for the sample OD85K.

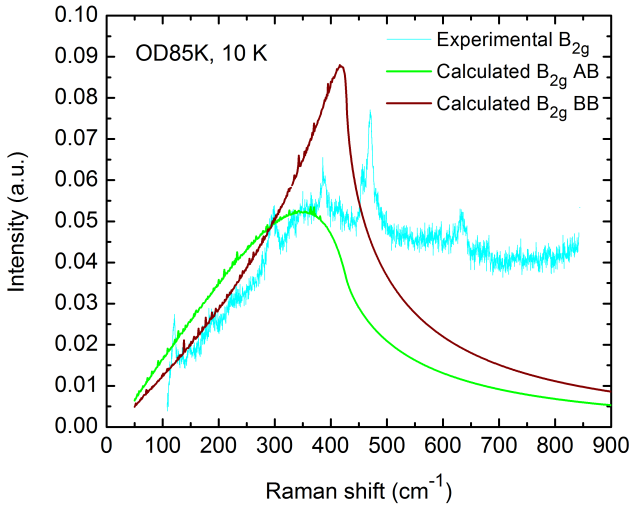

Figure 5.10: The B_{2g} kinetic calculation spectra with the bonding and antibonding band in comparison to the experimental data (cyan) for the sample OD85K.

UD75K, the B_{2g} spectra are fitted well although there is enhancement at the low energy region and suppression at the high energy region (figure 5.8). The difference in B_{2g} peak positions is just in 10 cm^{-1} ($\sim$ 1 meV).

Data of the sample OD85K is a little bit complex because of a bilayer splitting. Here we present kinetic theory calculations from the both antibonding band (AB) and bonding band (BB). The Fermi surface and the gap profile can be seen in figure 4.13.

Figures 5.9 and 5.10 present the calculation results of B_{1g} and B_{2g} in comparison to the experimental spectra. The peak positions of B_{1g} and B_{2g} AB spectra are fitted well to the experimental data, however the calculated B_{2g} BB spectrum shows a shape quite different from experiment where a sharp peak appears near 2Δ. This may be caused by the deviation of the gap profile from linear behavior and also depending on the shape of the Fermi surface.

Kinetic theory calculations are summarized in figures 5.11 for calculated Raman spectra.

It is clearly seen that the doping dependence of kinetic theory calculated B_{1g} spectra is consistent qualitatively in both peak position and intensity. B_{1g} peak energy increases with underdoping. The intensity of B_{1g} spectra decreases with underdoping and this behavior was mentioned in Ref. [45], figure 3.12. Here, to see clearly the doping dependence of the experimental B_{1g} intensity, I normalized the

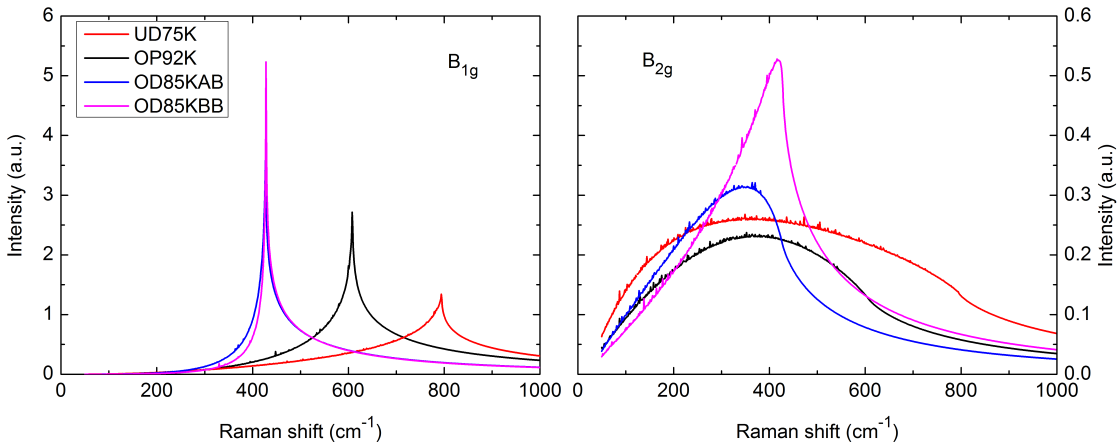

Figure 5.11: Doping dependences of the calculated Raman B_{1g} and B_{2g} spectra obtained from kinetic theory for Bi2212 samples.

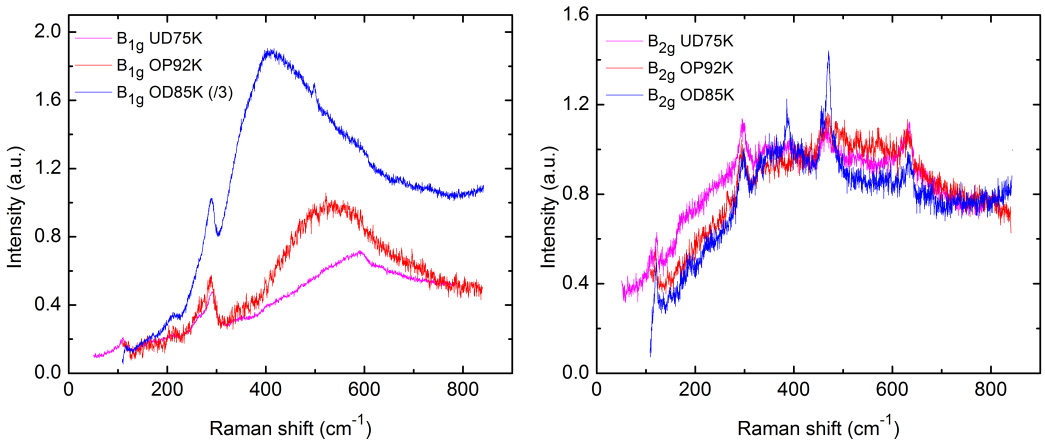

Figure 5.12: Doping dependence of B_{1g} intensity. The B_{2g} spectra were normalized and the same factors were applied for B_{1g} spectra.

B_{2g} spectra and applied the same factors for B_{1g} spectra, as shown in figure 5.12. The doping dependence of B_{2g} peak position is not clear and all of the spectra show nearly the same position. Therefore, the doping dependence of B_{2g} peak position does not follow an experimental T_c dome. The kinetic theory works for some aspects but quantitatively it is not satisfactory.

5.2 Kubo formula calculation

5.2.1 Description for Kubo formula calculation

To overcome the kinetic theory and try to get more realistic spectra, we applied a new method using ARPES data. ARPES intensity I is a function of matrix elements M, the Fermi-Dirac function f and a spectral function $A_{\mathbf{k},\omega}$,

$$I_{\mathbf{k},\omega} = I_0 \cdot M_{\mathbf{k}} \cdot f_\omega \cdot A_{\mathbf{k},\omega}. \tag{5.4}$$

Here I_0 is a constant. If the matrix elements do not have a strong momentum dependence, the spectral function can be obtained directly from ARPES spectra.

On the other hand, electronic Raman response χ'' in the superconducting state

can be deduced from Greens functions using the Kubo susceptibility [130] as follow

$$\begin{aligned}\chi''_{\gamma\Gamma} =& \frac{2}{\pi V}\sum_{\mathbf{k}}\gamma_{\mathbf{k}}\Gamma_{\mathbf{k}} \times \int_{-\infty}^{\infty} G''_{\mathbf{k},\omega}G''_{\mathbf{k},\omega+\Omega} \\ &\times \left(1 - \frac{\Delta_{\mathbf{k}}^2}{(\omega+\xi_{\mathbf{k}})(\omega+\Omega+\xi_{\mathbf{k}})}\right) \times \Big(f(\omega) - f(\omega+\Omega)\Big)d\omega,\end{aligned} \tag{5.5}$$

where $\gamma_{\mathbf{k}}$ and $\Gamma_{\mathbf{k}}$ are Raman vertices, $\Delta_{\mathbf{k}}$ is the superconducting energy gap, $\xi_{\mathbf{k}}$ is the bare band energy, V is the volume and f is the Fermi function. Since the Greens functions relate to the spectral functions through the relation [130]

$$G''_{\mathbf{k},\omega} = -\pi A_{\mathbf{k},\omega}, \tag{5.6}$$

therefore electronic Raman responses can be calculated from ARPES spectra. Raman verticies for B_{1g} and B_{2g} geometries in the d-wave symmetry of a teragonal structure with a lattice constant a and an electron mass m are

$$\gamma_{B_{1g},\mathbf{k}} = \Gamma_{B_{1g},\mathbf{k}} = ma^2t\Big(\cos k_x a - \cos k_y a\Big), \tag{5.7}$$

$$\gamma_{B_{2g},\mathbf{k}} = \Gamma_{B_{2g},\mathbf{k}} = 4ma^2t' \sin k_x a.\sin k_y a, \tag{5.8}$$

where t is a nearest neighbor hopping integral and t' is a next nearest neighbor hopping integral. The quantities γ and Γ are the bare vertex and renormalized vertex, respectively and in this study we use the same Raman vertex for both the bare vertex and renormalized one.

A tight binding model was applied for the band structure, which allows to obtain the Raman vertices above from the equation 5.3 and describe experimental ARPES data. The tight binding model in t and t' hopping limitation is

$$\xi_{\mathbf{k}} = -2t\Big(\cos k_x a + \cos k_y a\Big) + 4t' \cos k_x a.\cos k_y a - \mu, \tag{5.9}$$

where μ is a chemical potential. The parameter t, t' and μ were obtained by fitting tight binding band with ARPES experimental data.

Figure 5.13 illustrates a concept of our method where energy transfer is summed up in the same way as kinetic theory, however, the experimental ARPES EDC spectra were used instead of δ function density of state. In this calculation, not only for the density of states on the Fermi surface but also for the whole Brillouin zone could be done. The unoccupied states were obtained by symmetrizing the

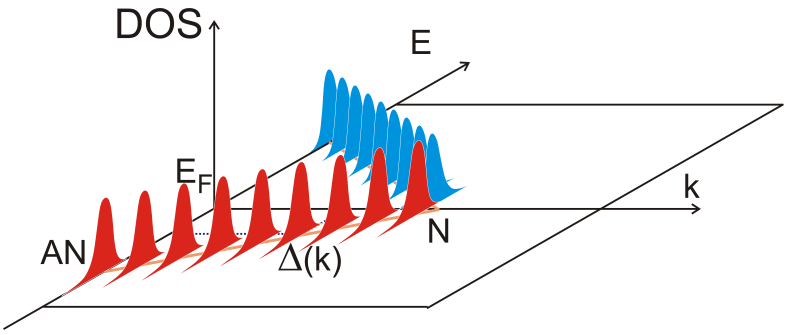

Figure 5.13: Illustration for our calculation method. In stead of δ-function DOS in the kinetic theory, the experimental ARPES EDC spectra were used, which include the real scattering rate.

ARPES EDC spectra against the Fermi level as shown in figure 5.21. A symmetric behavior of the density of state between occupied state and unoccupied state is supported by STS result where both states are probed (see figure 2.2). In general, because one can ignore the momentum transfer the calculation could be done for the whole Brillouin zone.

The band structure will be fitted by the tight binding model. A set of parameters $\{t, t', \mu\}$ of the tight-binding model was chosen to fit the Fermi surface and the band dispersion at nodal region simultaneously. Figure 5.14 shows the contour curve at the Fermi level fitting with the ARPES Fermi surface. And band dispersion fitted by the tight-binding model is presented in figure 5.15. The figure 5.15 C1 shows fitting results at the nodal cut. From the cuts in the middle region (cut C5) to the antinodal region (cut C8), there is a crossing between the tight-binding band and the experimental band. For calculation, a combination of two parts for band structure was used. One part is from the tight binding model and the other part is set to the experimental band. The modeled band structure is denoted by the yellow bold curves in fig 5.15 cut C5 and cut C8. For other cuts if there is no crossing we keep the tight binding band for that whole cuts.

The parameters used to fit the band structure for the sample OP92K are $t = 0.238$ eV, $t' = 0.392t$ and $\mu = -0.320$ eV.

The corresponding parameters for the sample UD75K are $t = 0.180$ eV, $t' = 0.490t$ and $\mu = -0.200$ eV and the ones for the sample OD85K are $t = 0.155$ eV, $t' = 0.440t$ and $\mu = -0.190$ eV.

Generally the renormalized Raman vertex should be derived as presented in

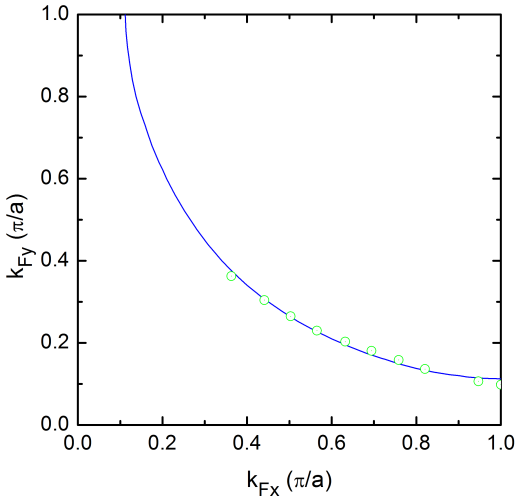

Figure 5.14: Fermi surface of the sample OP92K (dotted circle) and the contour at zero level obtained by the tight binding model with parameters $t = 0.238$ eV, $t' = 0.392t$ and $\mu = -0.320$ eV (blue smooth).

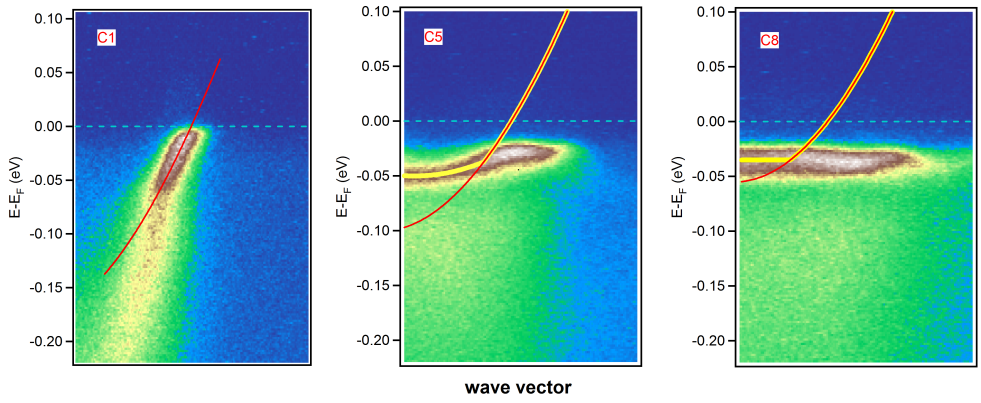

Figure 5.15: Experimental band dispersion versus the bare band from tight binding model. a) The cut C1 is the nodal cut. The tight binding band dispersion (the red curve) fitted well to the experimental band. b) The cut C5 is a cut in middle region. There is a crossing between the tight-binding band (the red curve) and the experimental band. The model for band dispersion (the yellow curve) is a combination of the tight binding model and experimental one. c) The cut C8 in the antinodal region as the same as the cut C5.

Ref. [130], however this is a complicated problem specially in the case strong interactions because it includes various types of final-state interaction. Several terms can contribute in the equation for the renomalized vertex including the bare vertex,

boson exchange terms, impurity scattering terms as well as the one from Coulomb screening effects [158]. And usually people consider just one of them, Coulomb screening [158], impurity [159], spin fluctuation [160], the screening effect [161]. The renormalized vertex could be derived from the interaction potential U through follow expression [130]:

$$\Gamma_{\mathbf{k},i\omega,i\Omega} = \gamma_{\mathbf{k}} + \frac{1}{V\beta}\sum_{i\omega'}\sum_{\mathbf{k}'} U_{\mathbf{k}-\mathbf{k}',i\omega-i\omega'} \times G_{\mathbf{k}',i\omega'} G_{\mathbf{k}',i\omega'+i\Omega}\Gamma_{\mathbf{k}',i\omega',i\Omega}. \tag{5.10}$$

Because of the complexity of renormalization, phenomenological formulae for the renormalized vertex were applied such as the one in Ref. [95] where

$$\Gamma_{\mathbf{k}} = \gamma_{\mathbf{k}}\tau_3 \exp[-\beta(\cos k_x a - \cos k_y a)^2]. \tag{5.11}$$

It may be still in good approximation that the renormalized vertex is replaced by the bare one (if the interaction is not too strong), where the main reason is just for simplicity and obtained results satisfied their studies [43, 99, 100, 108, 110].

5.2.2 Calculation using ARPES data only on k_F

First of all we show Kubo formula calculation for only-k_F for the sample OP92K. It means that only the EDC spectra on the Fermi surface were taken into account and this is similar to a kinetic theory calculation.

In this calculation, as the first test, the original ARPES spectra (the data at 10 K shown in figure 4.8 and with symmetrization against the Fermi level) were used. Figure 5.16 a) compares the B_{1g} and B_{2g} spectra calculated by kinetic theory and our method using Kubo formula. Since Kubo formula calculation uses ARPES spectra, which involves the experimental scattering rate information, one can see the effect of the scattering rate in this figure. The existence of scattering rate makes the B_{1g} spectrum broader and lowers the peak position, while the intensity in the higher energy region is enhanced in the B_{2g} spectrum. This enhancement of the spectral weight in B_{2g} spectrum tends to shift the peak position toward higher energy if scattering rate is large as expected by the previous report [156]. The shift of the B_{1g} peak position, on the other hand, was not expected by the previous report. This behavior implies that the momentum dependence of scattering rate, which is not taken into account in the previous reports, may cause this shift.

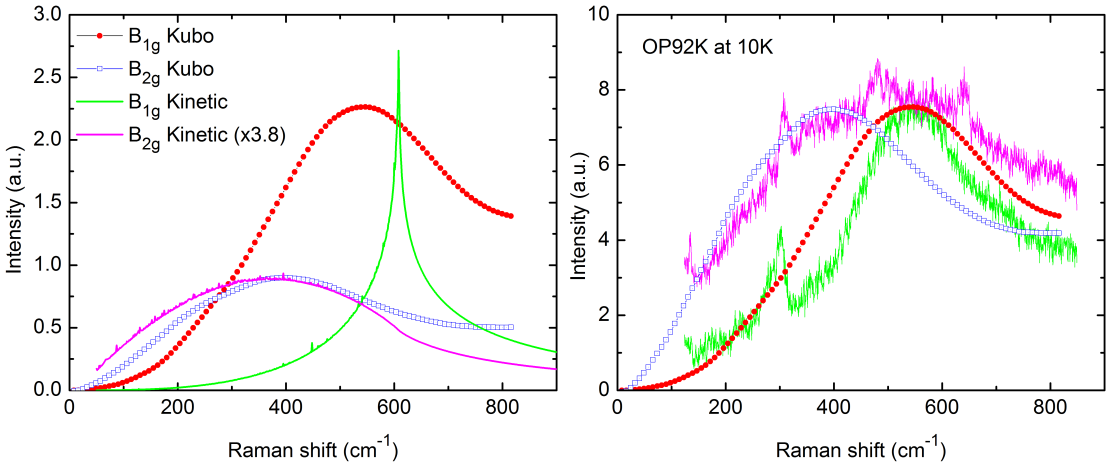

Figure 5.16: a) B_{1g} and B_{2g} calculated spectra by using Kubo formula and kinetic theory. b) B_{1g} and B_{2g} experimental ERS spectra and calculated ones using Kubo formula, using the raw ARPES data along Fermi surface for Bi2212 ($T_c = 92$ K) in superconducting state ($T = 10$ K). legend peaky

The B_{1g} and B_{2g} calculated spectra using Kubo formula are compared with the experimental data in figure 5.16 b). In B_{1g} spectra, there is a good agreement in both the peak position and the spectral shape in whole range, as well as ω-cubic behavior at the low energy region. The consistency between calculated and experimental B_{1g} peak positions could be understood because the B_{1g} peak energy is twice of the ARPES antinodal gap. The calculated B_{1g} spectrum is a little bit broader than the experimental spectrum. This may come from the background in ARPES spectra. In B_{2g} spectra, ω-linear behavior in the low energy region is obtained while the peak position shows significant difference (~ 100 cm^{-1}). This result indicates that the data of real scattering rate is not enough to reproduce the experimental B_{2g} peak position.

Here, it should be noted that the quasiparticle spectral weight $Z\Lambda$, which was introduced to qualitatively explain the doping dependence of the B_{2g} spectra [45], cannot explain this difference because it always lowers calculated B_{2g} peak position by decreasing the higher energy spectral weight from the larger gap region. One possible explanation of this difference is the contribution of the electronic structure from the whole BZ in the momentum space.

5.2.3 Calculation using ARPES data on the whole Brillouin zone

Here we want to explain why the calculated B_{2g} spectrum is expected to be improved with a whole-BZ calculation. Figure 5.17 illustrates the band structure and excitations around the Fermi surface. In previous section, we only used the electronic structure on the Fermi surface where the excitation gap of the spectral function is the smallest and ignored the electronic structure in the other region of Brillouin zone. If the electronic structures on the whole Brillouin zone are taken into account, the excitation with higher energy is naturally involved leading to an increase of intensity of calculated spectra in high ω region, and as a consequence leading to shift of peaks to higher energy. B_{2g} peak position is expected to shift to the higher energy because the Fermi velocity is large in the nodal region (figure 4.7). Therefore, further calculations including the electronic structure in the whole Brillouin zone is necessary to clarify whether ERS spectra, especially B_{2g} spectra can be reproduced from ARPES spectra or not.

The Brillouin zones of three samples OP92K, UD75K and OD85K are shown in chapter 4. Figure 5.18 shows calculation results with whole-BZ data of the sample OP92K. And figure 5.19 a) compares the B_{2g} calculated spectra using ARPES data on whole-BZ and only on the Fermi surface. We see that the B_{2g} peak shifts to higher energy as expected. It is clear that contribution from the electronic structure not on the Fermi surface is important. However, if we compare with the experimental data, there is one problem that intensity in high ω region of both B_{1g}

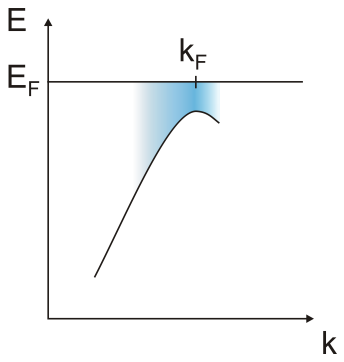

Figure 5.17: Illustration for excitation around Fermi surface. Excitation with larger gaps is involved in the whole-BZ calculation while intensity from k_F is the strongest.

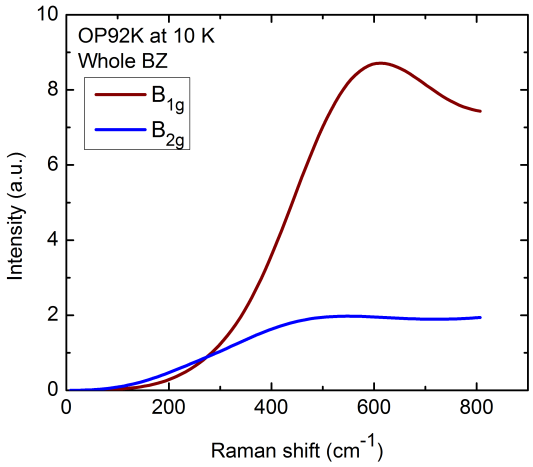

Figure 5.18: Calculated results of B_{1g} and B_{2g} spectra taking ARPES data on whole BZ.

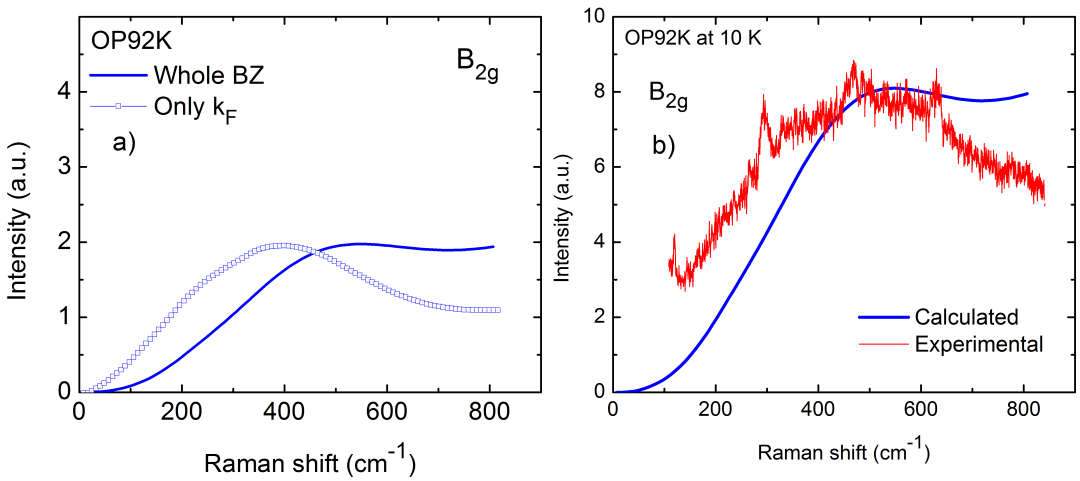

Figure 5.19: a) Comparisons between the whole-BZ calculation and the only-k_F calculation. b) Comparisons between the whole-BZ calculation and the experimental data.

and B_{2g} calculated spectra is too strong and this may be caused by a background in ARPES data. Therefore, subtracting background is one suggestion to improve calculated spectra.

5.2.4 Calculation with subtracting background

As presented in the chapter 3, the inelastic electrons contribute to the ARPES EDC spectra therefore the intensity from these electrons should be subtracted.

Here we subtract background in ARPES data using the Shirley background (bg), a phenomenological background, which has its form as follow:

$$bg_{Shirley} = c \int_{\omega}^{\infty} P(\omega')d\omega', \tag{5.12}$$

in which c is a coefficient, P is the primary spectrum after background subtracted. Value of c for each EDC spectrum is chosen so that the intensity at the highest binding energy in our measurement window typically ≈ 0.2 meV is composed all by background, which means that there is no contribution from elastic electrons at the highest binding energy.

Figure 5.20 presents one example for Shirley-background subtraction. The background nearly does not affect position of the coherence peak and especially the leading edge. Therefore background subtraction does not affect the gap size, it only suppresses intensity in high energy region. The important role of background subtraction will be clearer in later part when we compare result with and without background subtraction. The figure 5.21 shows symmetrized EDC spectra on Fermi surface of the sample OP92K measured at 10 K after Shirley background subtraction. In nodal region because of a nearly flat tail in raw spectra, the subtracted spectra have only coherence peak. For spectra in antinodal region after background subtraction there is still a small incoherence broad peak which will give small contribution in calculated results.

One interesting thing is that all measured EDC spectra in region near k-point (π, π) are the same as shown in figure 5.22. Spectral shape of these spectra can be used for a background, called k-independence background. The figure shows backgrounds for each cut in ARPES measurement which is average of more than 20 spectra near (π, π). It is also possible to take an average of all these background. The k-independence background is already mentioned and used by some studies [112, 126, 162, 163]. Here we confirmed that results obtained from k-independent is nearly the same as the ones using Shirley background. This can be understood when we compare Shirley and k-independent, as shown in figure 5.22. In this figure, the intensity is normalized in high energy region for two backgrounds.

The calculated B_{1g} and B_{2g} spectra of the sample OP92K using ARPES dat over the whole BZ and with Shirley-background subtraction are presented in figure 5.23. In comparison to the experimental spectra, their peak intensities are normalized in figure 5.24. The B_{1g} spectrum shows good agreement with the ex-

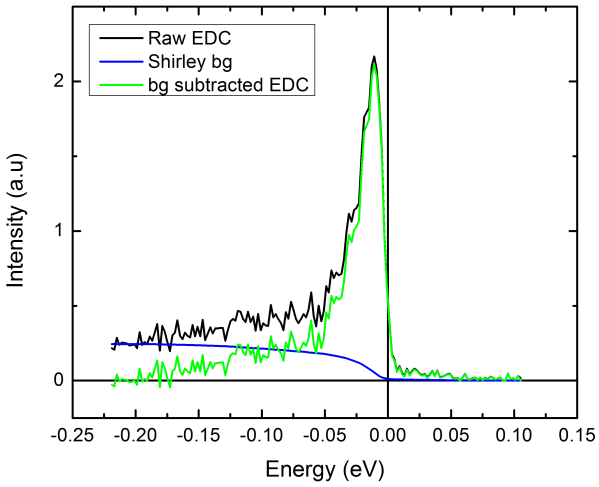

Figure 5.20: Shirley background subtraction for one EDC spectrum on Fermi surface near nodal region at temperature 10 K of the sample OP92K. The coefficient c in Shirley formula was chosen to normalize the intensity at high energy region.

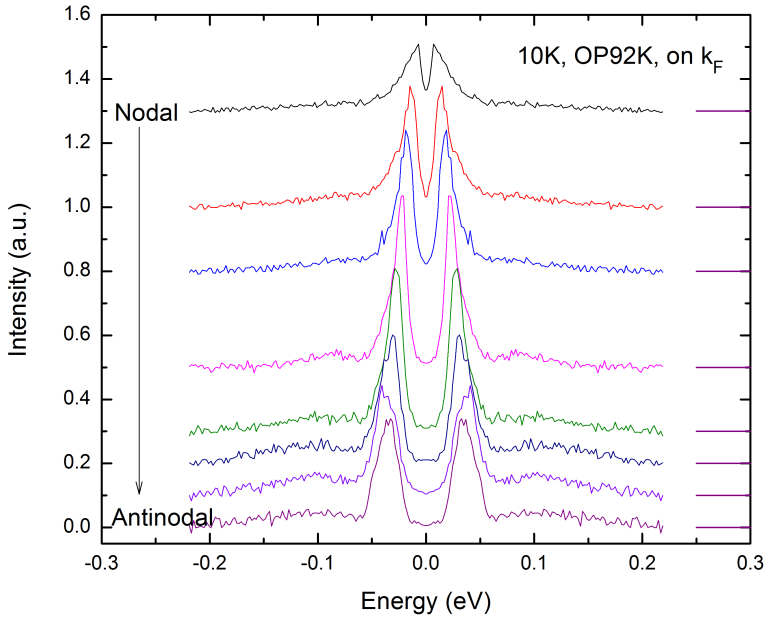

Figure 5.21: The EDC spectra at 10 K on k_F of the sample OP92K after Shirley-background subtraction. Spectra were offset in vertical axis, horizontal bars on right side denote zero value.

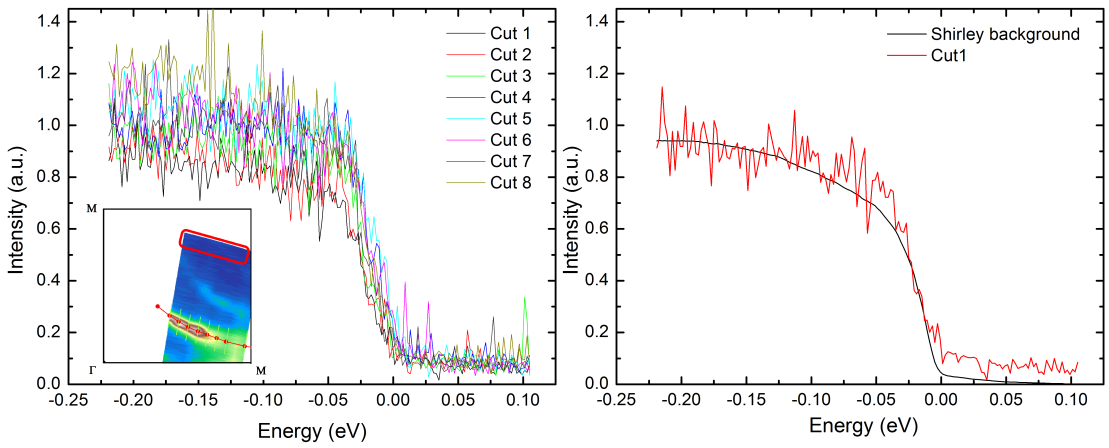

Figure 5.22: a) EDC spectra in the region near (π, π) (the area determined by the red round-corner rectangle in the inset) can be considered as background so called k-independent background. Each background is the average of 20 EDC spectra corresponding to each measurement cut. b) Comparison between the k-independent background and the Shirley background obtained from the EDC at k_F of the nodal cut of the sample OP92K. Two backgrounds are normalized their intensities at highest energy region.

perimental spectrum. Its peak position is a little bit higher than experiment about 35 cm^{-1}(4-5 meV). In the sample OP92K, the experimental B_{1g} Raman peak and ARPES antinodal gap $2\Delta_{ARPES}$ are quite close together, 535 cm^{-1} (66 meV) and 72 meV (580 cm^{-1}), respectively. And this is one reason leading to the proximity of calculated spectrum to the experimental one.

There is a big improvement of peak position in the calculated B_{2g} spectrum in comparison to the only-k_F calculation. The peak position in the whole-BZ calculation is the same as the experimental data although the calculated spectrum is not as broad as the experimental one. This result indicates that it is really important to involve the whole Brillouin zone information to reproduce Raman spectra.

It also needs to confirm the importance of background subtraction from these calculations. With a proper model for ARPES background such as Shirley background, ERS spectra could be reproduced. Background subtraction is one critical step in these calculations.

The whole-BZ calculation with Shirley background subtraction was also done for the samples UD75K and OD85K. The figure 5.25 shows the calculated B_{1g} and

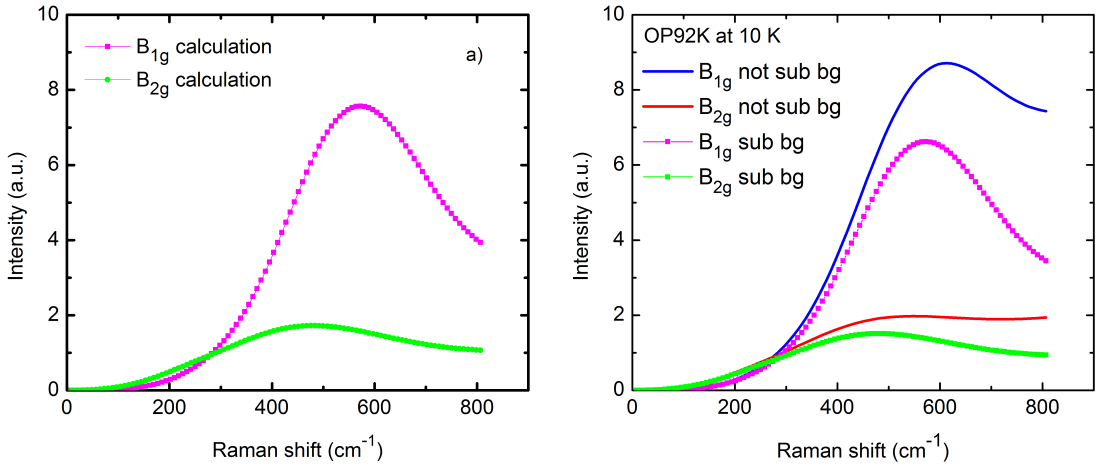

Figure 5.23: a) The calculated B_{1g} and B_{2g} spectra of the sample OP92K for superconducting state (10 K) using the ARPES data on the whole BZ and subtracted Shirley backgrounds. b) Comparison between calculated spectra on the whole BZ with and without Shirley background subtraction ("sub bg" and "not sub bg", respectively).

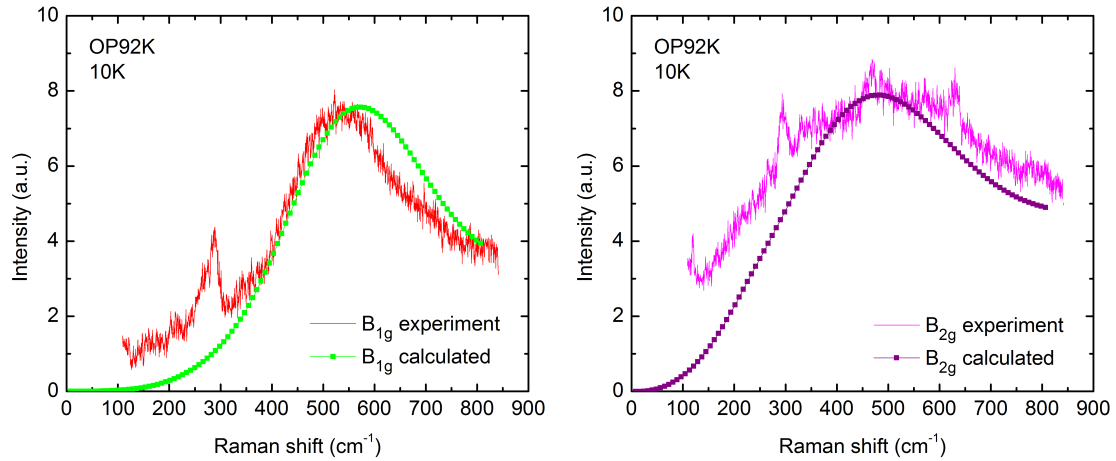

Figure 5.24: The calculated B_{1g} and B_{2g} spectra in comparison to the experimental ones of the sample OP92K measured at 10 K. The calculated spectra were normalized their intensities to the experimental spectra.

B_{2g} spectra together with the experimental data of the sample UD75K.

The difference in peak position in both B_{1g} and B_{2g} spectra between the calculation and the experiment increases to about 100 cm^{-1}. One should be noticed that in the experimental B_{1g} spectrum there is one phonon peak at 590 cm^{-1} [28]

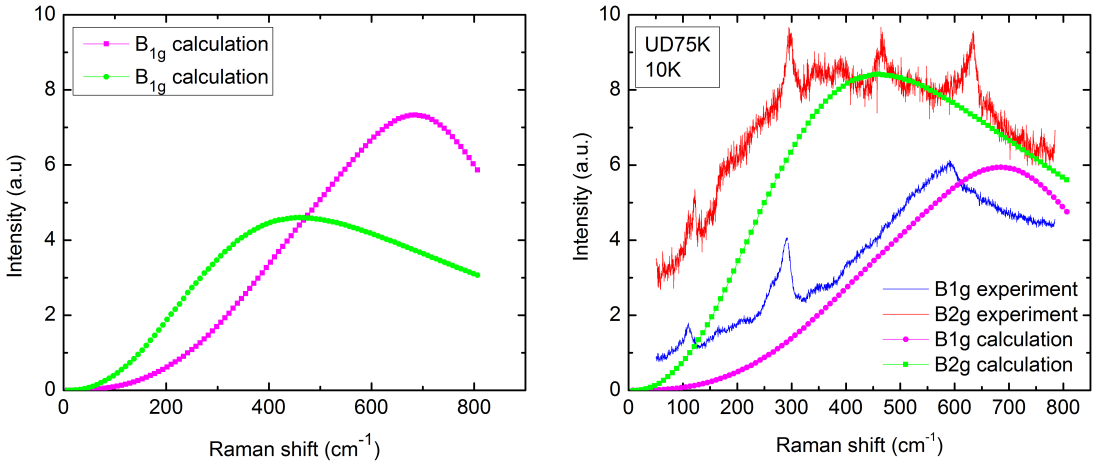

Figure 5.25: a) The original calculated B_{1g} and B_{2g} Raman spectra of the sample UD75K using ARPES data on whole BZ and subtracted Shirley backgrounds. b) Comparison between the calculation results and experimental data, the calculated spectra were normalized their intensity to the experimental ones.

which is nearly the same peak position of electronic spectrum. This phonon peak makes the experimental B_{1g} spectrum look sharp, however it could be wiped out by subtracting spectra in the normal and the superconducting states (figure 3.12). The calculated B_{2g} spectrum is broad and fits the experimental data in high energy region but not in low energy side. The difference in B_{1g} peak energy may be caused by a pseudogap, which may affect and make deviation in the gap profile along the Fermi surface from *d*-wave around the antinodal region (figure 4.13). That is not attributed for expansion from the only-k_F calculation to the whole-BZ one which involves larger gap because the gap in the antinodal region in ARPES ($2\Delta = 96$ meV ($\sim$ 770 cm^{-1})) already larger than the experimental B_{1g} gap (580 cm^{-1} (72 meV)).

For the overdoped sample OD85K we had to apply a special treatment for ARPES data, because there is a bilayer splitting leading to an antibonding band (AB) and a bonding band (BB). A band structure model deviating from tight-binding model can be applied for the case of bilayer splitting as in Ref. [164], however in this study we calculated only for the BB. The reason why the BB is chosen is the AB in the antinodal region is too close to *k*-point $(\pi, 0)$ and could be superposed by umklapp bands from another quadrant of Brillouin zone [77]

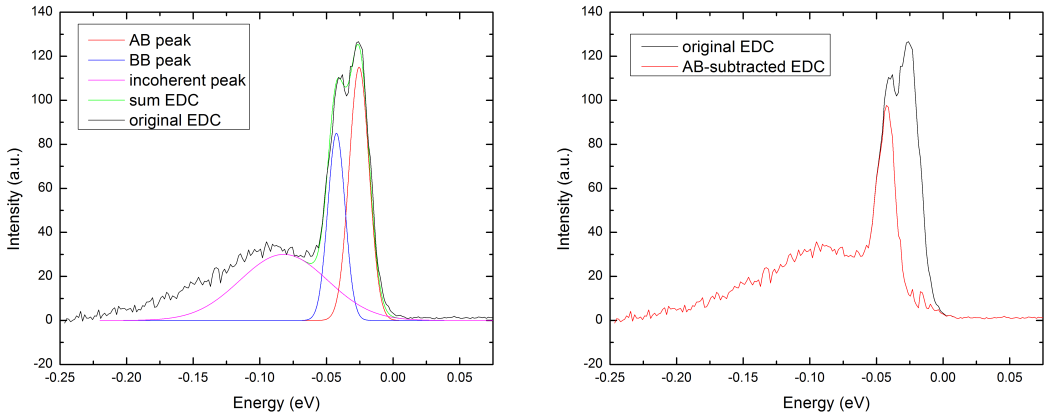

Figure 5.26: An example for subtracting the antibonding band (AB) peak from EDC spectra in which there is superposition of antibonding band and bonding band (BB), the sample OD85K.

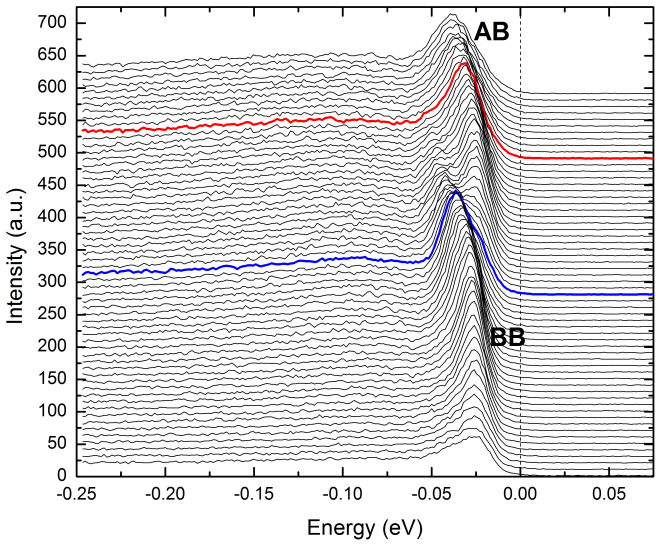

Figure 5.27: EDC spectra between the red and the blue ones are subtracted for the AB peak. Here is energy dispersion along the cut 8 at middle region and EDC spectra are offset in the vertical axis.

and with BB we could avoid this problem. Therefore for the k region where superposition of two bands exists, EDC spectra were fitted by Gaussian functions corresponding to a BB peak, an AB peak and an incoherent part, as shown in figure 5.26. To discuss the spectral weight from BB, the Gaussian AB peak is subtracted from these EDC spectra. This procedure was applied from cut 4 in

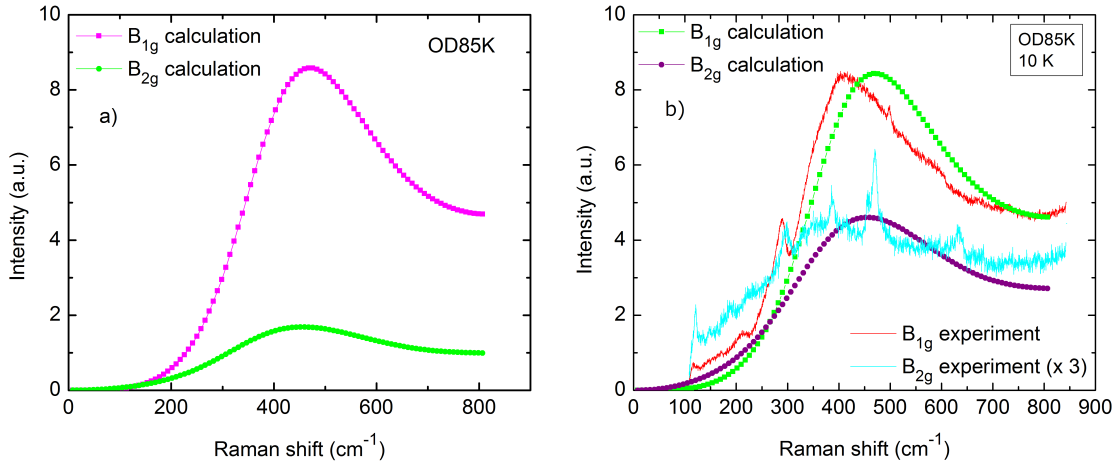

Figure 5.28: a) The original calculated B_{1g} and B_{2g} Raman spectra in superconducting state of the sample OD85K using ARPES data on whole Brillouin zone and subtracted Shirley backgrounds b) Comparison between the calculation results and experimental data, the experimental B_{2g} is multiplied by a factor of three to see more clear and the calculated spectra were normalized their intensity to the experimental ones.

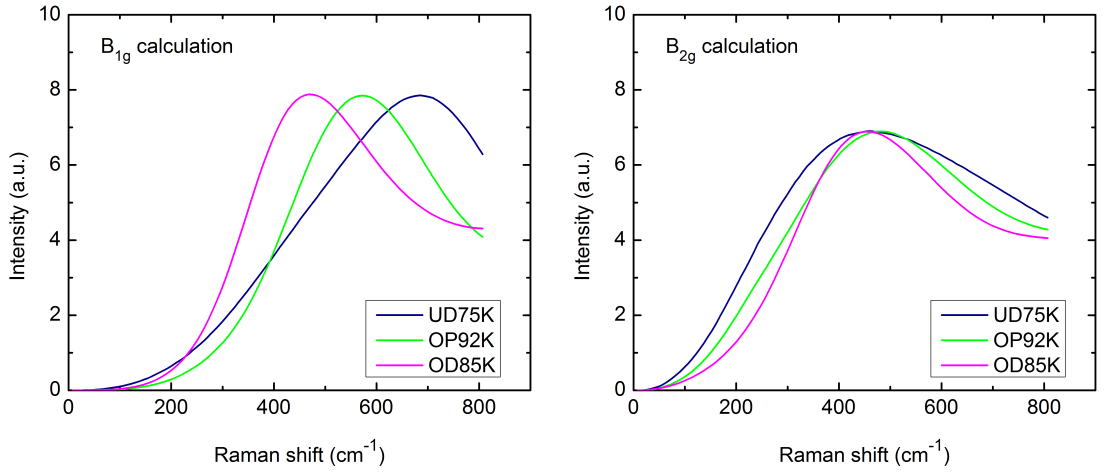

Figure 5.29: Doping dependence of calculated spectra in two geometries B_{1g} and B_{2g}. Peak position in B_{1g} increases clearly with underdoping while it changes lightly with a dome shape in B_{2g}.

figure 4.10 b) where the bilayer splitting starts to be clear to the last cut in the antinodal region. The figure 5.27 shows an example of the k-point region where the AB peak is subtracted.

Figure 5.28 shows the calculation results in comparison to the experimental data for the sample OD85K. The calculated B_{1g} spectrum has a quite good shape

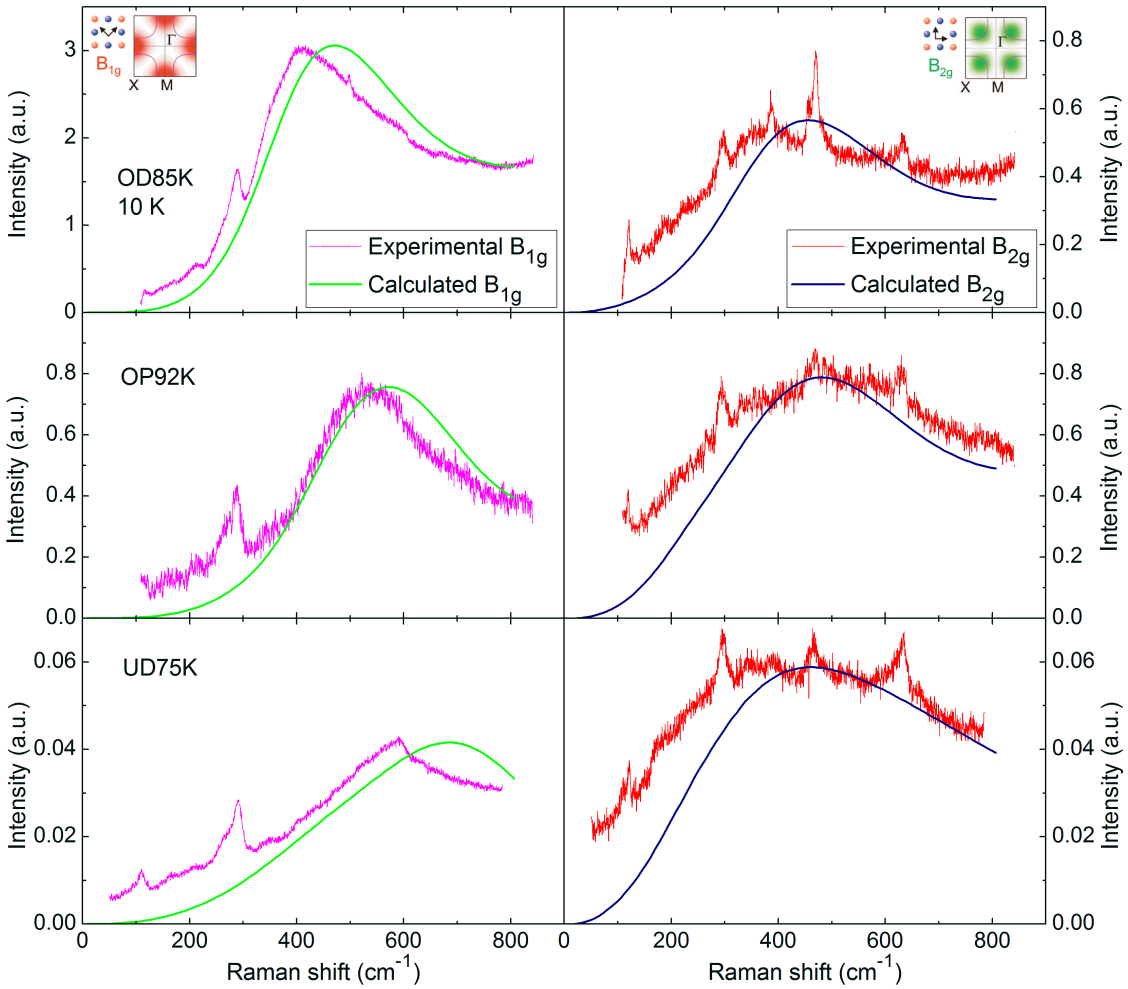

Figure 5.30: Summary of all whole-BZ Shirley-background-subtracted calculation results in comparison to the experimental data.

and the difference between calculation and experiment is 60 cm^{-1}. In figure 5.28, the experimental B_{2g} spectrum is multiplied by a factor of three to see clearer. The difference in B_{2g} is about 70 cm^{-1} a little bit more than B_{1g}.

Here we summarize the calculated B_{1g} and B_{2g} spectra from Kubo formula in figure 5.29 to see their doping dependence. The calculated B_{1g} peak position clearly moves to higher energy with underdoping while B_{2g} one does not show clear shift as seen in the experimental one, however two different energy scales still can be seen.

All whole-BZ Kubo-formula calculations presented above are summarized in comparison to the experimental results in figure 5.30. It is clear that whole-BZ

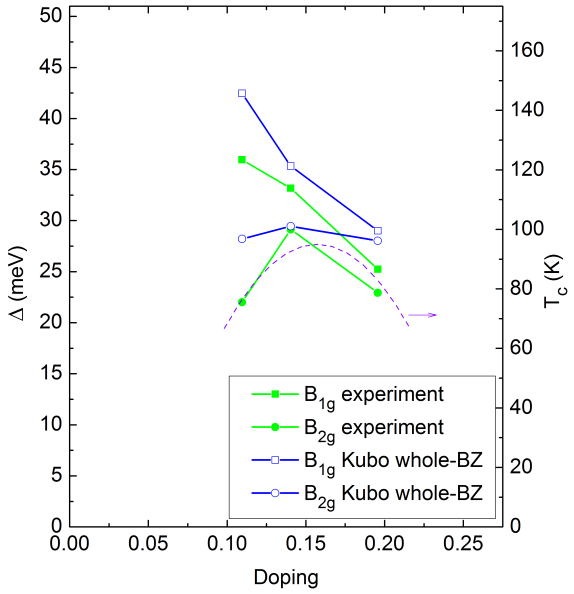

Figure 5.31: Doping dependence of the gap size obtained from the kinetic and Kubo calculations in comparison to experimental data. The dashed curve is T_c dome obtained from the empirical equation 2.1 with T_c^{max} is 95 K.

calculation can reproduce both B_{1g} and B_{2g} spectral shape better than kinetic theory calculation. However, one can still see differences between the calculation and the experiment. In B_{1g}, peak positions are slightly different, ≈ 100 cm^{-1}. In B_{2g}, spectra do not show ω-linear dependence and the experimental spectra always show more intensity than the calculated spectra at low frequency. To see the peak energy difference between the Kubo whole-BZ calculation and the experiment, we summarize the doping dependence of peak energy of B_{1g} and B_{2g} spectra in figure 5.31. We see that Kubo calculation always shows larger energy than the experiment. For B_{2g} peak, Kubo calculation has less doping dependence. From these calculations with background subtraction for the ARPES EDC spectra leaving mainly the coherence peak, we see that the electronic Raman spectra B_{1g} and B_{2g} are related to coherence excitation. However, it is hard to confirm these peaks are related only to superconducting state as in Ref. [45] because the coherence peaks in ARPES data appear already in the normal state even at the nodal region and continuously evolve into the superconducting state (figures 3.4 and 4.8).

We also can see that for the Kubo calculation, B_{1g} and B_{2g} peak energies are close together in the onverdoped side and depart with underdoping.

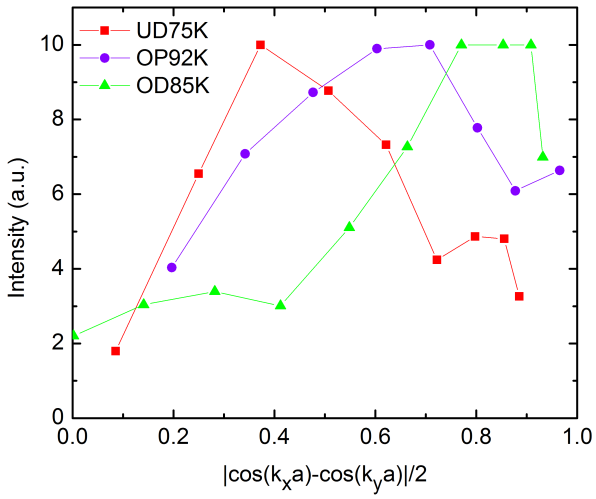

Figure 5.32: Experimental intensity profiles along Fermi surfaces of three samples.

5.2.5 Calculation taking into account the matrix element effect

As shown in the section 5.2.4, although the Kubo-formula whole-BZ calculation reproduces the experimental Raman spectra better than the kinetic theory, there still exists differences between the calculation and the experiment. Especially in B_{2g}, the calculated spectra show weak intensity at low frequency region. This result implies that the calculations lack the contribution from the electronic structure of lower energy gap region, namely the nodal region. In figure 5.32, we plot the momentum dependences of the experimental peak intensity at k_F for three samples with different doping levels. These momentum dependences are nonmonotonic. And these are the intensity profiles of $A_{\mathbf{k},\omega}$ we used in the previous sections. As discussed in the section 3.1, these profiles should be modulated by matrix elements and they may not represent the real $A_{\mathbf{k},\omega}$ intensity profile. This effect of matrix elements may cause the difference between the calculation and the experiment. Since it is hard to obtain the information of matrix elements from ARPES measurement itself, here, we assume several simple types of intensity profile along the Fermi surface for $A_{\mathbf{k},\omega}$ and try to reproduce the experimental data.

First we consider the overdoped sample OD85K. Figure 5.33 presents the experimental peak-intensity of the EDC spectra on Fermi surface of the sample OD85K, together with three assumed profiles. The EDC spectra on different cuts of ARPES

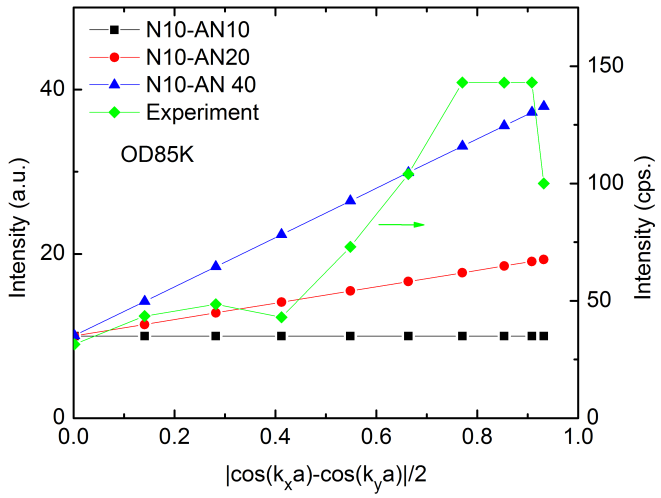

Figure 5.33: The experimental intensity profile of EDC spectra against the d-wave function along the Fermi surface of the sample OD85K and three linear assumed profiles (N10-AN10, N10-AN20 and N10-AN40). The experimental profile is converted to an assumed profile by different factors for different k-points and then these factors were applied for corresponding cuts. N denotes for the nodal region and AN denotes for the antinodal region.

measurement are multiplied by corresponding factors which convert the experimental profile to an assumed profile. The calculation for ERS spectra then were done in the same way with Shirley-background-subtracted whole-BZ Kubo-formula calculation.

Figure 5.34 shows the results of B_{1g} and B_{2g} calculations in which linear intensity profiles are applied. We see that with the assumed profiles, for the sample OD85K, there is no clear change in B_{1g} spectra, while in B_{2g} there is an improvement and the spectral weight in low energy region is filled.

The same procedure was applied for the samples OP92K and UD75K. The profiles used to investigate are shown in figure 5.35 for the sample OP92K and the calculation results are presented in figure 5.36. It is similar to the case of OD85K, with an improvement in B_{2g} spectra and no much change in B_{1g} when the profile changes from N10-AN10 to N10-AN5. With further reduction of intensity in the antinodal region, the high energy part in the B_{2g} spectrum increases.

For the sample UD75K with simple linear profiles as shown in figure 5.37, we did not get a good agreement between the calculated and experimental spectra.

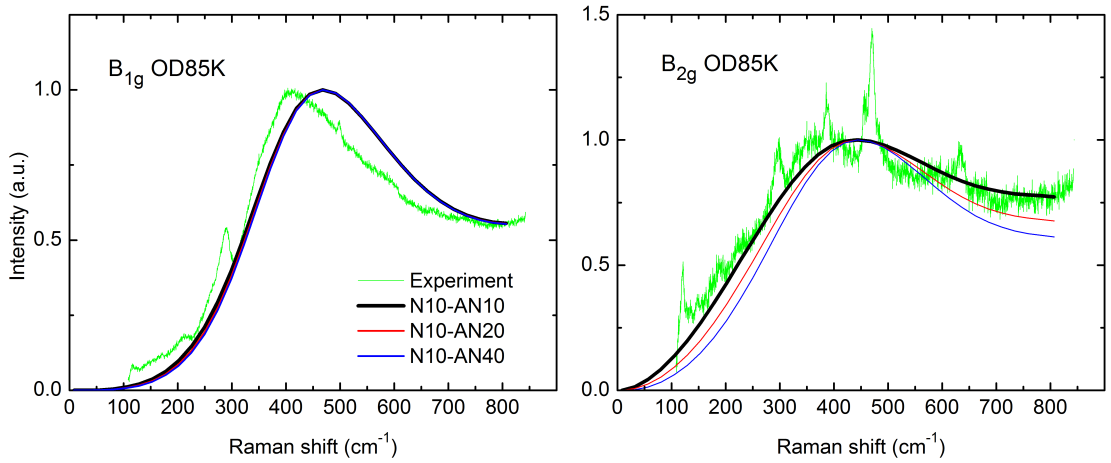

Figure 5.34: B_{1g} and B_{2g} calculated spectra in which linear profiles are applied, in comparison to the experimental data. There is no clear change in B_{1g} while the spectral weight in low energy region is filled with uniform intensity from the nodal region to the antinodal region. Calculated spectra were normalized.

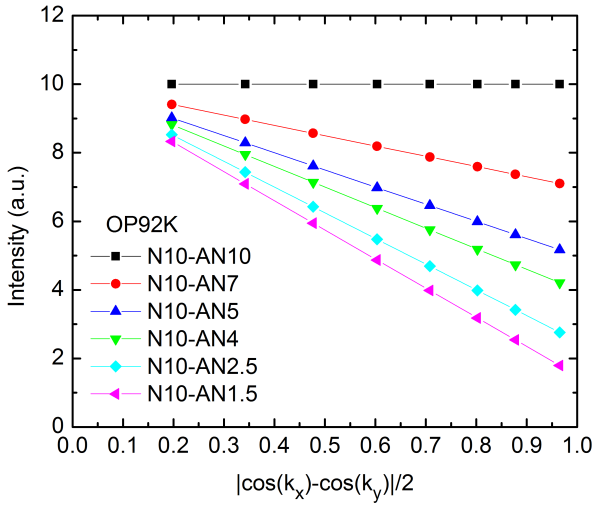

Figure 5.35: Linear profiles applied for the sample OP92K.

However, when intensity in the nodal region decreases from the profile N10-AN10 to the profile N10-AN1, the tendency is that the spectral weight in low energy region of both B_{1g} and B_{2g} is filled and the B_{2g} peak shifts to lower energy as one can see in figure 5.38. We also found out one "special profile" which enhances intensity near the node which helps to get better fit in B_{2g} spectra. The reason for

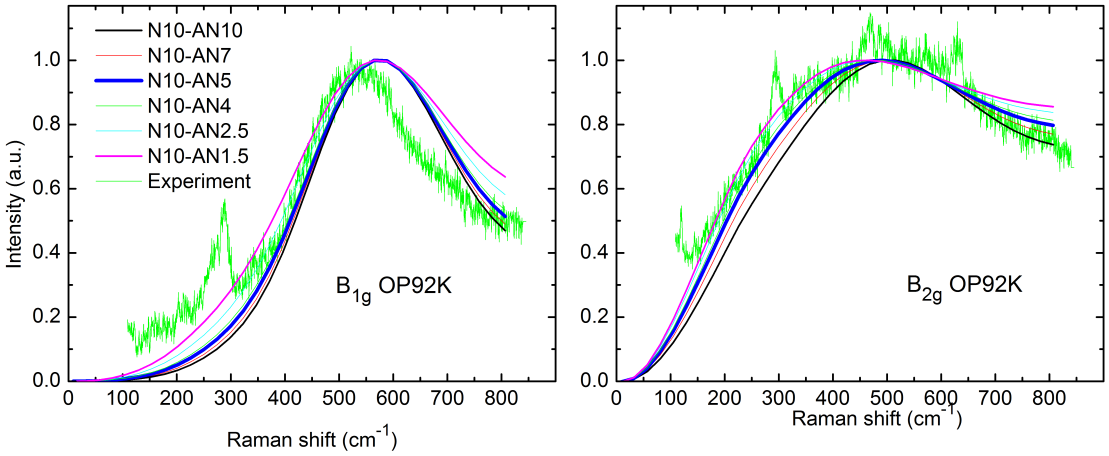

Figure 5.36: B_{1g} and B_{2g} calculated spectra of the sample OP92K in which linear profiles are applied. Calculated spectra were normalized. The best profile is around N10-AN5.

this peak-like shape profile is not clear. To clarify whether this peak is real or not, more study for doping levels around UD75K is necessary.

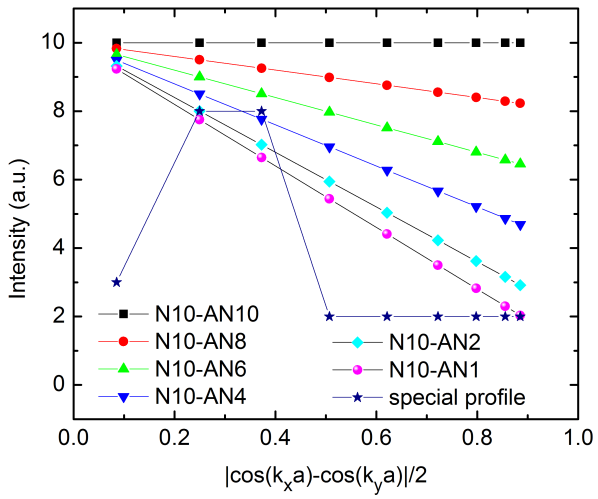

Figure 5.37: Linear profiles applied for the sample UD75K.

Comparing profiles which help to improve the calculated Raman spectra for three samples, we see that different doping level has different intensity profile. In figure 5.39, the best profiles of $A_{\mathbf{k},\omega}$ to reproduce Raman spectra are summarized. It shows that the spectral weight confined around the nodal region distributes to

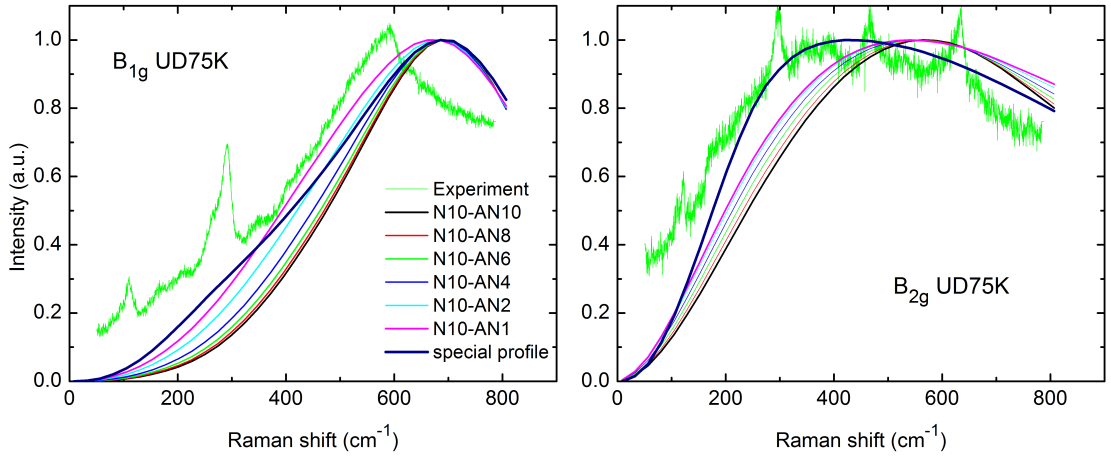

Figure 5.38: B_{1g} and B_{2g} calculated spectra of the sample UD75K in which linear profiles are applied. Calculated spectra were normalized. When intensity at the antinodal region reduces, there is an improvement in the B_{2g} spectrum although with the assumed linear profiles, it is not enough to reproduce the experimental spectra.

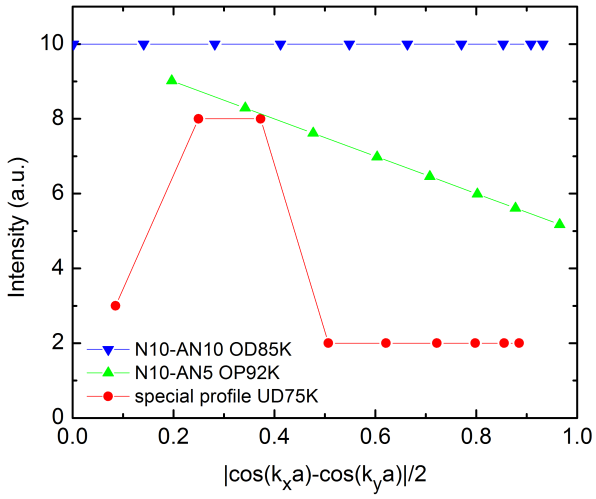

Figure 5.39: Assumed profiles which give improvements in Raman calculated spectra. It shows that with underdoping the intensity in the nodal region is enhanced more and more comparing to intensity in antinodal region.

the antinodal region with doping. It should be noticed that these intensity profiles of $A_{\mathbf{k},\omega}$ cannot be solely obtained by ARPES measurements because it is not easy to clarify the effect of matrix elements.

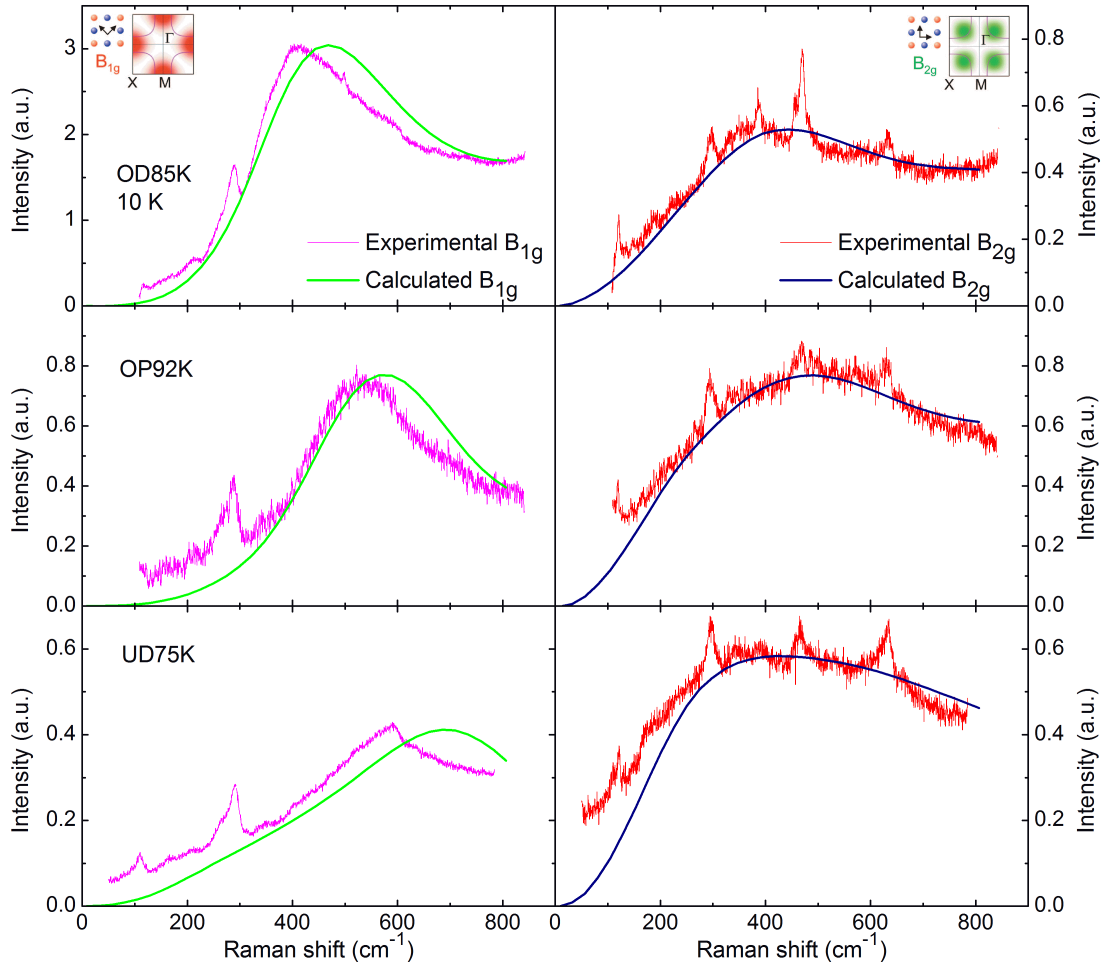

Figure 5.40: Summary calculations with the assumed profiles which help to get best fits, N10-AN10 for OD85K, N10-AN5 for OP92K and the special profile for UD75K.

The calculations with the best profiles are summarized in figure 5.40. One can easily tell that there is a good agreement between the calculation and the experiment.

Chapter 6

Discussion: Meaning of the present results

6.1 Implication of doping dependence of the intensity profile of $A_{\mathbf{k},\omega}$

Figure 5.39 shows doping dependence of spectral weight distribution and this result cannot be obtained solely by ARPES measurements because of matrix element effect. Here in this study, the result could be obtained by comparing Raman and ARPES.

Figure 5.39 shows that $A_{\mathbf{k},\omega}$ confined in the nodal region distributes to the antinodal region with doping. This is consistent with a recent report that the superconducting spectral weight is suppressed by the competing pseudogap at the antinodal region, figure 6.1. Figure 5.39 can be understood as the recovery of superconducting spectral weight with doping because the pseudgap becomes weaker.

This result can be also related to so-called "dichotomy" as shown in figure 6.2. It is well-known that there is a crossover of the sharper superconducting peak from the nodal region to the antinodal region with doping, which implies that the antinodal region getting more important for superconductivity with doping. Our results suggest that the importance of the antinodal region for superconductivity is also controlled by recovery of the spectral weight at the antinodal region with doping.

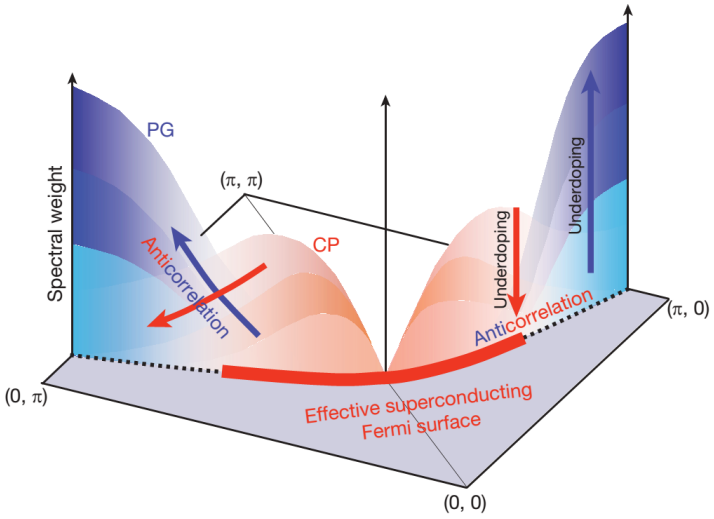

Figure 6.1: The competition between the pseudogap (PG) and superconductivity. Inverse evolution of the coherent and pseudogap spectral weights in momentum space and by doping result in the effective region of the superconducting quasiparticles. CP denotes for coherent peak [165].

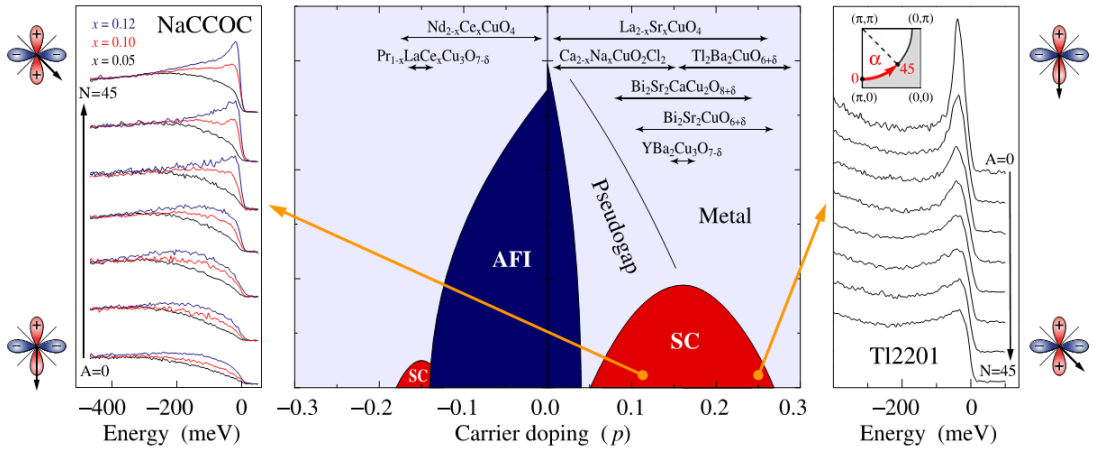

Figure 6.2: The sharper peak in ARPES data moves from the nodal region to the antinodal region with doping [166]. In underdoped cuprates, here is $Ca_{2-x}Na_xCuO_2Cl_2$ (NCCOC), the sharper peak is at the node, whereas in overdoped $Tl_2Ba_2CuO_{6+\delta}$ (Tl2201) it is at the antinode

6.2 Doping dependence of the superconducting gap

From figure 5.40, it is clear that the B_{2g} spectra, which are sensitive to the superconducting gap profiles along Fermi surfaces, are well reproduced by the ARPES

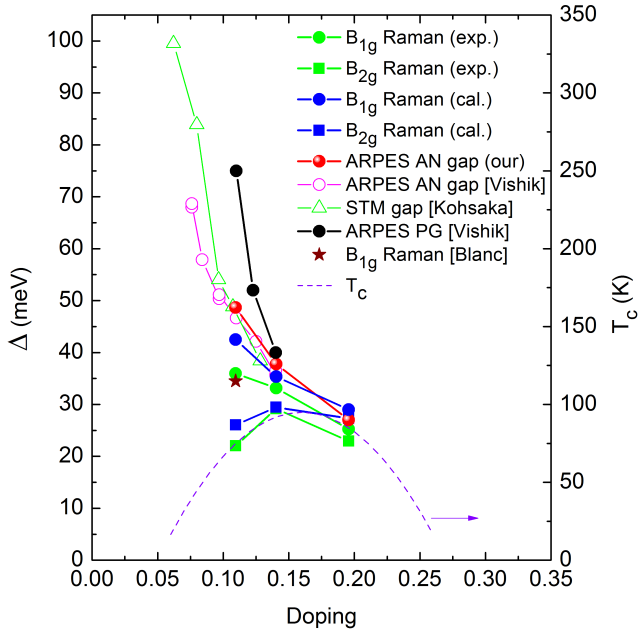

Figure 6.3: Peak energies obtained from calculations with Kubo formula for the whole Brillouin zone and with Shirley background subtraction in comparison to the experimental data from Raman, ARPES and STM measurements. AN denotes for the antinodal region.

data assuming proper intensity profiles of $A_{\mathbf{k},\omega}$ along the Fermi surface. This result indicates that B_{2g} Raman spectra can be understood by the superconducting gap profile obtained by ARPES, namely, the momentum independent gap slope. The intensity profiles of $A_{\mathbf{k},\omega}$ we used are simple and show doping dependence which is consistent with doping dependence of ARPES intensity along the Fermi surface observed in LSCO with fixed measurement conditions [167], and in contrast to the step-like function proposed by A. Sacuto [45].

We summarize our calculation results of peak energy in figure 6.3 in comparison to experimental Raman, ARPES and STM data. Firstly if we compare our experimental B_{1g} Raman and ARPES antinodal data, it clearly shows that the ARPES antinodal gap is higher than B_{1g} peak energy and the difference increases with underdoping. In the figure 6.3, we also plot data from other Raman, ARPES and STM measurements [45, 107, 168] in which ARPES measurement for underdoped samples used those from the same batch with ours. It shows that the ARPES antinodal gap and gap in STM increase very fast with underdoping, and definitely

show higher energy than Raman.

One can also notice that calculated B_{1g} peak energy follows ARPES antinodal gap and deviates from the experimental Raman data with underdoping. As discussed in the section 5.2.5, the intensity profile of $A_{\mathbf{k},\omega}$ cannot cause the shift of B_{1g} position. Therefore, this difference looks like intrinsic.

Since the calculated and experimental B_{1g} are consistent in the optimally doped region and the difference gets larger with underdoping, this difference is possibly caused by the pseudogap. Here we want to remind that the gap profile of the sample UD75K deviates from *d*-wave behavior in the antinodal region (figure 4.13) possibly because of the pseudogap.

In the figure we also plot pseudogap energy in ARPES data taken at 100 K [107]. If we compare the pseudogap energy to the other data, one can see that it increases rapidly with underdoping and it seems that the superconducting gap in ARPES is enhanced by the underlying-high-energy-pseudogap. Figure 6.3 may indicate that the effect of the pseudogap manifests differently in different measurement techniques and the manifestation is $ARPES > Raman$.

Chapter 7

Summary

To clarify the questions about origin of electronic Raman scattering spectra and the discrepancies between ERS and ARPES, also trying to get improvement more than previous calculations and explain the behaviors of ERS data, in this study

1) Bi2212 single crystals were grown by traveling solvent floating zone method, annealed in different conditions to get different doping levels from underdoped to overdoped, quality of single crystals were evaluated by magnetic succeptibility and the crystaline orientation was checked by X-ray Laue measurements,

2) ARPES and Raman measurements were carried out for the Bi2212 single crystals with different doping levels (UD75K, OP92K and OD85K) at well below T_c (at 10 K) for the same sample or the samples from the same batch, and measurements for both Raman and ARPES on the same sample is a critical point to compare quantitatively the ARPES and Raman data,

3) Calculations for B_{1g} and B_{2g} Raman spectra in the superconducting state were done using ARPES data and Kubo formula, as well as the kinetic theory. The electronic Raman spectra were well reproduced from ARPES data using Kubo formula, taking data over the whole Brillouin zone, with subtraction for Shirley background from raw ARPES EDC spectra, and with **k**-dependence of peak intensity of spectral function $A_{\mathbf{k},\omega}$. The tight-binding model was applied to fit band structure and get Raman vertices.

From the experimental data and the calculation results, some conclusions could be obtained as follows:

1) Raman and ARPES can be understood with the same gap profile. Nodal slope of gap profiles is independent for a wide range of doping levels. And this is different from the model proposed by A. Sacuto's group that the slope increases with underdoping.

The change of intensity ratio between the nodal region and the antinodal region of spectral function $A_{\mathbf{k},\omega}$ together with excitation on the whole BZ causes the doping dependence of the B_{2g} peak.

2) The superconducting gap in the antinodal region

- probed by ARPES is affected *strongly* by the pseudogap,
- probed by Raman using B_{1g} geometry is affected *moderately* by the pseudogap.

The effect of the pseudogap increases with underdoping, which manifests by the discrepancy between Raman and ARPES. Here in this viewpoint, the pseudogap competes with the superconducting gap. It also means that superconductivity and pseudogap coexist even at low temperature.

3) The peak-intensity profile of spectral functions $A_{\mathbf{k},\omega}$ is not only momentum dependent but also different in different doping levels. In the underdoped sample, spectral weight of $A_{\mathbf{k},\omega}$ is confined in the nodal region. And the antinodal region gets more spectral weight with doping and contributes to superconductivity.

4) More realistic B_{1g} and B_{2g} Raman spectra as in experimental data were obtained by using Kubo formula on whole-Brillouin-zone and Shirley-background subtraction calculation.

By applying the experimental ARPES EDC spectra for spectral functions, the momentum-dependent scattering rate was naturally included in the calculation, leading to the improvement of spectral shape in the calculated spectra.

Calculation on the whole Brillouin-zone means that electronic Raman scattering spectra are not only from excitation on the Fermi surface but also originated from the one around the Fermi surface.

Background subtraction has shown that Raman spectra are related to coherence peaks of single-particle spectral functions in the superconducting state.

Kubo formula calculations also reproduced two energy scales in B_{1g} and B_{2g} Raman spectra, which is caused definitely by different Raman vertices for different

geometries. Two energy scales have a tendency that they are close together in the overdoped region and separated more and more with underdoping.

5) Kinetic theory is not enough to describe the experimental B_{1g} and B_{2g} Raman spectra, specially in the underdoped and optimally doped regions where whether the calculated B_{1g} peak is too high or the calculated B_{2g} peak is too low in addition to simple spectra shapes.

We also see that tight-binding model could not describe fully the electronic band structure of cuprates specially in the antinodal region where the band dispersion is flat.

This calculation method should be examined for more doping levels and for other superconductors. Calculations for the B_{1g} and B_{2g} Raman spectra in the normal state could be concerned in the next step. For the normal state, certain assumption for band structure of unoccupied states is needed and this is one difficulty for a calculation in the normal state. In the present study, we concentrated on the superconducting state where a symmetry of particle-hole was assumed.

Publications

1) N. T. Hieu, K. Tanaka, T. Masui, S. Miyasaka and S. Tajima and T. Sasagawa, *Quantitative comparison between electronic Raman spectra and angle-resolved photoemission spectra in superconducting state of Bi2212*, Physics Procedia, **45**, 41-44 (2013).

2) N. T. Hieu, K. Tanaka, T. Masui, S. Miyasaka and S. Tajima and T. Sasagawa, *Reproduce electronic Raman scattering spectra in the superconducting state of Bi2212 from angle-resolved photoemission spectroscopy data* (to be submitted).

The conference presentations

1) 25^{th} International Symposium on Superconductivity, Tokyo - Japan, December 3-5, 2012 (ISS-2012). Program number: PCP-61, *Quantitative comparison between electronic Raman spectra and angle-resolved photoemission spectra in superconducting state of Bi2212*, N. T. Hieu, K. Tanaka, T. Masui, S. Miyasaka and S. Tajima and T. Sasagawa.

2) 68^{th} The Physical Society of Japan Meeting, Tokushima - Japan, September 25-28, 2013 (JPS-2013). Program number: 26aKQ-9, *Discrepancy between electronic Raman scattering and angle-resolved photoemission spectroscopy in the superconducting state of underdoped Bi2212*, N. T. Hieu, K. Tanaka, T. Masui, S. Miyasaka and S. Tajima and T. Sasagawa.

Acknowledgements

It is my great pleasure to express my gratitude to the following people for their help in my study as well as my life here in Japan.

First of all, I would like to express my sincere gratitude to my supervisor Prof. Setsuko TAJIMA for giving me a chance to study abroad in a field I like, for all helpful discussions with difficult questions, excellent comments and advice throughout my study, for continuous encouragement and taking care my life.

I have to express my great thanks to Ass. Prof. Kiyohisa TANAKA for taking care my study as a senior researcher, teaching a lot of things and giving me advice with his kind enthusiasm. I would like to express my especial thanks to Associate Prof. Shigeki MIYASAKA, Ass. Prof. Takahiko MASUI for all their supports and discussions.

I would like to thank Associate Prof. Toshifumi TANIGUCHI who allowed me to grow Bi2212 single crystals on his floating zone system. I would like to thank Prof. Shik SHIN and especially Dr. Yukiaki ISHIDA for their enthusiastic supports in ARPES measurements.

I am particularly indebted to Prof. T. P. DEVEREAUX for his kind discussion about my calculation.

I wish to thank professors in IPC and Department of Physics: Prof. Hideaki TAKABE, Dr. Baiotti LUCA, Prof. Yasuo NOZUE for their lectures and encouragement. I would like to express my thanks to Ms. Yoshiko ISHIMOTO, Ms. Hiroko OTOMO, Ms. Yoshiko YAMADA and every staffs in Graduate School of Science for dealing with a lot of business stuff.

I thank all my Japanese and international friends in TAJIMA lab: Mr. Taira MIYAKE, Mr. Ryuichiro FUKUTA, Mr. Akira TAKEMORI, Mr. Kazuhiro HENMI, Mr. Tatsuya KOBAYASHI , Mr. Naoya SASAKI, Mr. Tohru ADACHI,

Miss. Ece UYKUR, Mr. Kwing To LAI, Mr. Weiwu LI,... especially Mr. Naoki MURAI, as well as Vietnamese friends for their help and encouragement.

I would like to thank all the journals and people who allowed me to use their published figures.

Finally, I would like to send my sincere deep thanks with lot of respect and gratitude to my family and my relatives for their continuous support and encouragement all over the years.

OSAKA, April 2014
Nguyen Trung Hieu

Bibliography

[1] J. Bardeen, L. N. Cooper, and J.R.Schrieffer, Phys. Rev. **108**, 1175 (1957).

[2] J. G. Bednorz and K. Müller, Z. Phys. B **64**, 189 (1986).

[3] W. L. McMillan, Phys. Rev. **167**, 331 (1968).

[4] N. Plakida, *High-Temperature Cuprate Superconductors* (Springer, 2010).

[5] M. K. Wu, J. R. Ashburn, C. J. Torng, P. H. Hor, R. L. Meng, L. Gao, Z. J. Huang, Y. Q. Wang, and C. W. Chu, Phys. Rev. Lett. **58**, 908 (1987).

[6] A. Schilling, M. Cantoni, J. D. Guo, and H. R. Ott, Nature **363**, 56 (1993).

[7] P. Dai, B. C. Chakoumakos, G. F. Sun, K. W. Wong, Y. Xin, and D. F. Lu, Physica C **243**, 201 (1995).

[8] C. W. Chu, L. Gao, F. Chen, Z. Huang, R. Meng, and Y. Y. Xue, Nature **365**, 323 (1993).

[9] L. Gao, Y. Y. Xue, F. Chen, Q. Xiong, R. L. Meng, D. Ramirez, C. W. Chu, J. H. Eggert, and H. K. Mao, Phys. Rev. B **50**, 4260 (1994).

[10] C. E. Gough, M. S. Colclough, E. M. Forgan, R. G. Jordan, M. Keene, C. M. Muirhead, A. I. M. Rae, N. Thomas, J. S. Abell, and S. Sutton, Nature **326**, 855 (1987).

[11] Ø. Fischer, M. Kugler, I. Maggio-Aprile, C. Berthod, and C. Renner, Rev. Mod. Phys. **79**, 353 (2007).

[12] Y. Kamihara, H. Hiramatsu, M. Hirano, R. Kawamura, H. Yanagi, T. Kamiya, and H. Hosono, J. Am. Chem. Soc. **128**, 10012 (2006).

[13] Y. Kamihara, T. Watanabe, M. Hirano, and H. Hosono, J. Am. Chem. Soc. **130**, 3296 (2008).

[14] C. Wang, L. Li, S. Chi, Z. Zhu, Z. Ren, Y. Li, Y. Wang, X. Lin, Y. Luo, S. Jiang, X. Xu, G. Cao, and Z. Xu, Europhys. Lett. **83**, 67006 (2008).

[15] G. Wu, Y. L. Xie, H. Chen, M. Zhong, R. H. Liu, B. C. Shi, Q. J. Li, X. F. Wang, T. Wu, Y. J. Yan, J. J. Ying, and X. H. Chen, J. Phys.: Condens. Matter **21**, 142203 (2009).

[16] Z.-A. Ren, G.-C. Che, X.-L. Dong, J. Yang, W. Lu, W. Yi, X.-L. Shen, Z.-C. Li, L.-L. Sun, F. Zhou, and Z.-X. Zhao, Europhys. Lett. **83**, 17002 (2008).

[17] M. Fujioka, S. J. Denholme, T. Ozaki, H. Okazaki, K. Deguchi, S. Demura, H. Hara, T. Watanabe, H. Takeya, T. Yamaguchi, H. Kumakura, and Y. Takano, Supercond. Sci. Technol. **26**, 085023 (2013).

[18] S. Shimizu, S. Iwai, S. Tabata, H. Mukuda, Y. Kitaoka, P. M. Shirage, H. Kito, and A. Iyo, Phys. Rev. B **83**, 144523 (2011).

[19] D. Estève, J. M. Martinis, C. Urbina1, M. H. Devoret, G. Collin, P. Monod, M. Ribault, and A. Revcolevschi, Europhys. Lett. **3**, 1237 (1987).

[20] N. Bergeal1, J. Lesueur, M. Aprili, G. Faini, J. P. Contour, and B. Leridon, Nat. Phys. **4**, 608 (2008).

[21] M. R. Presland, J. L. Tallon, R. G. Buckley, R. S. Liu, and N. E. Flower, Physica C **176**, 95 (1991).

[22] A. Mourachkine, Supercond. Sci. Technol. **17**, 721 (2004).

[23] X.-J. Chen, B. Liang, C. Ulrich, C.-T. Lin, V. V. Struzhkin, Z. Wu, R. J. Hemley, H. Mao, and H.-Q. Lin, Phys. Rev. B **76**, 140502 (2007).

[24] J. Lee, K. Fujita, K. McElroy, J. A. Slezak, M. Wang, Y. Aiura, H. Bando, M. Ishikado, T. Masui, J. X. Zhu, A. V. Balatsky, H. Eisaki, S. Uchida, and J. C. Davis, Nature **442**, 546 (2006).

[25] J. P. Franck, Physca C **282–287**, 198 (1997).

[26] D. J. Pringle, G. V. M. Williams, and J. L. Tallon, Phys. Rev. B **62**, 12527 (2000).

[27] J. F. Douglas, H. Iwasawa, Z. Sun, A. V. Fedorov, M. Ishikado, T. Saitoh, H. Eisaki, H. Bando, T. Iwase, A. Ino, M. Arita, K. Shimada, H. Namatame, M. Taniguchi, T. Masui, S. Tajima, K. Fujita, S. Uchida, Y. Aiura, and D. S. Dessau, Nature **446**, E5 (2007).

[28] K. C. Hewitt, N. Wang, J. Irwin, D. M. Pooke, A. E. Pantoja, and H. J. Trodahl, Phys. Rev. B **60**, R9943 (1999).

[29] R. Khasanov, A. Shengelaya, E. Morenzoni, M. Angst, K. Conder, I. Savic, D. Lampakis, E. Liarokapis, A. Tatsi, and H. Keller, Phys. Rev. B **68**, 220506 (2003).

[30] D. Zech, H. Keller, K. Conder, E. Kaldis, E. Liarokapis, N. Poulakis, and K. A. Müller, Nature **371**, 681 (1994).

[31] A. A. Martin and M. J. G. Lee, Physica C **254**, 222 (1995).

[32] C. Kittel, *Introduction to Solid State Physics*, 7th ed. (John Wiley & Sons, 1996).

[33] M. Li, C. J. van der Beek, M. Konczykowski, A. A. Menovsky, and P. H. Kes, Phys. Rev. B **66**, 024502 (2002).

[34] R. Kleiner, F. Steinmeyer, G. Kunkel, and P. Müller, Phys. Rev. Lett. **68**, 2394 (1992).

[35] Y. J. Uemura, G. M. Luke, B. J. Sternlieb, J. H. Brewer, J. F. Carolan, W. N. Hardy, R. Kadono, J. R. Kempton, R. F. Kiefl, S. R. Kreitzman, P. Mulhern, T. M. Riseman, D. L. Williams, B. X. Yang, S. Uchida, H. Takagi, J. Gopalakrishnan, A. W. Sleight, M. A. Subramanian, C. L. Chien, M. Z. Cieplak, G. Xiao, V. Y. Lee, B. W. Statt, C. E. Stronach, W. J. Kossler, and X. H. Yu, Phys. Rev. Lett. **62**, 2317 (1989).

[36] Y. J. Uemura, L. P. Le, G. M. Luke, B. J. Sternlieb, W. D. Wu, J. H. Brewer, T. M. Riseman, C. L. Seaman, M. B. M. andM. Ishikawa, D. G. Hinks, J. D. Jorgensen, G. Saito, and H. Yamochi, Phys. Rev. Lett. **66**, 2665 (1991).

[37] N. D. Mathur, F. M. Grosche, S. R. Julian1, I. R. Walker, D. M. Freye, R. K. W. Haselwimmer, and G. G. Lonzarich, Nature **394**, 39 (1998).

[38] D. G. Hinks, D. R. Richards, B. Dabrowski, D. T. Marx, and A. W. Mitchell, Nature **335**, 419 (1988).

[39] S. Tajima, T. Nakahashi, S. Uchida, and S. Tanaka, Physica C **156**, 90 (1988).

[40] S. Tajima, Y. Fudamoto, T. Kakeshita, B. Gorshunov, V. Zelezny, K. M. Kojima, M. Dressel, and S. Uchida, Phys. Rev. B **71**, 094508 (2005).

[41] Z.-X. Shen, D. S. Dessau, B. O. Wells, D. M. King, W. E. Spicer, A. J. Arko, D. Marshall, L. W. Lombardo, A. Kapitulnik, P. Dickinson, S. Doniach, J. DiCarlo, T. Loeser, and C. H. Park, Phys. Rev. Lett. **70**, 1553 (1993).

[42] H. Ding, M. R. Norman, J. C. Campuzano, M. Randeria, A. F. Bellman, T. Yokoya, T. Takahashi, T. Mochiku, and K. Kadowaki, Phys. Rev. B **54**, R9678 (1996).

[43] T. P. Devereaux, D. Einzel, B. Stadlober, R. Hackl, D. H. Leach, and J. J. Neumeier, Phys. Rev. Lett. **72**, 396 (1994).

[44] T. P. Devereaux and D. Einzel, Phys. Rev. B **51**, 16336 (1995).

[45] S. Blanc, Y. Gallais, M. Cazayous, M. A. Measson, A. Sacuto, A. Georges, J. S. Wen, Z. J. Xu, G. D. Gu, and D. Colson, Phys. Rev. B **82**, 144516 (2010).

[46] R. Khasanov, S. Strassle, D. D. Castro, T. Masui, S. Miyasaka, S. Tajima, A. Bussmann-Holder, and H. Keller, Phys. Rev. Lett. **99**, 237601 (2007).

[47] M. Limonov, T. Masui, H. Uchiyama, S. Lee, S. Tajima, and A. Yamanaka, Physica C **392–396**, 53 (2003).

[48] K. Nishikawa, T. Masui, S. Tajima, H. Eisaki, H. Kito, and A. Iyo, J. Phys. Chem. Solids **69**, 3074 (2008).

[49] T. Hiramachi, T. Masui, and S. Tajima, Physica C **463–465**, 89 (2007).

[50] M. Bakr, A. P. Schnyder, L. Klam, D. Manske, C. T. Lin, B. Keimer, M. Cardona, and C. Ulrich, Phys. Rev. B **80**, 064505 (2009).

[51] K. Tanaka, W. S. Lee, D. H. Lu, A. Fujimori, T. Fujii, Risdiana, I. Terasaki, D. J. Scalapino, T. P. Devereaux, Z. Hussain, and Z.-X. Shen, Science **314**, 1910 (2006).

[52] W. S. Lee, I. Vishik, K. Tanaka, D.H.Lu, T. Sasagawa, N. Nagaosa, T. Devereaux, Z. Hussain, and Z.-X. Shen, Nature **450**, 81 (2007).

[53] I. M. Vishik, W. S. Lee, R.-H. He, M. Hashimoto, Z. Hussain, T. P. Devereaux, and Z.-X. Shen, New J. Phys. **12**, 105008 (2010).

[54] H. Maeda, Y. Tanaka, M. Fukutomi, and T. Asano, Jpn. J. Appl. Phys. **27**, L209 (1988).

[55] S. Ideta, *Electronic Structure and its Relationship to Superconductivity in Iron-based and Cuprate High-*T_c *Superconductors Studied by Angle-resolved Photoemission Spectroscopy*, PhD thesis, University of Tokyo, 2011.

[56] B. Liang and C. T. Lin, J. Crys. Growth **237–239**, 756 (2002).

[57] G. D. Gu, K. Takamuku, N. Koshizuka, and S. Tanaka, J. Crys. Growth **130**, 325 (1993).

[58] S. Sugai, Y. Takayanagi, N. Hayamizu, and T. Muroi, J. Phys.: Conf. Ser. **108**, 012022 (2008).

[59] T. Dahm, V. Hinkov, S. V. Borisenko, A. A. Kordyuk, V. B. Zabolotnyy, J. Fink, B. Bchner, D. J. Scalapino, W. Hanke, and B. Keimer, Nat. Phys. **5**, 217 (2009).

[60] O. V. Misochko, Phys. Usp. **46**, 373 (2003).

[61] Y. Sidis, S. Pailhès, B. Keimer, P. Bourges, C. Ulrich, and L. P. Regnault, Phys. Stat. Sol. (b) **241**, 1204 (2004).

[62] Y. Ando, S. Komiya, K. Segawa, S. Ono, and Y. Kurita, Phys. Rev. Lett. **93**, 267001 (2004).

[63] X. H. Chen, M. Yu, K. Q. Ruan, S. Y. Li, Z. Gui, G. C. Zhang, and L. Z. Cao, Phys. Rev. B **58**, 14219 (1998).

[64] T. Ito, H. Takagi, S. Ishibashi, T. Ido, and S. Uchida, Nature **350**, 596 (1991).

[65] T. Ito, K. Takenaka, and S. Uchida, Phys. Rev. Lett. **70**, 3995 (1993).

[66] M. A. Quijada, D. B. Tanner, R. J. Kelley, and M. Onellion, Physica C **235–240**, 1123 (1994).

[67] Y. Kotaka, T. Kimura, H. Ikuta, J. Shimoyama, K. Kitazawa, K. Yamafuji, K. Kishio, and D. Pooke, Physica C **235–240**, 1529 (1994).

[68] T. Watanabe, T. Fujii, and A. Matsuda, Phys. Rev. Lett. **79**, 2113 (1997).

[69] Y. Ando, K. Segawa, S. Komiya, and A. N. Lavrov, Phys. Rev. Lett. **88**, 137005 (2002).

[70] S. Komiya, Y. Ando, X. F. Sun, and A. N. Lavrov, Phys. Rev. B **65**, 214535 (2002).

[71] T. Motohashi, Y. Nakayama, T. Fujita, K. Kitazawa, J. Shimoyama, and K. Kishio, Phys. Rev. B **59**, 14080 (1999).

[72] S. Ono and Y. Ando, Phys. Rev. B **67**, 104512 (2003).

[73] S. Tajima, G. Gu, S. Miyamoto, A. Odagawa, and N. Koshizuka, Phys. Rev. B **48**, 16164 (1993).

[74] M. A. Quijada, D. B. Tanner, R. J. Kelley, M. Onellion, H. Berger, and G. Margaritondo, Phys. Rev. B **60**, 14917 (1999).

[75] J. J. Tu, C. C. Homes, G. D. Gu, D. N. Basov, and M. Strongin, Phys. Rev. B **66**, 144514 (2002).

[76] N. E. Hussey, J. R. Cooper, J. M. Wheatley, I. R. Fisher, A. Carrington, A. P. Mackenzie, C. T. Lin, and O. Milat, Phys. Rev. Lett. **76**, 122 (1996).

[77] A. Damascelli, Z. Hussain, and Z. X. Shen, Rev. Mod. Phys. **75**, 473 (2003).

[78] P. Fulde, *Electron correlations in molecules and solids*, 3rd ed. (Springer, 1995).

[79] E. Dagotto, Rev. Mod. Phys. **66**, 763 (1994).

[80] F. C. Zhang and T. M. Rice, Phys. Rev. B **37**, 3759 (1988).

[81] H. Eskes and G. A. Sawatzky, Phys. Rev. B **44**, 9656 (1991).

[82] T. Timusk and B. Statt, Rep. Prog. Phys. **62**, 61 (1999).

[83] M. R. Norman, D. Pines, and C. Kallin, Advances in Physics **54**, 715 (2005).

[84] W. W. W. Jr., R. E. Walstedt, G. F. Brennert, R. J. Cava, R. Tycko, R. F. Bell, and G. Dabbagh, Phys. Rev. Lett. **62**, 1193 (1989).

[85] H. Alloul, T. Ohno, and P. Mendels, Phys. Rev. Lett. **63**, 1700 (1989).

[86] J. Hwang, T. Timusk, and G. D. Gu, J. Phys.: Condens. Matter **19**, 125208 (2007).

[87] C. Renner, B. Revaz, J.-Y. Genoud, K. Kadowaki, and Ø. Fischer, Phys. Rev. Lett. **80**, 149 (1998).

[88] A. Matsuda, S. Sugita, and T. Watanabe, Phys. Rev. B **60**, 1377 (1999).

[89] M. Kugler, Ø. Fischer, C. Renner, S. Ono, and Y. Ando, Phys. Rev. Lett. **86**, 4911 (2001).

[90] M. R. Norman, H. Ding, M. Randeria, J. C. Campuzano, T. Yokoya, T. Takeuchik, T. Takahashi, T. Mochiku, K. Kadowaki, P. Guptasarma, and D. G. Hinks, Nature **392**, 157 (1998).

[91] H. Ding, J. C. Campuzano, M. R. Norman, M. Randeria, T. Yokoya, T. Takahashi, T. Takeuchi, T. Mochiku, K. Kadowaki, P. Guptasarma, and D. G. Hinks, J. Phys. Chem. Solids **59**, 1888 (1998).

[92] R. Nemetschek, M. Opel, C. Hoffmann, P. F. Müller, R. Hackl, H. Berger, L. Forró, A. Erb, and E. Walker, Phys. Rev. Lett. **78**, 4837 (1997).

[93] N. Momono, R. M. Dipasupil, S. Manda, T. Nagata, M. Oda, M. Ido, and A. Sakai, Physica C **341–348**, 909 (2000).

[94] M. Opel, R. Nemetschek, C. Hoffmann, R. Philipp, P. F. Müller, R. Hackl, I. Tüttő, A. Erb, B. Revaz, E. Walker, H. Berger, and L. Forró, Phys. Rev. B **61**, 9752 (2000).

[95] Y. Gallais, A. Sacuto, T. P. Devereaux, and D. Colson, Phys. Rev. B **71**, 012506 (2005).

[96] G. Blumberg, M. Kang, M. V. Klein, K. Kadowaki, and C. Kendziora, Science **278**, 1427 (1997).

[97] L. H. Machtoub, L. Robinson, J. Shimoyama, T. Suemoto, and K. Kishio, J. Raman Spectrosc. **32**, 937 (2001).

[98] W. Guyard, M. L. Tacon, M. Cazayous, A. Sacuto, A. Georges, D. Colson, and A. Forget, Phys. Rev. B **77**, 024524 (2008).

[99] S. Sakai, S. Blanc, M. Civelli, Y. Gallais, M. Cazayous, M.-A. Méasson, J. S. Wen, Z. J. Xu, G. D. Gu, G. Sangiovanni, Y. Motome, K. Held, A. Sacuto, A. Georges, and M. Imada, Phys. Rev. Lett. **111**, 107001 (2013).

[100] A. Sacuto, Y. Gallais, M. Cazayous, S. Blanc, M.-A. Méassona, J. Wen, Z. Xu, G. Gu, and D. Colson, C. R. Physique **12**, 480 (2011).

[101] A. Sacuto, S. Benhabib, Y. Gallais, S. Blanc, M. Cazayous, M.-A. Méasson, J. S. Wen, Z. J. Xu, and G. D. Gu, J. Phys.: Conf. Ser. **449**, 012011 (2013).

[102] A. J. Drew, C. Niedermayer, P. J. Baker, F. L. Pratt, S. J. Blundell, T. Lancaster, R. H. Liu, G. Wu, X. H. Chen, I. Watanabe, V. K. Malik, A. Dubroka, M. Rössle, K. W. Kim, C. Baines, and C. Bernhard, Nature Materials **8**, 310 (2009).

[103] Z. Shermadini, A. Krzton-Maziopa, M. Bendele, R. Khasanov, H. Luetkens, K. Conder, E. Pomjakushina, S. Weyeneth, V. Pomjakushin, O. Bossen, and A. Amato, Phys. Rev. Lett. **106**, 117602 (2011).

[104] S. Uchida, Physica C **357–360**, 25 (2001).

[105] A. Mann, Nature **475**, 280 (2011).

[106] A. V. Chubukov, T. P. Devereaux, and M. V. Klein, Phys. Rev. B **73**, 094512 (2006).

[107] I. M. Vishik, M. Hashimoto, R.-H. He, W.-S. Lee, F. Schmitt, D. Lu, R. G. Moore, C. Zhang, W. Meevasanaf, T. Sasagawa, S. Uchida, K. Fujita, S. Ishida, M. Ishikado, Y. Yoshida, H. Eisaki, Z. Hussain, T. P. Devereaux, and Z.-X. Shen, Proc. Natl. Acad. Sci. U.S.A. **109**, 18332 (2012).

[108] M. L. Tacon, A.Sacuto, A. Georges, G. Kotliar, Y. Gallais, D. Colson, and A. Forget, Nat. Phys. **2**, 537 (2006).

[109] M. Oda, R. M. Dipasupil, N. Momono, and M. Ido, J. Phys. Soc. Jpn. **69**, 983 (2000).

[110] W. Prestel, F. Venturini, B. Muschler, I. Tüttő, R. Hackl, M. Lambacher, A. Erb, S. Komiya, S. Ono, Y. Ando, D. Inosov, V. B. Zabolotnyy, and S. Borisenko, Eur. Phys. J. Special Topics **188**, 163 (2010).

[111] D. S. Inosov, S. V. Borisenko, I. Eremin, A. A. Kordyuk, V. B. Zabolotnyy, J. Geck, A. Koitzsch, J. Fink, M. K. B. Büchner, H. Berger, and R. Follath, Phys. Rev. B **75**, 172505 (2007).

[112] T. Valla, A. V. Fedorov, P. D. Johnson, B. O. Wells, S. L. Hulbert, Q. Li, G. D. Gu, and N. Koshizuka, Science **285**, 2110 (1999).

[113] Figure from the website of Shen laboratory, `http://arpes.stanford.edu/facilities_ssrl.html`.

[114] D. S. Dessau, Z. X. Shen, D. M. King, D. S. Marshall, L. W. Lombardo, P. H. Dickinson, A. G. Loeser, J. DiCarlo, C.-H. Park, A. Kapitulnik, and W. E. Spice, Phys. Rev. Lett. **71**, 2781 (1993).

[115] A. G. Loeser, Z.-X. Shen, M. C. Schabel, C. Kim, M. Zhang, , A. Kapitulnik, and P. Fournier, Phys. Rev. B **56**, 14185 (1997).

[116] A. Kanigel, M. R. Norman, M. Randeria, U. Chatterjee, S. Souma, A. Kaminski, H. M. Fretwell, S. Rosenkranz, M. Shi, T. Sato, T. Takahashi, Z. Z. Li, H. Raffy, K. Kadowaki, D. Hinks, L. Ozyuzer, and J. C. Campuzano, Nat. Phys. **2**, 447 (2006).

[117] H.-B. Yang, J. D. Rameau, Z.-H. Pan, G. D. Gu, P. D. Johnson, H. Claus, D. G. Hinks, and T. E. Kidd, Phys. Rev. Lett. **107**, 047003 (2011).

[118] D. L. Feng, N. P. Armitage, D. H. Lu, A. Damascelli, J. P. Hu, P. Bogdanov, A. Lanzara, F. Ronning, K. M. Shen, H. Eisaki, C. Kim, Z.-X. Shen, J. i. Shimoyama, and K. Kishio, Phys. Rev. Lett. **86**, 5550 (2001).

[119] A. A. Kordyuk, S. V. Borisenko, T. K. Kim, K. A. Nenkov, M. Knupfer, J. Fink, M. S. Golden, H. Berger, and R. Follath, Phys. Rev. Lett. **89**, 077003 (2002).

[120] J. D. Koralek, J. F. Douglas, N. C. Plumb, Z. Sun, A. V. Fedorov, M. M. Murnane, H. C. Kapteyn, S. T. Cundiff, Y. Aiura, K. Oka, H. Eisaki, and D. S. Dessau, Phys. Rev. Lett. **96**, 017005 (2006).

[121] D. A. Shirley, Phys. Rev. B **5**, 4709 (1972).

[122] L. Z. Liu, R. O. Anderson, and J. W. Allen, J. Phys. Chem. Solids **52**, 1473 (1991).

[123] M. R. Norman, H. Ding, H. Fretwell, M. Randeria, M. Randeria, and J. C. Campuzano, Phys. Rev. B **60**, 7585 (1999).

[124] M. R. Norman, M. Randeria, H. Ding, and J. C. Campuzano, Phys. Rev. B **59**, 11191 (1999).

[125] D. L. Feng, D.H.Lu, K. M. Shen, C. Kim, H. Eisaki, A. Damascelli, R. Yoshizaki, J. i. Shimoyama, K. Kishio, G. D. Gu, S. Oh, A. Andrus, J. O'Donnell, J. N. Eckstein, and Z.-X. Shen, Science **289**, 277 (2000).

[126] A. Kaminski, S. Rosenkranz, H. M. Fretwell, J. Mesot, M. Randeria, J. C. Campuzano, M. R. Norman, Z. Z. Li, H. Raffy, T. Sato, T. Takahashi, and K. Kadowaki, Phys. Rev. B **69**, 212509 (2004).

[127] G.-H. Gweon, B. S. Shastry, and G. D. Gu, Phys. Rev. Lett. **107**, 056404 (2011).

[128] H. J. Im, T. Ito, H.-D. Kim, S. Kimura, K. E. Lee, J. B. Hong, Y. S. Kwon, A. Yasui, and H. Yamagami, Phys. Rev. Lett. **100**, 176402 (2008).

[129] H. Ding, J. C. Campuzano, A. F. Bellman, T. Yokoya, M. R. Norman, M. Randeria, T. Takahashi, H. K. Yoshida, T. Mochiku, K. Kadowaki, and G. Jennings, Phys. Rev. Lett. **74**, 2784 (1995).

[130] T. P. Devereaux and R. Hackl, Rev. Mod. Phys. **79**, 175 (2007).

[131] M. Cardona, Physica C **317–318**, 30 (1999).

[132] M. V. Klein, M.Rübhausen, D. Budelmann, B. Schulz, P. Guptasarma, M. S. Williamsen, R. Liang, D. A. Bonn, and W. N. Hardy, J. Phys. Chem. Solids **67**, 298 (2006).

[133] O. V. Misochko and E. Y. Sherman, J. Phys.: Condens. Matter **12**, 9095 (2000).

[134] M. Limonov, S. Lee, S. Tajima, and A. Yamanaka, Phys. Rev. B **66**, 054509 (2002).

[135] Y. Gallais, A. Sacuto, and D. Colson, Physica C **408–410**, 785 (2004).

[136] M. L. Tacon, A. Sacuto, and D. Colson, Phys. Rev. B **71**, 100504 (2005).

[137] M. Kang, G. Blumberg, M. V. Klein, and N. N. Kolesnikov, Phys. Rev. Lett. **77**, 4434 (1996).

[138] M. L. Tacon, A. Sacuto, and D. Colson, Physica C **460–462**, 358 (2007).

[139] M. Rübhausen, O. A. Hammerstein, A. Bock, U. Merkt, C. T. Rieck, P. Guptasarma, D. G. Hinks, and M. V. Klein, Phys. Rev. Lett. **82**, 5349 (1999).

[140] G. Blumberg, A. Koitzsch, A. Gozar, B. S. Dennis, C. A. Kendziora, P. Fournier, and R. L. Greene, Phys. Rev. Lett. **88**, 107002 (2002).

[141] S. Sugai and T. Hosokawa, Phys. Rev. Lett. **85**, 1112 (2000).

[142] S. Sugai, H. Suzuki, Y. Takayanagi, T. Hosokawa, and N. Hayamizu, Phys. Rev. B **68**, 184504 (2003).

[143] F. Venturini, M. Opel, R. Hackl, H. Berger, L. Forró, and B. Revaz, J. Phys. Chem. Solids **63**, 2345 (2002).

[144] F. Venturini, M. Opel, T. P. Devereaux, J. K. Freericks, I. Tüttő, B. Revaz, E. Walker, H. Berger, L. Forró, and R. Hackl, Phys. Rev. Lett. **89**, 107003 (2002).

[145] N. Munnikes, B. Muschler, F. Venturini, L. Tassini, W. Prestel, S. Ono, Y. Ando, D. C. Peets, W. N. Hardy, R. Liang, D. A. Bonn, A. Damascelli, H. Eisaki, M. Greven, A. Erb, and R. Hackl, Phys. Rev. B **84**, 144523 (2011).

[146] X. K. Chen, J. C. Irwin, H. J. Trodahl, M. Okuya, T. Kimura, and K. Kishio, Physica C **295**, 80 (1998).

[147] S. Hüfner, M. A. Hossain, A. Damascelli, and G. A. Sawatzky, Rep. Prog. Phys. **71**, 062501 (2008).

[148] S. D. Almeida-Didry, F. Giovannelli, I. Monot-Laffez, Y. Sidis, P. Bourges, F. Schoenstein, S. Pruvost, and B. Pignon, J. Crys. Growth **312**, 466 (2010).

[149] J. S. Wen, Z. J. Xu, G. Y. Xu, M. Hucker, J. M. Tranquada, and G. D. Gu, J. Cryst. Growth **310**, 1401 (2008).

[150] I. Chong, Z. Hiroi, M. Izumi, J. Shimoyama, Y. Nakayama, K. Kishio, T. Terashima, Y. Bando, and M. Takano, Science **276**, 770 (1997).

[151] P. V. Bogdanov, A. Lanzara, X. J. Zhou, S. A. Kellar, D. L. Feng, E. D. Lu, H. Eisaki, J.-I. Shimoyama, K. Kishio, Z. Hussain, and Z. X. Shen, Phys. Rev. B **64**, 180505 (2001).

[152] S. V. Borisenko, A. A. Kordyuk, T. K. Kim, A. Koitzsch, M. Knupfer, J. Fink, M. S. Golden, M. Eschrig, H. Berger, and R. Follath, Phys. Rev. Lett. **90**, 207001 (2003).

[153] H. Eisaki, N. Kaneko, D. L. Feng, A. Damascelli, P. K. Mang, K. M. Shen, Z.-X. Shen, and M. Greven, Phys. Rev. B **69**, 064512 (2004).

[154] H. Sozeri, L. Dorosinskii, and U. Topal, Physica C **434**, 95 (2006).

[155] J. D. Rameau, Z.-H. Pan, H.-B. Yang, G. D. Gu, and P. D. Johnson, Phys. Rev. B **84**, 180511 (2011).

[156] T. P. Devereaux, Phys. Rev. Lett. **74**, 4313 (1995).

[157] M. V. Klein and S. B. Dierker, Phys. Rev. B **29**, 4976 (1984).

[158] D. Branch and J. P. Carbotte, J. Supercond.: Inc. Nov. Magn. **13**, 535 (2000).

[159] T. P. Devereaux and A. P. Kampf, Int. J. Mod. Phys. B **11**, 2093 (1997).

[160] T. P. Devereaux and A. P. Kampf, Phys. Rev. B **59**, 6411 (1999).

[161] D. Manske, C. T. Rieck, R. D. Sharma, A. Bock, and D. Fay, Phys. Rev. B **56**, R2940 (1997).

[162] A. G. Loeser, Z.-X. Shen, D. S. Dessau, D. S. Marshall, C. H. Park, P. Fournier, and A. Kapitulnik, Science **273**, 325 (1996).

[163] A. V. Fedorov, T. Valla, P. D. Johnson, Q. Li, G. D. Gu, and N. Koshizuka, Phys. Rev. Lett. **82**, 2179 (1999).

[164] F. Venturini, U. Michelucci, T. P. Devereaux, , and A. P. Kampf, Phys. Rev. B **62**, 15204 (2000).

[165] T. Kondo, R. Khasanov, T. Takeuchi, J. Schmalian, and A. Kaminski, Nature **457**, 296 (2009).

[166] D. C. Peets, J. D. F. Mottershead, B. Wu, I. S. Elfimov, R. Liang, W. N. Hardy, D. A. Bonn, M. Raudsepp, N. J. C. Ingle, and A. Damascelli, New J. Phys. **9**, 28 (2007).

[167] T. Yoshida, X. J. Zhou, T. Sasagawa, W. L. Yang, P. Bogdanov, A. Lanzara, Z. Hussain, T. Mizokawa, A. Fujimori, H. Eisaki, Z.-X. Shen, T. Kakeshita, and S. Uchida, Phys. Rev. Lett. **91**, 027001 (2003).

[168] Y. Kohsaka, C. Taylor, P. Wahl, A. Schmidt, J. Lee, K. Fujita, J. W. Alldredge, K. McElroy, J. Lee, H. Eisaki, S. Uchida, D.-H. Lee, and J. C. Davis, Nature **454**, 1072 (2008).

[169] R. Liu, M. V. Klein, P. D. Han, and D. A. Payne, Phys. Rev. B **45**, 7392 (1992).

Appendix A

Maxtrix element

Semi-classical theory view on matrix element. Matrix element indicates interaction between electromagnetic waves and electrons. In non-relativistic system the Shrödinger equation for an electron is

$$H_0\psi_0 = \left(\frac{p^2}{2m} + V_0\right)\psi_0 = E\psi_0. \tag{A.1}$$

Fields of an electromagnetic wave in Maxwell equations are

$$\mathbf{B} = \nabla \times \mathbf{A}, \tag{A.2}$$

$$E = -\frac{1}{c}\frac{\partial \mathbf{A}}{\partial t}, \tag{A.3}$$

with $\Phi = 0$ and $\nabla \cdot \mathbf{A} = 0$, where Φ and $\mathbf{A}$ are the scalar potential and the vector potential, respectively.

The electron interacts with the wave and its momentum is changed by adding the vector potential. The Hamiltonian becomes

$$\begin{aligned} H &= \left(\frac{1}{2m}(\mathbf{p} + \frac{e}{c}\mathbf{A})^2 + V_0\right) && \text{(A.4)} \\ &= \frac{p^2}{2m} + \frac{e}{2mc}\mathbf{A}\mathbf{p} + \frac{e}{2mc}\mathbf{p}\mathbf{A} + \frac{e^2}{2mc^2}\mathbf{A}^2 + V_0 && \text{(A.5)} \\ &= \frac{p^2}{2m} + \frac{e}{mc}\mathbf{A}\mathbf{p} + V_0, && \text{(A.6)} \end{aligned}$$

because of commutator relation $[\mathbf{p}, \mathbf{A}] = -i\hbar\nabla \cdot \mathbf{A} = 0$ and we ignore the second order term.

Therefore the perturbation of the field of the wave

$$\langle \phi_f^{\mathbf{k}} | H_{int} | \phi_i^{\mathbf{k}} \rangle = \frac{e}{2mc} \langle \phi_f^{\mathbf{k}} | \mathbf{A} \cdot \mathbf{p} | \phi_i^{\mathbf{k}} \rangle. \tag{A.7}$$

For a plane wave, we have

$$\mathbf{A}(\omega, t) = \boldsymbol{\varepsilon} \exp i(\omega t - \mathbf{q}.\mathbf{r}), \tag{A.8}$$

where $\boldsymbol{\varepsilon}$ is polarization vector, $\mathbf{q}$ is momemtum of photon. And with a ultra violet wave, the exponent is ≈ 1 (unchange) in the atom scale. We also have $\hbar\mathbf{p}/m = -i[\mathbf{x}, H]$, therefore we can deduce the interaction term or square of matrix element as

$$|M_{f,i}^{\mathbf{k}}|^2 \propto |\langle \phi_f^{\mathbf{k}} | \boldsymbol{\varepsilon} \cdot \mathbf{r} | \phi_i^{\mathbf{k}} \rangle|^2. \tag{A.9}$$

Appendix B

Raman active phonons in Bi2212

Table B.1: Character table for D_{4h} point group

	E	C_2	$2C_4(z)$	$2C_2'$	$2C_2''$	i	$2S_4$	σ_h	σ_x	σ_d	linear, rotation	quadratic
A_{1g}	1	1	1	1	1	1	1	1	1	1		x^2+y^2, z^2
A_{2g}	1	1	1	-1	-1	1	1	1	-1	-1	R_z	
B_{1g}	1	-1	1	1	-1	1	-1	1	1	-1		x^2-y^2
B_{2g}	1	-1	1	-1	1	1	-1	1	-1	1		xy
E_g	2	0	-2	0	0	2	0	-2	0	0	(R_x, R_y)	(xz, yz)
A_{1u}	1	1	1	1	1	-1	-1	-1	-1	-1		
A_{2u}	1	1	1	-1	-1	-1	-1	-1	1	1	z	
B_{1u}	1	-1	1	1	-1	-1	1	-1	-1	1		
B_{2u}	1	-1	1	-1	1	-1	1	-1	1	-1		
E_u	2	0	-2	0	0	-2	0	2	0	0	(x, y)	

Table B.2: Assignments of observed Raman modes in Bi2212 single crystal [169]

Raman shift (cm^{-1})	Symmetry (D_{2h})†	Assignment
28	A_g **	amplitude mode
47	A_g **	second-order scattering
62	A_g *	Bi a-axis vibration
106	B_{1g} *	Bi b-axis vibration
109	A_g *	Cu a-axis vibration
119	A_g	Bi c-axis vibration
129	A_g	Cu c-axis vibration
180	A_g *	Sr a-axis vibration
180	A_g	Sr c-axis vibration
285	B_{1g}	O_{Cu} c-axis vibration (out of phase)
295	A_g *	O_{Bi} a-axis vibration
355	A_g *	O_{Cu} a-axis vibration
400	A_g *	O_{Sr} a-axis vibration
465	A_g	O_{Sr} c-axis vibration
630	A_g	O_{Bi} a-axis vibration
660	A_g ***	O_{extra} or folded O_{Bi} c-axis vibration

* The Raman modes induced by orthorhombic distortion.
** The Raman modes induced by superstructure modulation.
*** The Raman modes induced by extra oxygen atoms (or folded optical modes).

Appendix C

Additive mode in Raman measurement

Additive mode allows us to measure Raman spectra with high resolution of energy. Here are the configuration and the optical path in this mode.

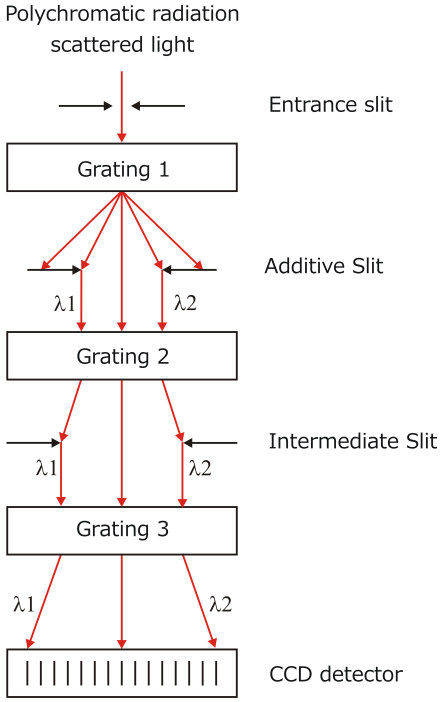

Figure C.1: Optical diagram of the additive mode.

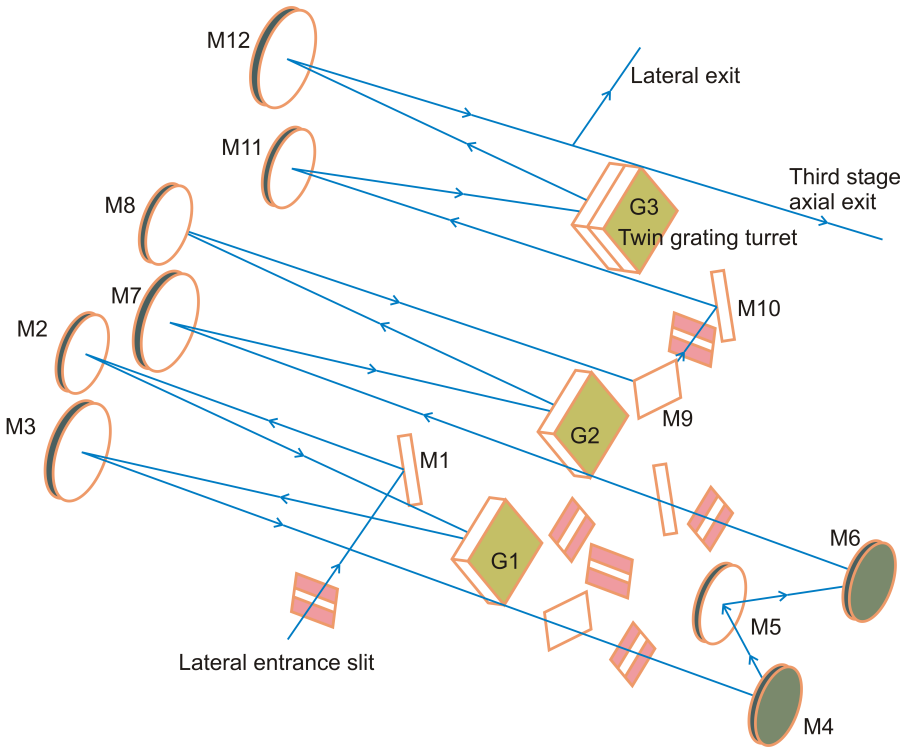

Figure C.2: Optical path in the additive mode. M notation denotes a mirror, G is for grating and S is for slit.